Charge Transport in Printed Silicon Nanoparticle Networks

Batsirai Magunje

Thesis presented for the degree of

DOCTOR OF PHILOSOPHY

In the Department of Physics

Faculty of Science

UNIVERSITY OF CAPE TOWN

May 2013

Abstract

For the first time, the charge transport mechanisms in printed silicon nanoparticle networks have been comprehensively studied using variable temperature *IV* characteristics and Hall effect measurements, supported by microscopy studies. The conductivity can be described as hopping percolation in which activated charge transport is limited by band bending at the interface between particles and electron trapping at surface states.

To probe the charge transport, two types of printed silicon nanoparticle networks based on milled silicon nanoparticles and highly doped *p*-type chemical vapour synthesised nanoparticles, were studied and compared. Four characteristic activation energies for conduction were observed for the milled silicon nanoparticle network irrespective of the resistivity of the silicon used. In contrast, networks formed from highly doped *p*-type chemical vapour synthesised nanoparticles were characterised by only three activation energies. The average activation energies observed in the milled silicon nanoparticle networks were generally higher than those in chemical vapour synthesised nanoparticles, owing to the distinguishing features in the morphology of the particles. The analysis of variable temperature Hall effect data established the presence of four activation energies for electron conduction, in contrast to only three for holes. Hence the fourth and highest activation energy observed in the milled silicon nanoparticle network is due to the activation of electrons from a surface trap state. On the contrary, the conductivity of the chemical vapour synthesised nanoparticles is predominantly *p*-type, hence the electron trap cannot affect the hole transport. Because the charge transport is limited by the mobility of carriers across interfaces, the *IV* characteristics is marked by an unusually high ideality factor arising from the scaling of applied absolute potential over many interfaces along the average conduction path. For the same reasons, the conductivity shows a strong temperature dependence which is characterised by freeze-out of different percolation paths at low temperature.

Acknowledgements

I would like to appreciate my supervisors; Professor David Britton and Professor Margit Härting for their incomparable capabilities and support throughout this project. My heartfelt thanks go to the NanoSciences Innovation Centre group members; past and present, who worked with me tirelessly in the lab against all odds. Many thanks go to Stephen D. Jones, Stanley D. Walton, Serges Zambou, Claire van den Berg and Florence M. Idowu for proof reading this manuscript. I also thank my parents Josiah and Susan Magunje for giving me a good educational foundation upon which this project is based. My appreciation also goes to my beautiful daughters, Tashinga and Tawana; going home to their angelic voices after long days of working made this project worthwhile. To my wife Caroline, I say "Look what the Lord has done". Profound thanksgiving goes to my Lord and Saviour, Jesus Christ for the life, the strength, the protection, the revelations and the provisions.

I owe sincere gratitude to the Deutscher Akademischer Austausch Dienst (DAAD), Germany, the Oppernheimer Memorial Trust and the NanoPower Africa Project funded by United States Agency for International Development (USAID) through the Higher Education for Development (HED) office for covering the financial needs of my thesis. Special mention also goes to sponsors for other various aspects of this work under the UCT NanoSciences Innovation Centre. These were the South African Department of Science and Technology through its business unit, the Innovation Fund, the NanoPower Africa Project funded by United States Agency for International Development (USAID) through the Higher Education for Development (HED) office, the US Airforce Office of Scientific Research, the University of Cape Town Vice Chancellor's Strategic Fund, and the South African National Research Foundation (NRF).

Table of Contents

1 Introduction

Technology based on printed electronics is rapidly advancing and occupies a leading position in the vanguard of the electronics industry. The desirability of printed electronics arises from the possibility of producing components and circuits in a simple and cost effective way compared to conventional electronics [1]. Silicon occupies a central position in semiconductor technology, and printable forms of silicon and other semiconductors will become alternative candidates for the mass production of large area devices and circuitry to conventional thin film technology. Use of printed electronics in the production of devices on low temperature conformable substrates has attracted attention owing to further reduction in cost and a favourable energy budget due to low temperature. The need for affordable, clean and sustainable energy sources has steered innovation in the direction of silicon nanostructured materials for photovoltaic applications [2]. The utility of printed electronics is enhanced if the structural characterisation of the nanoparticles and printed films is complemented by an understanding of the charge transport in the printed nanoparticle networks.

A new class of semiconductor material, based on nanostructured silicon, was introduced in the last decade and the synthesis, microstructure and morphology of the primary nanoparticles, and the structural features of the printed nanomaterial are known and have been reported [2-6]. An example of the electronic application of the printed nanoparticulate silicon has been in the fabrication of fully printed silicon field effect transistors which showed similar behaviour to their thin film counterparts [3]. For the first time, this thesis explores the charge transport in the printed silicon network, both at macro-scale using *IV* measurements, and at micro-scale using variable field Hall effect measurements, over an extended temperature range. Existing models for charge transport were mainly developed for bulk materials, most of which are linked to the non-Arrhenius models developed by Mott, and Efros-Shklovskii, and have mainly been applied to the description of conduction in disordered bulk materials [7-9]. These models usually address the issue of the dimensionality of the transport mechanism as temperature evolves, and the nature of the density of states function in the neighbourhood of the Fermi level in bulk materials [7]. These have been convincing in their description of, for example, charge transport in heavily doped semiconductors and disordered conjugated polymer materials, as well as in explaining conduction in granular metal films [8, 10-13]. However, these models do not perfectly fit to

the behaviour of the printed silicon studied herein, which is characterised by activated hopping transport behaviour of a pure Arrhenius type. The generalised percolation theory has previously been used to describe the charge transport in particle systems that contain at least two dissimilar components [14-16]. The major focus of percolation studies has been the search for the percolation threshold, which is the minimum filler concentration necessary to create a continuous network that covers the entire system [17]. At the percolation threshold, particles in the network will be within a short distance of each other in order to be regarded as touching, and hence permit charge carrier transport between them. In these studies, the emphasis has been on the study of the geometry of the percolation path with not much attention on the activation energies for conduction [15-19]. The conductivity of the silicon nanoparticle network under this study is percolative in nature, but an understanding of activation energies for charge transport is critical in unfolding potential applications for any material system and in electronic circuit design where the detailed knowledge of the behaviour of devices operating over a wide temperature range is required [20]. An important aspect of this thesis is therefore the determination of the activation energies required to establish conduction paths in the printed silicon nanoparticle networks.

A comprehensive study is executed, starting from the determination of the *IV* characteristic of the printed silicon, followed by a detailed analysis that confirms the consistency of the current-voltage behaviour of the material with its given microstructure. Variable temperature variable field Hall effect measurements were also effectively used to investigate the dependency of the statistics of charge carriers on temperature. The correlation between the microstructure of the printed silicon and the electrical behaviour of the material is then successifully constructed to fully explain the charge transport in the printed silicon nanoparticle network. The descriptions given for the charge transport in the printed silicon are expected to be applicable to a broad range of particle networks.

Chapter 2 briefly touches on the structure of silicon and its nanoparticles together with its temperature dependent electrical conductivity. A review of the charge transport mechanisms in disordered systems and percolative networks is outlined in chapter 3. Experimental methods used to investigate the charge transport in silicon nanoparticle networks is presented in chapter 4, followed by the presentation of the research findings in chapter 5. A closer analysis of the research findings is elucidated in chapter 6 and the pertinent conclusions stated in chapter 7.

2 Silicon and silicon nanoparticles

Silicon is the most important material for electronic applications and consequently the basis of the electronics revolution of the 20th century. It constitutes 27.7% of the earth's crust by mass, and is thus the second most abundant element in the earth's crust after oxygen [1]. It occurs mainly as silicon dioxide, commonly known as quartz, and more complex silicate minerals. To obtain silicon, the silicon dioxide is reduced by carbon at high temperature. The reduction produces metallurgical grade silicon [2-3], which is further purified by either the Czochralski technique or the float zone technique [4]. The use of silicon for electronic applications is a result of its unique semiconductor properties [5].

An overview of the structure of silicon and synthesis of nanoparticles is given in this chapter. For crystalline silicon, the dependence of electrical conductivity on band structure, Fermi level and doping is reviewed. The scattering of charge carriers with increasing temperature as well as its influence on the mobility of charge carriers in crystalline materials is discussed with regard to the impact that this may have on charge transport.

2.1 Structure of Silicon

Silicon belongs to group four of the periodic table of elements [6]. Its atomic number is 14, with a shell structure: $1s^2\ 2s^2\ 2p^6\ 3s^2\ 3p^2$. Silicon thus has 4 valence electrons in its outermost shell. According to the atomic orbital model [7-9], the outermost orbitals of a silicon atom form four sp^3 hybrid orbitals which are oriented at 109.5^o, defining the corners of a tetrahedron [4, 10]. Four other atoms can each form a covalent bond with one of the four sp^3 orbitals of the first atom, forming a tetrahedral structure as highlighted in Fig. 2.1. This structure has a face centred cubic lattice [4, 10] with a lattice constant of 5.431 nm [11].

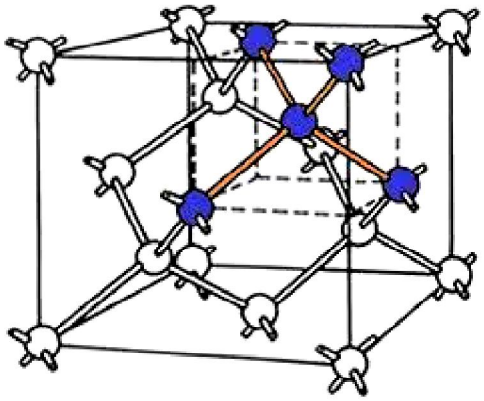

Fig. 2.1: The diamond cubic structure of silicon [4]. The highlighted bonds and atoms represent the tetrahedral structure.

The physical, and in some cases electrical, properties of a material have been shown to be dependent on its microstructure and morphology [12-14]. In broad terms, silicon may have three different microstructures; single crystalline, polycrystalline and amorphous, as shown in Fig. 2.2.

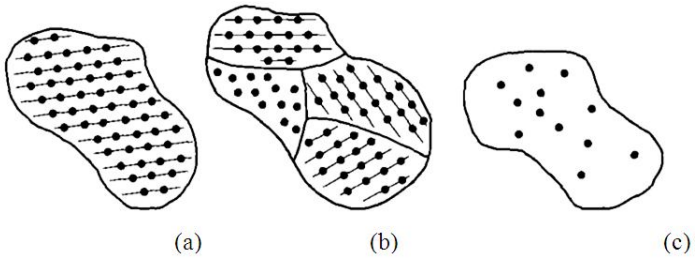

Fig. 2.2: Schematics of three types of silicon: (a) Single crystalline, (b) Polycrystalline and (c) Amorphous [15].

The atoms of crystalline silicon are arranged in a three dimensional periodic manner within the constituent crystals as shown in Fig. 2.2 (a) and (b). Single crystalline silicon is used to produce silicon based microelectronic devices. In polycrystalline form [15], silicon is characterised by many single crystals which are disoriented with respect to each other and meet at grain boundaries [16] as shown in Fig. 2.2 (b). The grain boundaries play an important role in controlling the electrical properties of the polycrystalline silicon [16-17]. This will be discussed in more detail in chapter 3.

2.2 Silicon nanoparticles

Nanoparticles have become favourable candidates for engineering and scientific applications. Silicon nanoparticles have not been spared in this search for novel materials, especially for improved electronic applications [18]. Motivated by the unique properties of materials at nanoscale, one-, two-, and three dimensional nanoparticle arrangements have been synthesised to achieve miniaturisation in electronics [19-20]. Generally, methods of nanoparticle synthesis can be classified into two categories: bottom-up chemical synthesis, and top-down size reduction of bulk material [21-23]. Bottom-up methods are generally regarded as being cleaner, and they involve using isolated and uncontaminated particles [24-26].

Large scale production of silicon nanoparticles has been realised using the top-down synthesis approach which involves the breaking down of bulk material into nano-sized structures or particles [27-31]. It may also involve the vaporisation of a solid followed by condensation of the vapour.

2.2.1 Bottom-up synthesis of silicon nanoparticles

Bottom-up synthesis involves the aggregation of atoms, molecules or relatively small nanoparticles to form a nanostructure. The process can occur through self assembly or positional assembly of nanostructured materials, as well as solid, liquid or gas phase synthesis [23]. Some of the commonly used methods of synthesising nanoparticles using the bottom up approach with respect to silicon are described below.

- **Chemical vapour synthesis (CVS)**: Decomposition of a gaseous precursor can be accomplished using diverse energy sources such as microwave plasma, laser, or a flame. The energy will induce chemical reactions in the gas phase resulting in gas phase nucleation of particles [18, 32-34]. Examples where CVS has been applied include passing silane gas across a hot tungsten filament [18], and thermal pyrolysis of silanes in hot wall reactors [32] to yield large quantities of nanoparticles. Unlike related chemical vapour deposition methods, which result in the deposition of amorphous and crystalline layers [35-37], CVS yields free crystalline nanoparticles which are deposited on reactor walls or surfaces as highly porous films consisting of individual or aggregated nanoparticles. Scriba et al. [18] have used this method to

produce monodisperse single crystalline nanoparticles with sizes of the order of 35nm. The nanoparticles are favourable candidates for printed electronics.

- **Aerosol synthesis**: Aerosol synthesis may be classified into droplet-to-particle and gas-to-particle conversions. In the droplet-to-particle conversion method, droplets of the precursor are suspended in a gas by liquid atomisation and converted to powder by drying or by direct pyrolysis. An example is the pyrolytic decomposition of diluted silane at 950 ^{o}C, resulting in the formation of crystalline, and spherically shaped silicon nanocrystals [35, 38]. Onishuk et al. have used this process to produce silicon nanoparticle aggregates consisting of primary particles of 10 nm size [32]. In the gas-to-particle conversion method, particles form as condensates in a supersaturated vapour of a condensable species in a carrier gas.
- **Liquid phase methods**: These involve either the precipitation of nanoparticles from a solution as a result of a reaction or decomposition from a liquid silane based precursor [39-42]. Passivation of the resulting nanoparticles is necessary to curb recrystallisation and agglomeration, which has been achieved using hydrogen and alkyl groups [43-44]. Liquid phase methods can produce crystalline primary particles with sizes in the order of 10 nm. Common liquid phase methods have little control over the size distribution and surface modification of the nanoparticles. However, Kauzlarich et al. have used a novel approach to produce monodisperse silicon nanocrystals with control over their surface characteristics [45-50]. In another approach, Korgel et al. produced clean, passivated crystalline nanoparticles and nanowires with average diametres of 10 nm and 39.3 nm respectively [49, 51-53].

2.2.2 Top-down processes

These are simple processes, amenable to large scale production, which involve physical and chemical reduction of bulk materials to form nanostructures. Among the top down methods are lithography [54-55] and chemical reduction [56-57]. Some of the notable top-down methods, that yield primary particles, are described below.

- **Milling**: Milling is the most commonly used physical method in the top down production of nanoparticles. During the milling process, the bulk material is crushed to smaller particles due to brittle fracture and plastic deformation. The microstructure, morphology, size distribution, and level of contamination of the resulting nanoparticles are related to

the choice of mill and its process variables. The quality of milled nanoparticles may depend on the density of the milling medium, the milling time, and the milling media to powder ratio [58-61]. Milling usually produces polydisperse nanoparticles which form clusters of varying size. Milled silicon nanoparticles can be used in a wide cross-section of electronic applications [27]. Studies of milled powder, using spectroscopic techniques, have revealed the presence of grain refinement, lattice transformation and amorphorisation [62]. The main concern in the case of silicon nanoparticles intended for electronic applications is the oxidation of the particles. This has been overcome by Härting et al. who have produced silicon nanoparticles which, while not necessarily free of oxygen, contain a disordered monolayer of silicon sub-oxide which permits charge transport [28, 30].

- **Laser ablation**: If laser light is irradiated onto a target at a low fluence, e.g 10mJ/cm^2, with the target immersed in a liquid such as water, hexane, or toluene, the bulk material will evaporate or sublimate into nanoparticles which will then be dispersed in the liquid [63]. Umezu et al. have used pulsed laser ablation on a silicon target, placed in a liquid environment, to yield a colloid of silicon nano-crystallites [63]. The primary particles averaged 3nm, and the aggregate particles had diameters in the order of 10 nm. Makino et al. used a similar approach to prepare crystalline silicon nanoparticles of average size 5nm [64]. In another approach, Semaltianos et al. used femto-second laser ablation in deionised water to produce spherical, partially amorphous, and polydisperse silicon nanoparticles averaging 5 - 200 nm [65].

2.3 Energy band structure of silicon

The band structure is the basis for discussing transport in crystalline semiconductors. The separation in energy between the bonding and anti-bonding orbital states is believed to be the fundamental origin of the energy band gap characteristic of all semiconductors [56, 66-67]. Simplified versions of the band gap model are usually in the form of flat band diagrams showing the conduction band and the valence band energies separated by a gap [68]. Classification of materials according to their conductivities is then related to the magnitude of the energy gap [66, 68]. Silicon's band gap of 1.11eV [68-69] enables it to be used for photoelectronic applications with no need for band engineering.

For three dimensional crystals, electrons moving in different crystallographic directions encounter different potential patterns [4]. In this scenario, energy (E) versus space (k) diagrams are used. The E-k diagrams show the energy bands as a function of crystallographic direction in reciprocal space [8]. The E-k diagram for silicon is shown in Fig. 2.7. The energy band gap, E_g is the difference between the maximum in the valence band energy and minimum in the conduction band energy [8]. From Fig. 2.3, the maximum in the valence band energy occurs at $k = 0$ for both directions considered ([111] and [100]). Silicon is an indirect band gap material. The minimum in the conduction band does not occur at $k = 0$ but occurs along the [100] direction. The band energy gap (E_g) is evaluated as shown in the schematic, and is the difference between the maximum energy in the valence band (E_v) and the minimum energy in the conduction band.

.

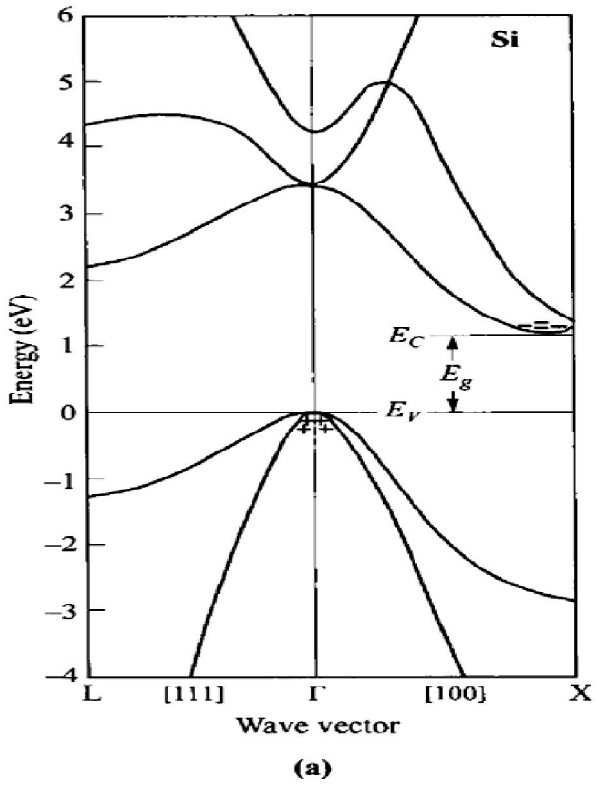

Fig. 2.3: Energy band structure of silicon [8]. $E_g = E_c$-E_v.

Transitions in an indirect band gap material must include an interaction with the crystal so that crystal momentum is conserved [4, 8].

2.3.1 Thermal excitation of carriers

When sufficient thermal energy is supplied to electrons in a silicon crystal such that thermal energy is greater than the band gap energy, covalent bonds in the valence band can be broken and electrons will be promoted into the conduction band, leaving behind half filled molecular orbitals in the valence band. If a potential difference is then applied across the crystal, electrical conduction results. Promotion of one electron into the conduction band results in the generation of a hole in the valence band [4, 6]. The number of electrons generated per unit volume, *n* equals the number of holes, *p* as

$$n = p\,. \tag{2.1}$$

For a system of more than one type of charge carrier, the overall conductivity is the sum of contributions from all carriers involved. Therefore the electrical conductivity, σ is given by

$$\sigma = \sum_i n_i |q_i| \mu_i\,, \tag{2.2}$$

where μ_i is the mobility and q_i the charge on the carrier of type i. Subject to the applied electric field, E the drift velocity, v, for a carrier of type i is given by $v_i = \mu_i E$.

For a system of holes and electrons

$$\sigma = ne\mu_e + pe\mu_p\,. \tag{2.3}$$

From equation (2.1) we have,

$$\sigma = ne\left(\mu_e + \mu_p\right)\,. \tag{2.4}$$

The number of electrons which have been excited may be approximated by [8]

$$n = AT^{\frac{3}{2}} \exp\left(\frac{-E_g}{2k_B T}\right)\,, \tag{2.5}$$

where E_g is the band gap, $k_B T$ is a measure of the thermal energy and k_B is the Boltzmann's constant.

2.4 Statistics of charge carriers

The study of the statistics of charge carriers in semiconductors, particularly their distribution in energy bands, as well an understanding of the free carrier concentration to the Fermi level [70] are of importance when charge transport patterns are discussed. The density of states (DOS), $g(\varepsilon)$ is defined as the number of electronic states with energy between ε and $\varepsilon + d\varepsilon$ per unit volume of the crystal [3]. The DOS is a function of the effective mass of the charge carrier and the energy band in which the states are considered. The DOS functions for the conduction and valence bands are given respectively by [70]

$$g_c(\varepsilon) = \frac{m_n^* \sqrt{2m_n^*(\varepsilon - \varepsilon_c)}}{\pi^2 h^3} \text{ for } \varepsilon > \varepsilon_c,$$

and $$g_v(\varepsilon) = \frac{m_p^* \sqrt{2m_p^*(\varepsilon - \varepsilon_c)}}{\pi^2 h^3} \text{ for } \varepsilon < \varepsilon_c, \quad (2.6)$$

where m_n^* and m_p^* are the effective masses of electrons and holes respectively.

Applying Fermi-Dirac statistics yields information about the proportion of filled states with respect to the number of the allowed states [8]. The probability, $f(\varepsilon)$ of occupation for an allowed state of energy ε is given by [70]

$$f(\varepsilon) = \frac{1}{1 + \exp\left(\frac{\varepsilon - \varepsilon_F}{k_B T}\right)}, \quad (2.7)$$

where ε_F is the Fermi energy, defined as the maximum energy of a state that can be occupied by an electron at absolute zero temperature.

Similarly, the probability of a hole occupying a state of energy ε in the valence band is given by

$$f(\varepsilon) = 1 - \frac{1}{1 + \exp\left(\frac{\varepsilon - \varepsilon_F}{k_B T}\right)}. \quad (2.8)$$

For non degenerate semiconductors where the Fermi level is at least 0.1eV above the valence band and below the conduction band, [8], Maxwell-Boltzmann statistics give the following: for electrons

$$f(\varepsilon) = \exp\left(-\frac{\varepsilon - \varepsilon_F}{k_B T}\right) \text{ for } \varepsilon > \varepsilon_c, \tag{2.9}$$

and for holes $$f(\varepsilon) = 1 - \exp\left(-\frac{\varepsilon_F - \varepsilon}{k_B T}\right) \text{ for } \varepsilon < \varepsilon_c. \tag{2.10}$$

From equations (2.9) and (2.10) we derive the concentration of electrons in the conduction band and holes in the valence band as follows

$$n = \int g_c(\varepsilon) f(\varepsilon) d\varepsilon \ , \tag{2.11}$$

giving,

$$n = N_c \exp\left(-\frac{\varepsilon_c - \varepsilon_F}{k_B T}\right) \tag{2.12}$$

for electrons, and $$p = \int g_v(\varepsilon)(1 - f(\varepsilon)) d\varepsilon \,. \tag{2.13}$$

giving

$$p = N_v \exp\left(-\frac{\varepsilon_F - \varepsilon_v}{k_B T}\right), \tag{2.14}$$

for holes.

In equations (2.12) and (2.14), N_c and N_v are the effective densities of states in the conduction and valence bands respectively [71-72]. For an intrinsic semiconductor material, the electron density excited to the conduction band creates an equal density of holes in the valence band [73] such that

$$n = p = n_i, \tag{2.15}$$

where n_i is the intrinsic carrier concentration. Invoking the law of mass action, we get

$$np = n_i^2 = N_v N_c \exp\left(\frac{\varepsilon_v - \varepsilon_c}{k_B T}\right), \tag{2.16}$$

but $\varepsilon_v - \varepsilon_c = E_g$ as discussed in section 2.3, which results in

$$n_i = \sqrt{N_v N_c \exp\left(-\frac{\varepsilon_g}{k_B T}\right)} \ . \tag{2.17}$$

This implies that materials with low band gap energy have a higher intrinsic carrier density. The condition, $n = p$ may be used to predict the position of the Fermi level as

$$N_c \exp\left(\frac{-(\varepsilon_c - \varepsilon_F)}{k_B T}\right) = N_v \exp\left(\frac{-(\varepsilon_c - \varepsilon_F)}{k_B T}\right), \tag{2.18}$$

giving,

$$\varepsilon_F = \frac{\varepsilon_c + \varepsilon_v}{2} + \frac{k_B T}{2} \ln\left[\frac{N_v}{N_c}\right] . \tag{2.19}$$

For parabolic bands, the effective densities of states are given by

$$N_c = 2\left(\frac{2\pi m_n^*}{h^2}\right)^{\frac{3}{2}} \text{ and } N_v = 2\left(\frac{2\pi m_p^*}{h^2}\right)^{\frac{3}{2}} . \tag{2.20}$$

Substituting these into equation (2.19) yields

$$\varepsilon_F = \frac{\varepsilon_c + \varepsilon_v}{2} + \frac{k_B T}{4} \ln\left[\frac{m_p^*}{m_n^*}\right] . \tag{2.21}$$

Equation (2.21) shows that the Fermi energy depends on the temperature and effective masses of the charge carriers. At $T = 0$, the Fermi level is midway in the band gap. At high temperature, as the second term does not change appreciably, the Fermi level for an intrinsic material is considered to be near the midpoint of the band gap.

2.4.1 Doping of semiconductors

The significance of semiconductors for electronic device fabrication is based on the fact that their conductivity can be tuned by the incorporation of appropriate dopant elements. Doping can be described as the introduction of shallow level defects into the band gap of a semiconductor with the intention of increasing its conductivity [74-75]. When impurities are added to a semiconductor material such as silicon, they enter the lattice substitutionally and can give up an electron to the conduction band [3, 76], as with the case of a group five dopant, or can donate a hole to the valence band, as with the case with group three dopants [3, 76].

The amount of energy necessary to free an electron from the donor atom and liberate it into the conduction band is called the donor ionisation energy [76]. Donor ionisation energies are about 0.01 eV and 0.05 eV for various group five impurities in germanium and silicon respectively [3, 76]. The energies involved in ionisation of impurity levels are shown in Fig. 2.4.

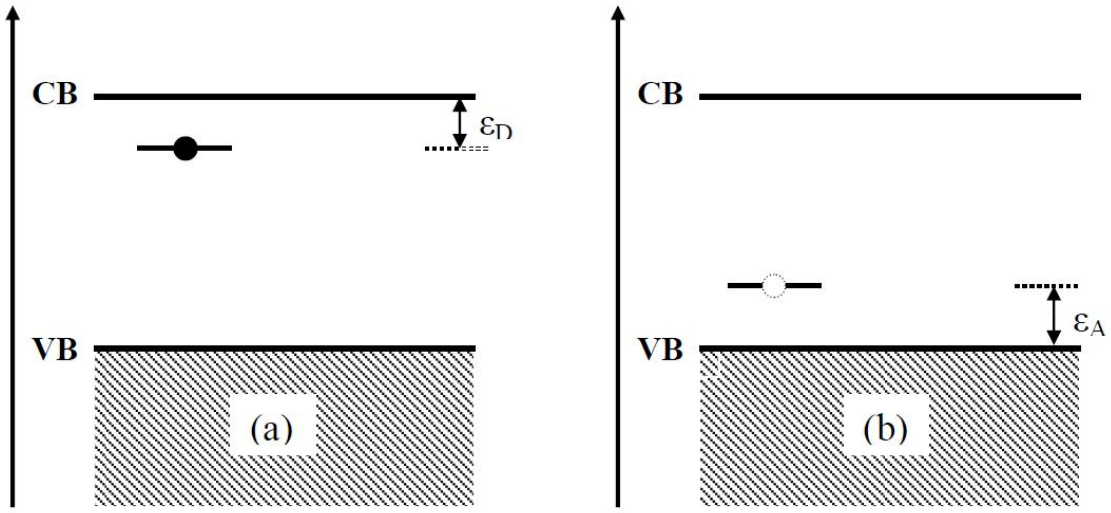

Fig. 2.4: Ionisation of impurity levels in a (a) donor atom and (b) acceptor atom [72].

In Fig. 2.4 (a), the electron is in a bound state at energy ε_D below the conduction band (CB) minimum. On acquiring energy of at least equal to ε_D, the electron will be excited into the conduction band. The ionisation of a hole bound to an acceptor atom is shown in Fig. 2.4 (b). The hole is bound at an energy ε_A above the valence band (VB) energy. On supplying energy which is at least equal to the required ionization energy, $\varepsilon_{A,}$ the hole will be moved to a valence band state leaving behind an empty acceptor state. The

acceptor ionisation energies range from 0.016 eV to 0.065 eV in silicon and about 0.01 eV in germanium. The net charge after doping remains neutral. A comparison of density of states, probability distribution and carrier concentration for intrinsic and doped semiconductors is schematically displayed in Fig. 2.5.

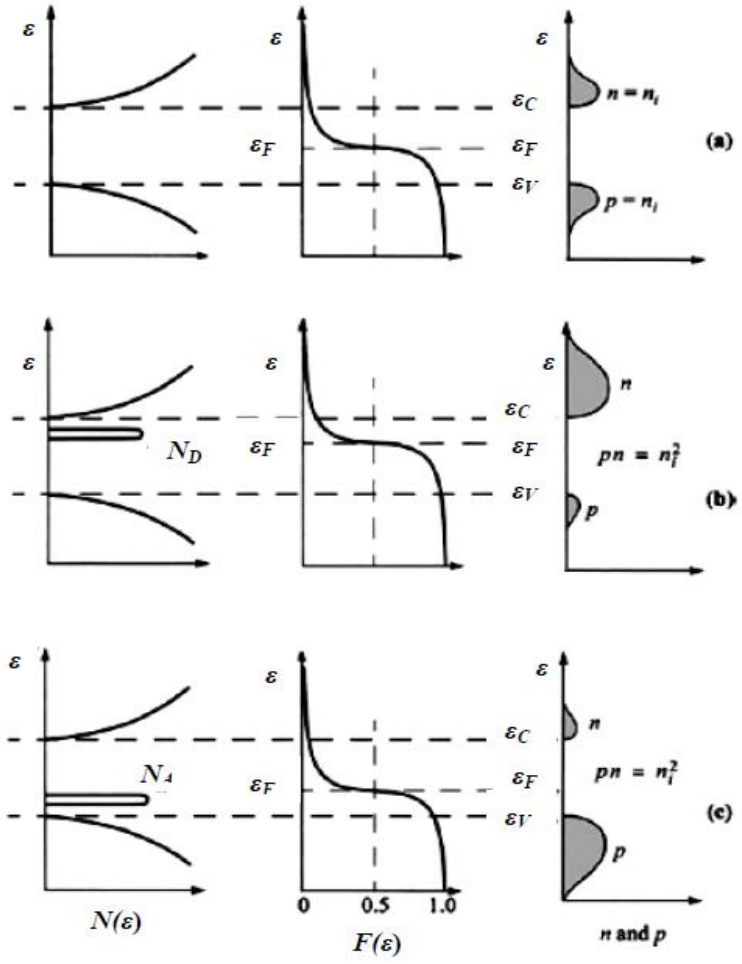

Fig. 2.5: Density of states, probability distribution and carrier concentration for (a) intrinsic, (b), *n*-type, and (c) *p*-type semiconductors at thermal equilibrium [8].

The diagrams show the presence of donor and acceptor levels in the energy band gap for *n*- and *p*-type semiconductors. The Fermi level shifts upwards towards the CB in *n*-type semiconductors and downwards towards the valence band in *p*-type materials. Predominant charge carriers are electrons for *n*-type and holes for *p*-type semiconductors. A quantitative argument can be used to justify these qualitative statements. Since the net charge remains neutral after doping, then for an *n*-doped semiconductor

$$0 = (-qn) + (qp) + (qN_D), \tag{2.22}$$

where N_D is the donor concentration per unit volume and $np = n_i^2$, giving $p = \frac{n_i^2}{n}$. Substituting into (2.22) yields

$$0 = (-qn) + (qn_i^2) + (qN_D)\,. \tag{2.23}$$

Solving (2.23) for n gives

$$n = \frac{N_D}{2} + \frac{N_D}{2}\sqrt{1 + \frac{4n_i^2}{N_D^2}}\,, \tag{2.24}$$

for $N_D >> n_i, \quad n = N_D$. (2.25)

The implication of this for heavily *n*-doped semiconductors is that, the predominant charge carriers will be electrons. For the position of the Fermi level, substituting (2.25) into (2.18) gives

$$n = N_c \exp\left(\frac{-(\varepsilon_c - \varepsilon_F}{k_B T}\right).$$

Hence,

$$N_D = N_c \exp\left(\frac{-(\varepsilon_c - \varepsilon_F}{k_B T}\right),$$

and thus

$$\varepsilon_c - \varepsilon_F = k_B T \ln\left[\frac{N_c}{N_D}\right]\,. \tag{2.26}$$

As the donor density increases, the energy difference, $\varepsilon_c - \varepsilon_F$, decreases implying that the Fermi level shifts towards the conduction band [8]. For a *p*-type semiconductor, $N_A >> n_i$ and $p = N_A$, giving $n = \frac{n_i^2}{n_A}$, and

$$N_A = N_v \exp\left(\frac{-(\varepsilon_F - \varepsilon_v}{k_B T}\right). \tag{2.27}$$

The position of the Fermi level is then given by

$$\varepsilon_F - \varepsilon_v = k_B T \ln\left[\frac{N_v}{N_A}\right], \tag{2.28}$$

The Fermi level is shifted downward towards the valence band.

It is possible to have both types of dopants present at the same time. The electrical conductivity is then dictated by the impurity with the higher density [8]. Such a type of semiconductor is known as a compensated semiconductor.

2.5 Temperature Dependence of Semiconductor Conductivity

The conductivity, σ, of a semiconductor depends on the concentration of free carriers and their mobility as given by equation (2.3). The mobility and carrier concentration are in turn functions of temperature as shown in Fig. 2.5. Recasting equation (2.3) to emphasise the temperature dependence gives

$$\sigma = e\left(n(T)\mu_e(T) + p(T)\mu_p(T)\right) \tag{2.29}$$

The mobility of electrons is mainly influenced by two scattering mechanisms. These are: lattice scattering and scattering by impurity or defect centres. Defects include vacancies, interstitials, dangling bonds, and grain boundaries. In the case of particulate composites, scattering may occur at particle interfaces and surfaces resulting in low mobility. Moreover, lattice vibrations result in the transfer of crystal momentum to the electrons causing a decrease in mobility with increasing temperature [77-78]. The presence of charged impurities also affects the mobility of electrons. Scattering of electrons by ionised impurities occurs at low temperature since carriers will be moving more slowly and have sufficient time to interact with the charged centers. The temperature dependence of mobility due to phonon scattering follows a $t^{\frac{3}{2}}$ law, while the mobility due to impurity scattering varies as $t^{\frac{-3}{2}}$ as shown in Fig. 2.5 (a). The temperature dependence of electron concentration for a doped semiconductor can be seen in Fig. 2.5 (b). At very low temperature, only a few electron-hole pairs exist and the donor electrons are bound to the donor atoms [79]. This is known as the freeze out (or ionisation region). As temperature increases, ionization increases and at about 100K [32] all of the donor atoms are ionised. The region where all dopants have been ionized is called the extrinsic

(saturation) region. In this region, an increase in temperature does not result in an increase in carrier concentration.

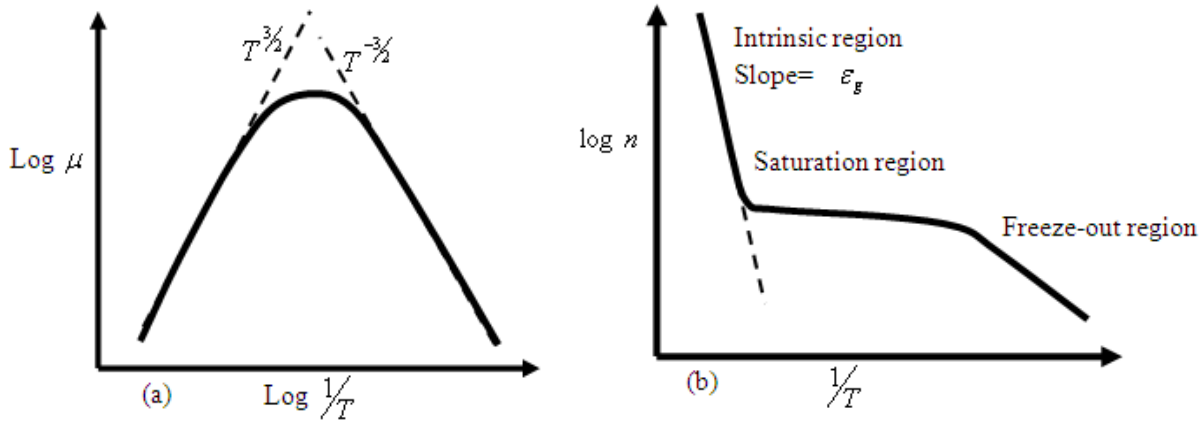

Fig. 2.5: Dependence on temperature, T of mobility, μ (a) and (b) Carrier concentration, n for a doped semiconductor [8, 22].

At high temperatures, the thermally generated intrinsic carriers outnumber the dopants, and as a result carrier concentration increases as temperature increases as shown in Fig. 2.5 (b).

Equation (2.9) shows that conductivity depends on carrier mobility and concentration. As a result there are a variety of temperature dependencies for conductivity. Impurity scattering might be dominant at low temperature while the carrier concentration is determined by extrinsic doping with the result that conductivity increases with temperature. Other possibilities could be expected, depending on the doping level and temperature, with different temperature dependence of conductivity [30-33]. However at high temperatures (> 400 K), when carrier concentration is intrinsic and mobility is dominated by lattice scattering, the conductivity depends only on the band gap, ε_g, and the temperature as according to

$$\sigma \propto \exp\left(\frac{-\varepsilon_g}{k_B T}\right). \qquad (2.30)$$

In this high temperature range, measured conductivity data can be used to determine the semiconductor band gap [23].

3 Charge transport in disordered systems and percolative networks.

This section reviews charge transport processes in inhomogeneous systems, including nanocomposites, grain boundary interfaces, percolative systems and disordered materials in general. A discussion on the Hall effect in inhomogeneous materials is also given, highlighting the fundamental origin of the anomalous Hall effect in particular.

It has been established that electron transport in disordered materials is influenced by the dominance of charge localisation induced by the presence of disorder [1-4]. Though remarkable efforts have been invested in studying charge transport in disordered solids, questions pertaining to the spatial arrangement of electronic states have not yet been fully answered [2]. This challenge has crept into similar research efforts to understand the charge transport mechanisms in nanoparticle and molecular networks. As such, models of charge transport in disordered systems are mainly still phenomenological [2-4]. In spite of this, nanostructured materials have become the testing ground for the study of electron transport. Examples of such novel model systems include "artificial solids" [5] formed by mono-disperse metallic nanostructures [6-8], close packed assemblies of nanoparticles [9], and carbon black-polymer composites [10-11]. So far, hopping and percolation have been unambiguously identified as strong candidates for the description of charge migration in these emerging materials.

To understand the charge transport in a nanoparticle system, it is important to master three key aspects of the system: nanoparticle characteristics such as size, morphology and chemical nature; particle-particle interface properties; and the arrangement of the particles in the system which is dependent on nanoparticle size distribution [7-8]. The arrangement of the particles in the system defines its electronic properties, especially the conductivity as predicted by the percolation theory [12-14].

3.1 Charge Transport in Nanoparticle systems

As highlighted earlier, the charge transport in nanoparticle systems relies on the fundamental understanding of the transport within the individual particles, inter-particle couplings, and the spatial distribution of the particles. The spatial distribution encompasses how the particles are assembled or arranged in the film or nanostructure [7]. The arrangement of the nanoparticles can be in the form of clustering of particles [12], formation of crystalline nanostructured films [15], or massive nanocomposites composed of poly-disperse nanoparticles [16]. Typically, nanoparticle systems are characterised by a web of interfaces which present a broad distribution of barriers. Examples of such systems include nanocomposites and powder networks [17-20]. If an individual nanoparticle is regarded as a site of the nanoparticle network, then it is important to understand the movement of charge carriers through it to complement the observed macro-scale transport. The internal structure of nanoparticles can be crystalline or amorphous. For single crystalline particles, it is plausible to perceive intra-particle transport of charge by drift and ballistic transport. In the case of polycrystalline particles, intra-particle charge transport may be modulated by grain boundaries as shall be discussed in section 3.2. Other considerations such as the energy levels of individual nanoparticles are important, for example in understanding elastic and inelastic cotunneling in metal quantum dots [7]. Sometimes the relative energy levels and their occupancy can affect the transport mode of electrons between particles [21]. The doping levels of nanoparticles can influence the preferred charge transport mode in much the same way as tunneling or field emission is the preferred transport for a metal contact to a highly doped semiconductor [22]. The morphology of the nanoparticles can also influence how the particles cluster in the nanostructure, possibly resulting in a broad spectrum of charge transport barriers. Charge carriers can move between clusters whose coupling may be energetically favourable in the same manner as the particle-particle scenario.

Depending on the inter-particle coupling, conventional current transport processes can be used to describe particle-particle charge migration. The basic electron transport processes across an interface include thermionic emission (TE), tunnelling (sometimes called field emission (FE)), and thermionic field emission (TFE) [15]. Fig. 3.2 shows an energy diagram representing the interface between two identical

nanoparticles (1 and 2) presenting a barrier, Φ, to charge transport and the underlying charge transport processes.

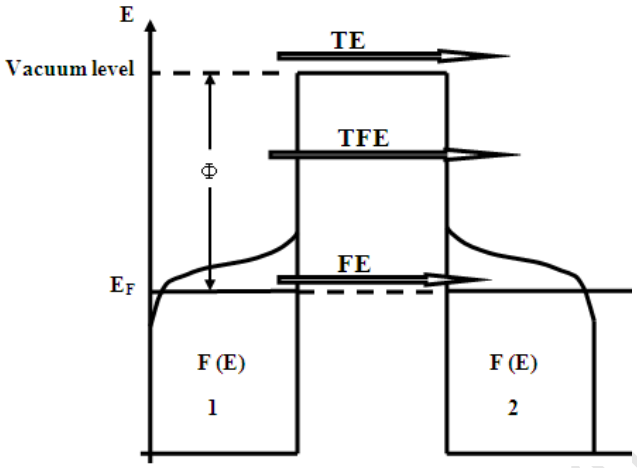

Fig. 3.2: Basic charge transport processes (TE, TFE, and FE). F(E) 1 and F(E) 2 are the density of state functions of particle 1 and particle 2 respectively. Φ is the barrier height at the interface between the two particles.

3.1.1 Thermionic emission (TE)

In the broadest sense, thermionic emission (TE) may involve the transmission of charge carriers across an interface between a heated surface and an insulating space [23-24]. Charge transport by TE involves the thermal excitation of charge carriers from nanoparticle 1 (Fig. 3.2) to energies greater than the barrier height resulting in the carriers passing over the barrier to occupy a state in particle 2. For an applied voltage, V, the current density across the interface will be given by [22, 25-26]

$$J = A^{*}T^{2}\exp\left(\frac{-q\Phi}{k_{B}T}\right)\exp\left(\frac{qV}{k_{B}T}\right), \tag{3.1}$$

where $A^{*} = \frac{4\pi q m^{*} k_{B}}{h^{2}}$, is the effective Richardson constant for thermionic emission and q, m^{*}, k_{B}, and h preserve the same meanings as in chapter 2. The TE current, J_{TE} is then given by

$$J_{TE} = A^{*}T^{2}\exp\left(\frac{-q\Phi}{k_{B}T}\right). \tag{3.2}$$

3.1.2 Tunnelling

Tunnelling is sometimes called field emission (FE) [26] and is represented by the arrow for electrons crossing the barrier near the Fermi level in Fig. 3.2. It is the means through which charge is able to flow between weakly coupled sites, that is, a situation where wave functions are mainly localized on each site. In nanocomposites, the particles may be separated by an insulator or the barrier may represent a surface or interface state. At room temperature, thermal fluctuations are of the order of $k_B T \approx 25\,\text{meV}$, which is much smaller than typical barrier heights [27-28]. Hence, from a classical picture, charge transport is not possible except at high temperature. However charge can move from particle to particle via tunnelling. The tunnelling transmission probability decays with barrier width and barrier height [7]. For heavily doped particles and for charge transport at low temperature, tunnelling is more pronounced [22, 26, 29]. For typical current-voltage characteristics in which thermionic emission is dominant, the total current density, which consists of both thermionic emission and tunnelling, can be expressed as [30]

$$J = J_0\left[\exp\left(\frac{qV}{\eta k_B T}\right) - 1\right], \tag{3.3}$$

where J_0 is the saturation current density and η is the diode ideality factor [26].

3.1.3 Thermionic field emission (TFE)

Thermionic field emission is the tunnelling of thermally excited carriers at energies between those of TE and FE. The excited carriers will generally experience a thinner barrier than those transferred by field emission. The relative contribution of these components depends on temperature and doping level of the particles involved.

Sheng et al. [31] described a mechanism for tunnelling of electrons through a barrier whose height varies due to local temperature fluctuations. Transport in many composite systems follows the Sheng model, especially if the conducting particle size is of micrometre order [31-32]. Sheng et al. argue that for a variety of disordered materials in which most of the conducting electrons are delocalised and free to move over very large distances as compared to atomic dimensions, the electrical conduction

is dominated by electron transfer between large conducting segments rather than by hopping between localised sites within the conducting segments [33-34]. Examples of such materials are some conductor-insulator composites, disordered semiconductors and doped organic semiconductors. In this model [35], it is assumed that the two conducting islands separated by an insulating layer form a junction and charge carriers tunnel through the junction [21, 32]. Due to random thermal motion of electrons at the conducting surface, there can be transient deficit or excess of charge at the tunnel junction surfaces, resulting in fluctuation of voltage at the junction known as thermal fluctuation of voltage [31, 34], giving rise to fluctuation induced tunnelling.

3.1.4 Fluctuation induced tunnelling

Fluctuation induced tunnelling is a tunnelling conduction mechanism for disordered materials proposed by Sheng et al. [32, 36-38], in which the modulation of the tunnelling barriers by thermal fluctuations plays an important role in determining the dependence of the conductivity on temperature and electric field. Charge transport between large conducting segments in a disordered system is characterised by tunnelling between areas shown schematically by heavy lines in Fig. 3.3 (a).

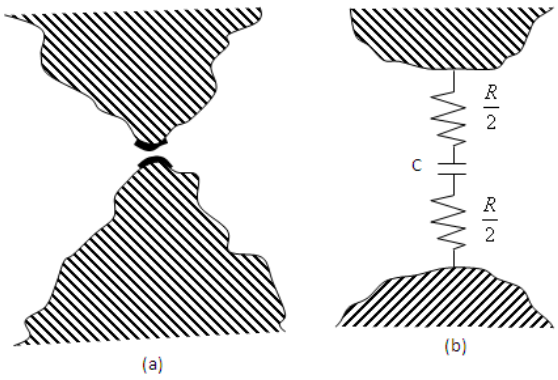

Fig. 3.3: A region of close approach between two conducting segments represented by shaded regions. (a) A region where most tunnelling occurs. (b) Equivalent circuit model for the junction [31]. C and $R/2$ are as described in the text.

According to the description given by Sheng et al., the junction between the two segments presents a capacitance, C, and effective contact resistances $R/2$ connecting the junction capacitor to the conducting segments [31] as shown in Fig. 3.3 (b).

Due to thermal motion of electrons in the conducting junction, there will be voltage fluctuations across the junction. The random variation of voltage across the junction is often referred to as Johnson noise [34], V_T. If the system is considered to have one degree of freedom, then applying the equipartition theorem gives [31]

$$\frac{1}{2}\left\langle CV_T^2 \right\rangle = \frac{1}{2}k_B T \ , \tag{3.4}$$

giving

$$\left\langle V_T^2 \right\rangle = \frac{k_B T}{C} . \tag{3.5}$$

Since the tunnel junctions in disordered materials are usually small in area, the resulting temperature induced voltage fluctuations across the junctions are expected to play an important role in modifying the electron tunneling probability.

In the fluctuation induced tunneling model, the temperature dependence of the composite conductivity is governed by [31]

$$\sigma = \sigma_0 \exp\left(\frac{-T_1}{(T + T_0)}\right). \tag{3.6}$$

Physically, T_1 is the energy required for an electron to cross the insulating barrier between conducting segments, and T_0 can be viewed as the temperature above which the fluctuation effects become significant. At $T << T_0$, it can be said that simple elastic tunneling takes place and is just a special case of fluctuation induced tunneling which occurs at low temperature. When temperature is increased from $T << T_0$ to $T \approx T_0$, the tunnelling barrier as seen by the electrons is effectively reduced in height by the fluctuation voltages. Furthermore, the most rapid change in the effective barrier height occurs when T is in the same order as T_0. For $T > T_0$, thermally activated fluctuation induced tunnelling is more pronounced. Between the two limiting behaviours namely thermally activated fluctuation induced tunneling at high temperatures and simple elastic tunnelling at low temperatures, dependence of the conductivity is controlled by the shape of the tunnelling barrier [31, 39-40].

A disordered composite material contains a proliferation of tunnel junctions with diverse junction parameter values. Consequently the effects of voltage fluctuations are

expected to vary from one junction to another. The equations above were derived through the application of the effective medium theory [25, 38], hence no matter what the values of the junction parameters might be, the behaviour of each junction is expressible in terms of a single junction characteristics with appropriate values of T_0 and T_1 [31-32, 34, 40]. Effectively, the composite material can be regarded as a random resistor network in which the resistors represent tunnel junctions with distributions in values of T_0 and T_1.

The fluctuation induced tunnelling model is applied to disordered systems where the conductivity is believed to be dominated by electron tunnelling across small gaps separating large (or long) conducting regions (or pathways). Fluctuation induced tunnelling has been shown to agree excellently with experimental results [32, 35, 39-40].

3.2 Grain boundaries in semiconductors

A grain boundary is an interface between two crystallites of different orientation [41]. The mismatch in bonding between the two crystallites results in bond defects at the grain boundary. A polycrystalline material is an aggregate of relatively small crystallites separated by grain boundaries [42-43]. Within any particular crystallite, atoms are arranged in a strictly periodic way. The boundary defects at the grain boundary translate into localised electronic states or interface states [44]. The energy distribution of these states is important in the determination of carrier transport processes. The main interest in grain boundaries has been based on the need to understand the extent to which parameters such as the resistivity, recombination efficiency, and *IV* characteristics are modified by the presence of these defects [45-47]. In the simplest approximation, charge transport across a grain boundary interface is analogous to that across inter-particle and inter-cluster interfaces. For a system of polycrystalline nanoparticles, the grain boundary interfaces in the individual nanoparticles are perceived to present barriers similar to those present in the inter-particle network.

3.2. Charge transport across the grain boundary interface

Charge transport between crystallites depends on the extension of the depletion layers, wholly or partially through the grains [43]; the relative size of the Debye length and average grain size; and whether the mean free path is greater or less than the grain size [43, 46]. For partially depleted crystallites, the mobility of charge carriers will be temperature activated and correlates with the grain diameter [46, 47]. In such a situation, the Hall effect measures the carrier concentration in the bulk of the grain. If the depletion layers extend completely through the grains, the measured carrier concentration will be much lower than the doping level. For mean free paths which are greater than the grain size, the Hall effect would measure the number of carriers moving between grains and not the number of carriers in the bulk of the grains. Acceleration of carriers across the grain boundaries is modulated by band bending [48-49]. Band bending reaches a maximum when the grains are fully depleted and the mobility of carriers will be a minimum [46-50]. Charge transport across the grain boundary interface has been attributed to thermionic emission [46-47]. A combination of thermionic emission and drift diffusion has successfully accounted for charge transport across the space charge region of the grain boundary interface in the presence of an electric field [51-57]. Consequently, the current-voltage characteristic of a polycrystalline resistor is generally described by [43, 45-46]

$$I = I_0 \sinh\left[\frac{qV}{2k_B T}\right], \tag{3.7}$$

where I is the current, V is the voltage and I_0 is the saturation current. I_0 is related to band bending and grain size [46].

3.3 Mechanism of charge transport in disordered materials

As pointed out in earlier, charge transport in disordered materials is determined by the presence of localised electronic states [58]. Localised states can either act as traps that terminate charge transport via extended states or they can participate in charge transport in a hopping mode. In hopping transport, charge carriers move by tunnelling or thermal activation between localised states [59]. The temperature dependence of the electrical resistivity of disordered materials can reveal information about the charge transport mechanism inherent in the material [4, 60]. In general, for an

extended temperature range, the DC conductivity in disordered materials has the form [61]

$$\sigma = \sigma_0 \exp\left[-\left(\frac{\Delta\varepsilon}{k_B T}\right)^f\right], \tag{3.8}$$

where σ_0 depends on the underlying material system [3] and f depends on the material, and also sometimes on the temperature range in which the conductivity is studied [58, 62]. In many inorganic materials, f is close to unity at temperatures close to and higher than room temperature, while at lower temperatures, f can essentially be smaller than unity, whereas $f \approx 2$ in organic disordered materials [3, 62]. The DC conductivity can generally be represented in the form [4]

$$\sigma = e\int d\varepsilon \mu(\varepsilon) n(\varepsilon), \tag{3.9}$$

where e is the elementary charge, $n(\varepsilon)d\varepsilon$ is the concentration of electrons in the states with energies between ε and $\varepsilon + d\varepsilon$ and $\mu(\varepsilon)$ is the mobility of these electrons. Under equilibrium conditions, the concentration of electrons $n(\varepsilon)d\varepsilon$ is determined by the density of states $g(\varepsilon)$ and the Fermi function $f(\varepsilon)$, which is dependent on the Fermi energy ε_F, that is

$$n(\varepsilon) = g(\varepsilon) f(\varepsilon), \tag{3.10}$$

and

$$f(\varepsilon) = \frac{1}{1 + \exp\left(\frac{\varepsilon - \varepsilon_F}{k_B T}\right)}. \tag{3.11}$$

The Fermi level in almost all known real inorganic disordered semiconductors is situated in the mobility gap [1-2]. The charge carrier mobility, $\mu(\varepsilon)$ in localised states is much smaller than that in the extended states above the mobility edge. Charge carriers possessing energy within $k_B T$ of the mobility edge dominate the conductivity [62]. Within this energy band, conductivity is

$$\sigma = e\mu_c n(\varepsilon_c) k_B T, \tag{3.12}$$

where μ_c is the mobility of electrons greater than ε_c, and $n(\varepsilon_c)k_BT$ is their approximate concentration ,where

$$n(\varepsilon_c) = f(\varepsilon_c)g(\varepsilon_c) = \frac{g(\varepsilon_c)}{1+\exp\left(\frac{\varepsilon_c - \varepsilon_F}{k_BT}\right)} \ . \qquad (3.13)$$

At low temperatures more electrons occupy localised states than extended states. Hopping of electrons between localised states then dominates the charge transport [62].

3.3.1 Hopping transport via localized states

At high enough temperature electrical conductivity in disordered materials is dominated by electron transport through localized states above the mobility edge [3, 56, 63]. As temperature decreases, the concentration of free electrons decreases, resulting in electrical conductivity diminishing. Under such low temperatures, charge transport is mainly due to tunnelling of electrons between localised states in the band tails. The tunnelling by charge carriers resembles a series of their hops between randomly distributed sites [62]. Each of the sites presents a localised electronic state with energy ε [59]. If the concentration of electrons for the localised states is assumed to be N_0, their distribution is described by the density of state (DOS) function $g(\varepsilon)$ [59, 62]

$$g(\varepsilon) = \frac{N_0}{\varepsilon_0} G\left(\frac{\varepsilon}{\varepsilon_0}\right), \qquad (3.14)$$

where ε_0 is the energy scale of the DOS distribution and $G(\varepsilon/\varepsilon_0)$ is a function governing the energy dependence of the DOS function.

The probability, γ_{ij} of an electron tunnelling from a localised state i to a lower in energy localized site j depends on the spatial separation r_{ij} between sites i and j as [62]

$$\gamma_{ij} = \nu_0 \exp\left(\frac{-2r_{ij}}{\alpha}\right), \tag{3.15}$$

where α is the localisation length (Fig. 3.5) which is assumed to be identical for sites i and j. The quantity ν_0 depends on the electron interaction mechanism that causes the transition, for instance, interaction of electrons with phonons.

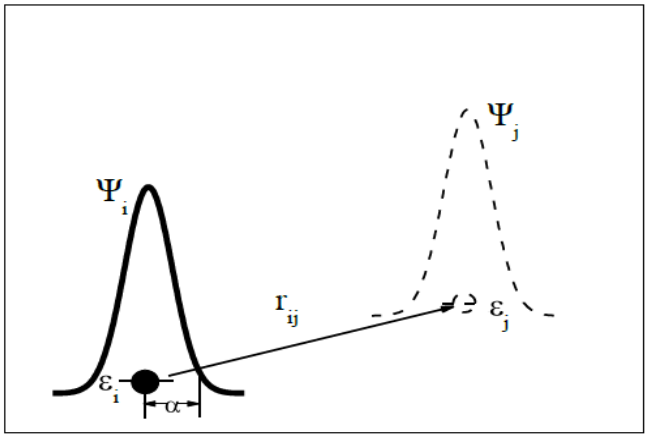

Fig. 3.5: Hopping transition between two localised states i and j with energies ε_i and ε_j, respectively. The solid and dashed lines depict the carrier wave functions on sites i and j respectively [62].

The energy to support the transition may come from the absorption of corresponding thermal energy [60]. When an electron undergoes a transition from a low energy localised site i to a higher energy localised site j, the rate of transition depends on the energy difference between the states. It can be explicitly stated that depending on temperature, the relationship between energy-dependent and distance dependent considerations has an impact on the type of hopping mechanism [62]. Two regimes of hopping transport have been established. These are the nearest neighbour hopping and variable range hopping mechanisms [2, 58], and are explained further in the following sections.

3.3.2 Nearest neighbour hopping

Given a system of isoenergetic sites randomly distributed in space with some concentration N_0, and if it is assumed that electron states for the system are strongly localised and the inequality $N_0\alpha^3 << 1$ (where α is the localisation radius) is fulfilled, then electrons hop between spatially nearest sites and hence this transport mode is

often called nearest neighbour hopping [28, 64]. Nearest neighbor hopping takes place in many real systems at high enough temperatures, T, when the thermal energy, $k_B T$, is larger than the energy scale ε_0 of the density of states [62]. In such a situation, the energy of the localised sites does not limit the charge transport. Hopping rates are influenced mainly by the spatial localisation of the sites.

Charge transport via nearest neighbour hopping is best explained by percolation theory [58-59]. Under this theory, a pair of sites is regarded as connected if the relative separation between the sites is smaller than a maximum distance R_c. Due to the exponential nature of the relationship between transition rates and distance between sites, excitation of carriers over distances $r < R_c$ are more pronounced than those over distances R_c. In this context, fast transitions are not a limiting factor for charge transport and hence can be ignored in the calculation of the conductivity of the system [58]. The slowest transitions occur over R_c and are the slowest among those necessary for DC transport; hence such transitions limit the conductivity [31, 58-59]. A schematic for a percolation cluster structure highlighting a typical transport path consisting of connected hopping sites is shown in Fig. 3.6. A variety of theoretical arguments [59, 62] give for R_c in three dimensional space the relation

$$R_c = \left(\frac{3B_c}{4\pi N_0} \right)^{\frac{1}{3}}, \tag{3.16}$$

where $B_c = 2.7 \pm 0.1$ is the average number of neighbouring sites available within the distance smaller than R_c [2, 31]. The transport path consists of connected sites with an energetically expensive transition occurring over the approximate distance R_c. Substituting R_c from equation (3.14) for R_{ij} in equation (3.15), one obtains the variation of conductivity with the number of localisation sites per unit volume.

Thus, $$\sigma = \sigma_0 \exp\left(\frac{-\delta}{\alpha N_0^{\frac{1}{3}}} \right). \tag{3.17}$$

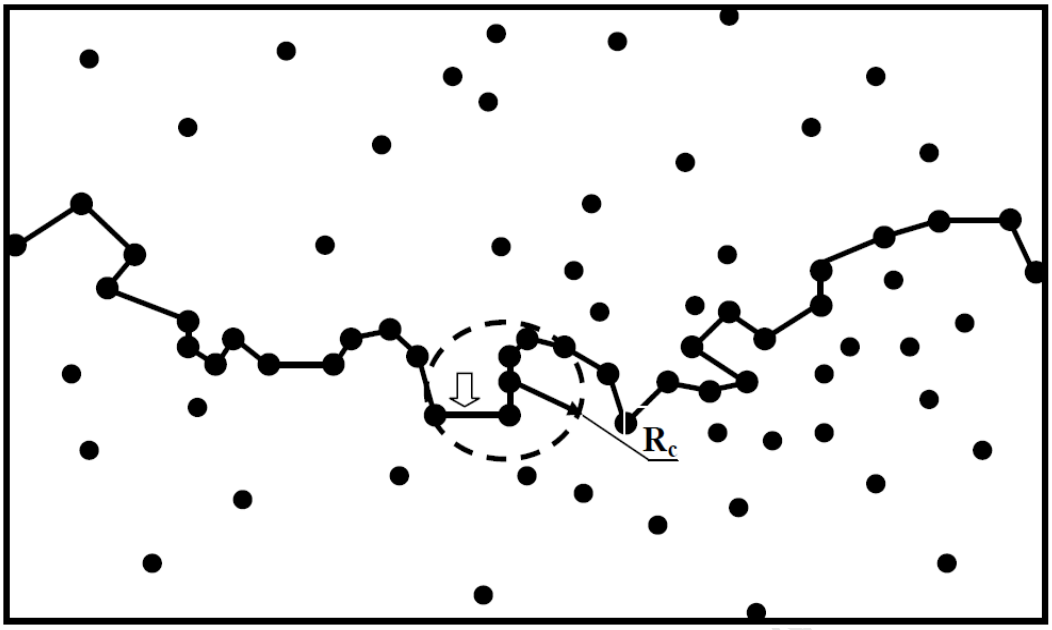

Fig. 3.6: Schematic of a transport path consisting of connected sites. Circles represent localised states. The block arrow indicates the most "difficult" transition over distance R_c [62].

Here, the pre-exponential factor, σ_0 is independent of the electron concentration and $\delta = 1.73 \pm 0.03$ is a numerical constant [21]. Equation (3.15) gives the dependence of conductivity on the concentration of localised states in the nearest neighbour hopping regime [60]. The equation assumes that only spatial factors influence hopping of electrons between localised states. This is true only at high temperature where the energy of the localised sites does not differ by more than $k_B T$. If the temperature is not as high, the relationship between energy-dependent and distance-dependent considerations affects the conductivity. Energy dependent factors such as the relative energies of the hopping sites become more important at low temperature. If the spatially nearest-neighbour sites have very different energies as shown in Fig. 3.7, it would be more energetically favourable for the electron to hop to a further site of energy closer to the initial one than to the nearest neighbour [2, 62].

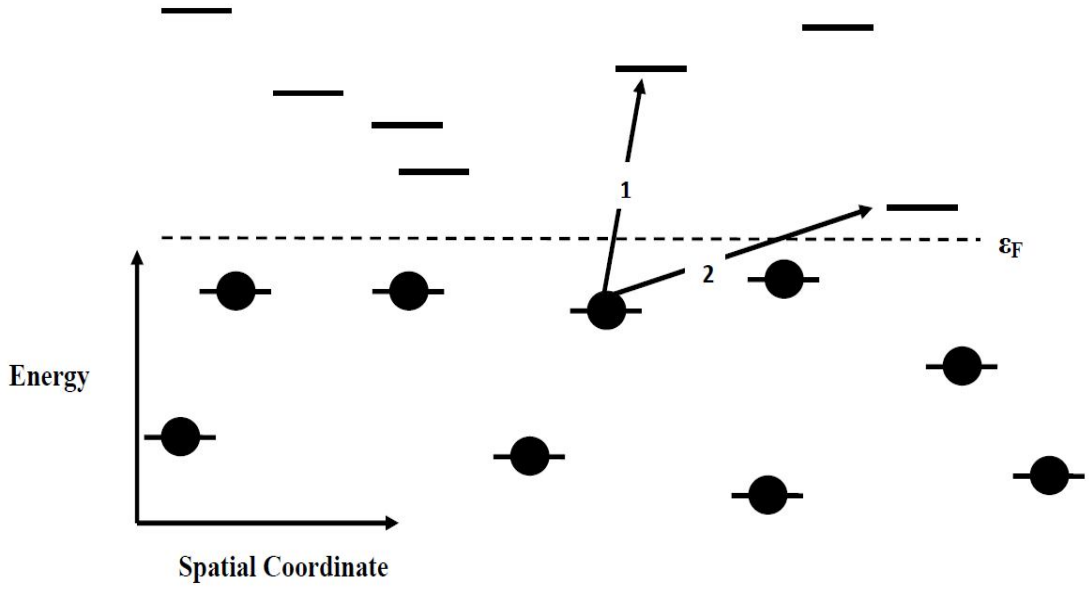

Fig. 3.7: Two possible hopping transitions between occupied states and unoccupied states. The dashed line depicts the position of the Fermi level, ε_F. Solid circles represent occupied states [62].

In transitions (1), a charge carrier hops to a nearest energy state though higher in energy. This corresponds to nearest neighbour hopping. In transition (2), the carrier hops to an energy state which is closest in energy to its initial state though further away. This represents the variable range hopping regime. For this reason, the span of transitions increases with decreasing temperature. This charge transport system is called variable range hopping, and this is explained further in the next section.

3.3.3 Variable range hopping

The concept of variable range hopping was put forward by Mott [4] for amorphous materials. He argued that at low temperatures, the most efficient electron transitions for charge transport are those in the neighbourhood of the Fermi energy level, ε_F, since only in this energy range can filled and empty states with close energies be found. For a region in the vicinity of the Fermi level with width $2\Delta\varepsilon$ symmetric with respect to ε_F (Fig. 3.8), the relation [4]

$$g(\varepsilon_F)\Delta\varepsilon r^3(\Delta\varepsilon) \approx 1, \tag{3.18}$$

can be used to estimate the energy width of the efficient strip for electron transport [4, 62].

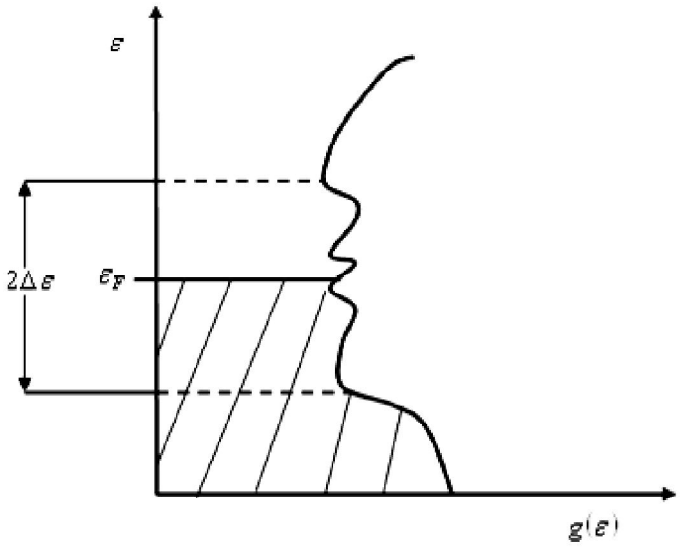

Fig. 3.8: Effective region in the vicinity of the Fermi level, ε_F, where the charge transport takes place at low temperatures [62], $g(\varepsilon)$ is the DOS function.

Here it is assumed that the energy width $2\Delta\varepsilon$ is small and the DOS function $g(\varepsilon)$ is nearly constant in the range $\varepsilon_F \pm \Delta\varepsilon$. The typical hopping distance then becomes

$$r(\Delta\varepsilon) \approx \left[g(\varepsilon)\Delta\varepsilon\right]^{\frac{-1}{3}}, \tag{3.19}$$

Giving a typical hopping rate of

$$\gamma_{ij} = \nu_0 \exp\left(\frac{-2}{\left[g(\varepsilon)\Delta\varepsilon\alpha^3\right]^{\frac{1}{3}}} - \frac{\Delta\varepsilon}{k_B T}\right). \tag{3.20}$$

For maximum hopping rate $\frac{d\gamma}{d\varepsilon} = 0$, thus the optimum energy width is

$$\Delta\varepsilon = \left[\frac{2k_B T}{3g^{\frac{1}{3}}(\varepsilon_F)}\right]^{\frac{3}{4}}. \tag{3.21}$$

Substituting (3.21) in (3.20) gives the Mott formula for temperature-dependent conductivity in the variable range hopping regime as [4, 62]

$$\sigma = \sigma_0 \exp\left(\frac{-T_0}{T}\right)^{\frac{1}{4}}, \tag{3.22}$$

where T_0 is the characteristic temperature given by

$$T_0 = \frac{\beta}{k_B g(\varepsilon_F)\alpha^3}, \tag{3.23}$$

and β is a numerical constant. A direct implication of the Mott law is that the density of states in the neighbourhood of the Fermi level is constant. However due to long range electron-electron interaction between localized states a gap, may appear in the vicinity of the Fermi energy [63, 65]. This gap may take a parabolic shape in the DOS [65] (Fig. 3.9) and the DOS function then assumes the form

$$g(\varepsilon) = \frac{\eta\kappa^3}{e^6}(\varepsilon - \varepsilon_F)^2, \tag{3.24}$$

where κ is a dielectric constant, e is the elementary charge and η is a numeric constant. At low temperature, the parabolic density of states vanishes exactly at the Fermi energy. With rising temperature, the gap disappears.

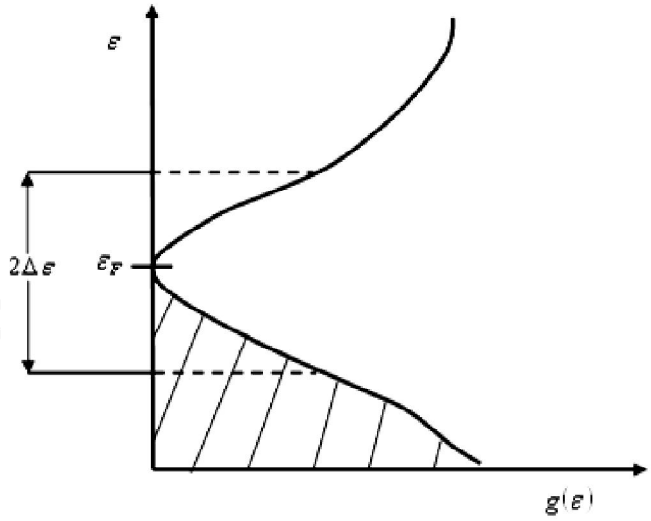

Fig. 3.8: Illustration of the coulomb gap [62].

The presence of the coulomb gap essentially modifies the hopping conductivity in the VRH regime [60]. In the presence of the coulomb gap and using the parabolic energy dependence of the DOS function [60],

$$\sigma = \sigma_0 \exp\left(\frac{-\tilde{T}_0}{T}\right)^{\frac{1}{2}}, \tag{3.25}$$

where $\tilde{T} = \frac{\tilde{\beta} e^2}{\kappa \alpha k_B}$, and $\tilde{\beta}$ is a numerical constant.

However equations (3.22) and (3.25) are of little help for the analysis of charge transport in disordered materials. The equations are two cases of constant DOS or a parabolic DOS in the energy range essential for hopping conduction. In non crystalline materials, the distribution of localised states is described by a DOS function which has a much stronger dependence than a parabolic one. The energy dependence of the DOS function is believed to be exponential in amorphous, vitreous and microcrystalline semiconductors, while in organic materials, it is usually assumed to be Gaussian [59]. In such cases new concepts are necessary in order to describe the hopping conduction.

3.4 Charge transport in percolation systems

Structurally disordered systems have been comprehensively modelled using percolation [66-67]. Highlights of materials where percolation has been applied range from transport in amorphous [67], porous media [68] and composites [69], to the properties of branched polymers, gels and complex ionic conductors [70-71]. Percolation has been proven to show universality [72-73]. This means that the large scale behaviour of percolation systems can be described by relatively simple mathematical relationships which are wholly independent of the small scale construction. For charge transport in a disordered system, the percolation problem reduces to exploring possible means to compute the conductivity of the system or at least its useful form [66, 70, 73].

3.4.1 Percolation

In the array of squares indicating percolation sites as shown in Fig. 3.10 (a), the fraction of the occupied states are marked with a cross whereas the other squares are left empty as in Fig. 3.10 (b). A cluster is then defined as a group of neighbouring squares occupied by these crosses [70]. The clusters are identified in Fig. 3.10 (c).

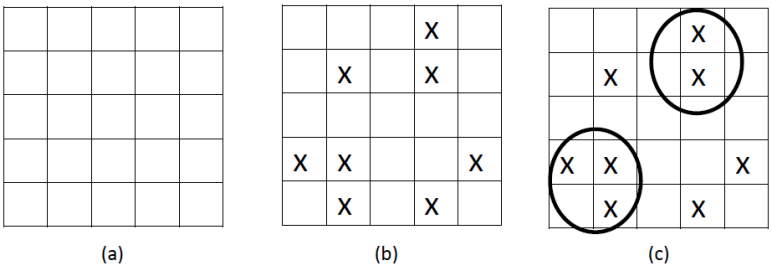

Fig 3.10: Definition of percolation (a) sites, (b) occupied sites and (c) clusters [70].

Squares with one side in common are regarded as nearest neighbours. If they only touch at one corner they are called “next nearest neighbours” [73]. There are two models that are handy in describing percolation phenomena. These are site percolation and bond percolation. The choice of model depends on whether the sites are connected or uncoupled. The subsequent sections describe the main features of these models.

3.4.2 Site percolation model

If the occupied sites are electrical conductors and empty sites are insulators, then charges can move between nearest neighbour conductor sites. Two conductor sites belong to the same cluster if they are connected by a path of nearest neighbour conductor sites and a current can flow between them [47, 66]. If the occupation probability for conductor sites is high, many conducting paths between the opposite edges exist where electrical current can flow. Defining the probability of occupation for sites as p, or for empty sites $1-p$. At low p, there will be no conducting paths between opposite edges of the lattice and the material is an insulator or highly resistive. Between the extremes of high and low p values, there exists a threshold concentration or probability p_c where electrical current can percolate from one edge of the lattice to the other. Percolation has thus three distinct phases namely subcritical if $p < p_c$, critical if $p = p_c$ and supercritical if $p > p_c$ [67, 69-70, 74].

Unlike thermal phase transitions where transition between two phases occurs at a critical temperature [75-76], the percolation transition is a geometrical transition characterized by the geometrical features of large clusters in p_c. When p is low, only small clusters of occupied sites exist. As p increases, the average size of the clusters

increases. At $p = p_c$, a large cluster is formed which provides at least one conducting path connecting opposite edges of the cluster [73]. This large cluster is called the infinite cluster [66, 69, 73]. As p continues to increase, eventually all sites belong to the infinite cluster. The critical concentration, p_c increases for the same dimension of the lattice. However, p_c decreases with increase in dimension of the lattice for the same coordination number [66, 73]. For $p < p_c$, the probability, P that a site belongs to an infinite cluster is zero and increases as $p > p_c$ as [72, 73]

$$P \sim (p - p_c)^t . \tag{3.26}$$

The linear size of the finite clusters below and above p_c is characterized by the correlation length, λ. The correlation length is a characteristic length scale in percolation and is the average distance between two sites on the same cluster [73] and

$$\lambda \sim |p - p_c|^{-f} . \tag{3.27}$$

The parameters t in equation (3.26) and f in equation (3.27) are universal and are dependent on the dimension of the lattice where as p_c depends explicitly on the type of lattice. A schematic representation of λ and p_c is shown in Fig 3.10. For length scales $r < \lambda$, the finite cluster and infinite cluster are self similar [66, 73]. This means that if a small part is cut out of the infinite cluster, enlarged and compared with the large cluster, the two will look identical. Due to the self similarity of clusters, they are characterized by a fractal dimension [77-78] which is smaller than the dimension of the embedding lattice [69, 72-73, 76]. The average mass of the cluster, M, in a circle of radius r, follows [73]

$$M(r) \sim r^{d_f} \ , \ r << \lambda , \tag{3.28}$$

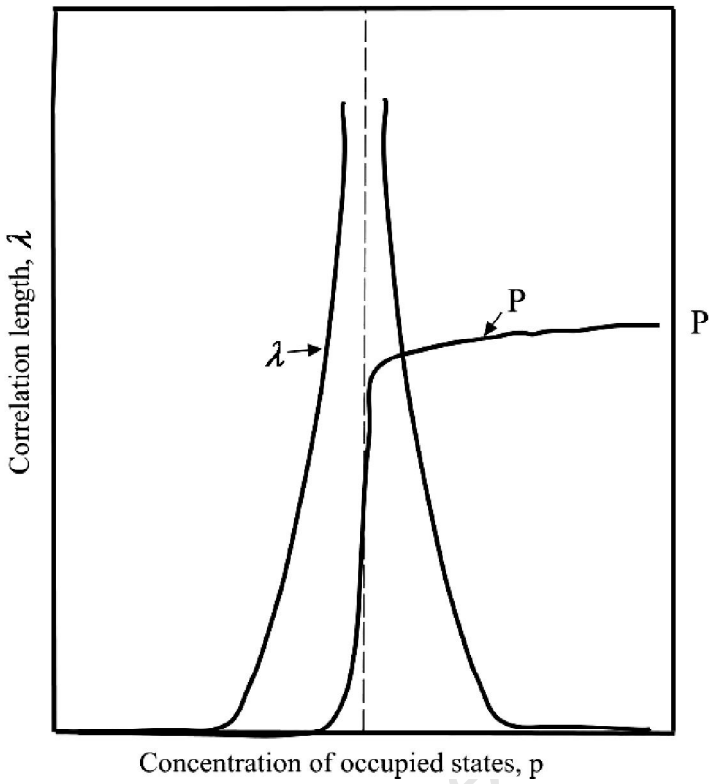

Fig. 3.11: Probability, P, and correlation length λ, versus concentration of occupied sites [66].

where d_f is the fractal dimension which provides a measure of how well a given fractal objects fills space. For $r >> \lambda$, the infinite cluster can be regarded as a homogeneous system. Thus, [76-79]

$$M(r) \sim \begin{cases} r^{d_f} & , \quad r << \lambda \\ r^{d} & , \quad r >> \lambda \end{cases} . \tag{3.29}$$

3.4.3 Bond percolation model

Site percolation results when sites of a lattice have been occupied randomly. When the sites are all occupied but the bonds between are randomly occupied with probability q, we have a situation of bond percolation. If a path of connected bonds connects two occupied sites, then those two connected bonds belong to the same cluster [66, 73]. The critical concentration, q_c of the bonds separates a phase of finite clusters of bonds from a phase with an infinite cluster [73]. If sites are occupied with probability p and bonds are occupied with q, then site-bond percolation results [75].

If the positions of the two components of a random mixture are not restricted to the discrete sites of a regular lattice, continuum percolation takes place [73].

3.4.4 Percolation substructures

The diagram in Fig. 3.12 shows a section of a bond cluster on a square lattice at p_c. If the bonds are resistors and if a voltage is applied between the points A and B of the cluster, then many bonds carry no current because they lead nowhere. These are called "dangling" or "dead ends" [67, 77].

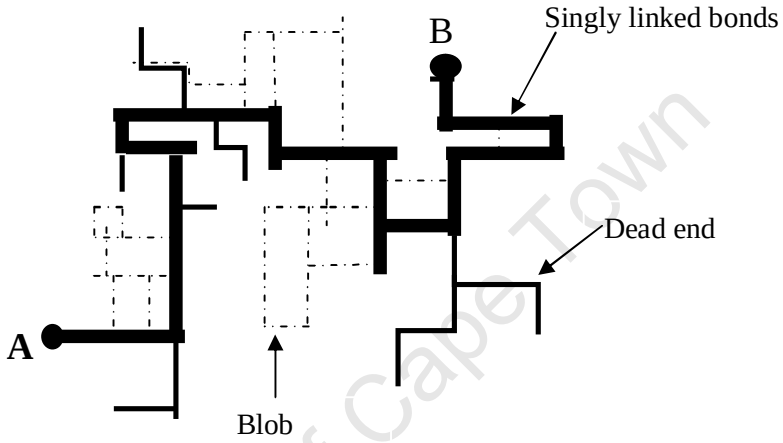

Fig. 3.12: Section of a cluster at p_c showing dead bonds, Blobs and singly connected bonds [73].

If the dangling bonds are disregarded, the conducting path is the remaining backbone [70, 73, 80]. All bonds on the backbone will carry some current when a voltage is applied between the left and right edges of the cluster. Most of the mass of the infinite cluster is concentrated in the dead ends and not the "bus bar" geometry of the backbone [81]. Accordingly most of the mass in the infinite cluster makes no contribution to the conductivity. Of the backbone, there are those links that carry current such that when they are cut, the current stops. These bonds are called singly connected bonds [73, 80], and are drawn in thick lines in Fig. 3.10. The singly connected segments are usually separated by structures which contain several routes in parallel [73, 80-81]. These are often called "blobs" [81], and are shown as broken lines in Fig. 3.12.

In general, the existence of the singly connected bonds proves the existence of a generalized link between neighbouring nodes. Although the length of each singly

connected segment is finite, the blobs have possible sizes up to λ [73]. This description leads to the "links-nodes-blobs" picture [82].

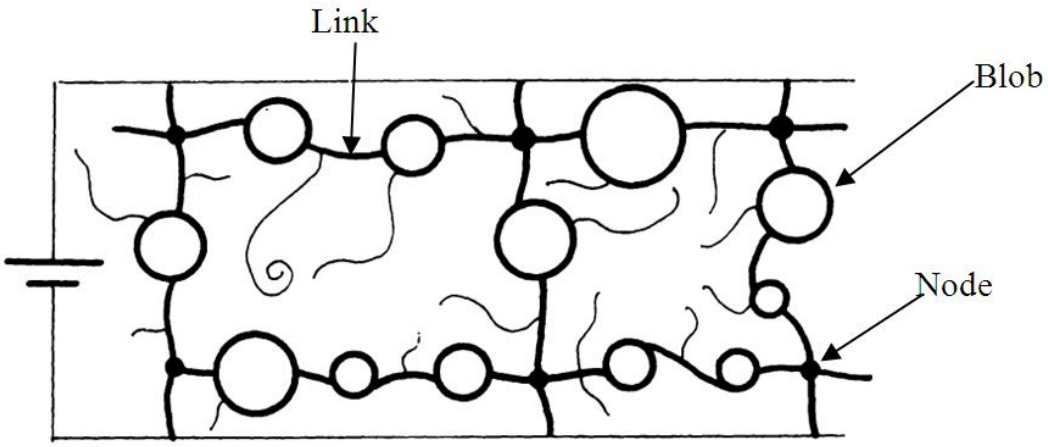

Fig. 3.13: Schematic picture of the "links-nodes-blobs" model of an infinite cluster with $p > p_c$ [82].

This model which is schematically represented in Fig. 3.13 is the basis for the analysis of conductance in a percolation network.

3.4.5 The resistor network problem

Percolation theory is closely related to the hopping theory discussed in section 3.3 [66, 72]. This is supported by the fact that under the hopping theory, there exists a critical separation below which the conducting sites can be regarded as touching thereby forming a network of interconnected conductive material through which current can percolate [80-81, 83-84]. Moving from a hopping system to a resistor network can be achieved by turning the hopping rates into equivalent resistors [67, 85-86]. The conductance G_{ij} between two sites can be written as [67, 86]

$$G_{ij} \approx G_0 \exp\left(-2\gamma\left|R_{ij}\right| - \frac{E_{ij}}{k_B T}\right), \tag{3.30}$$

where E_{ij} is the activation energy for transition of carriers between site i and site j. Suppose we define a critical conductance, G_c at the percolation threshold. The critical conductance is expected to contain all the functional behaviour of the entire network.

An approximate relationship between G_c, the maximum hopping distance and maximum hopping energy can be given by [71, 85, 87]

$$\begin{aligned} G_c &= \frac{ev_0}{k_B T}\exp\left(-2\gamma R_{\max}\right) \\ &= \frac{ev_0}{k_B T}\exp\left(\frac{-E_{\max}}{k_B T}\right) \\ &\cong G_0 \exp\left(\frac{-E_c}{k_B T}\right) \end{aligned} \quad , \tag{3.31}$$

where v_0 is a normalization factor which can be taken to be the phonon vibration frequency and γ is the wave function decay constant.

For a regular network of random valued conductances, g_{ij} with v_i being the voltage at the i^{th} node, Kirchhoff's current law gives [66, 70]

$$\sum_i g_{ij}\left(v_i - v_j\right) = 0 . \tag{3.32}$$

The percolation resistor network model is applicable to a system where hopping characterises the charge transport [70, 86]. In addition to information about the conductances of the critical paths, this model also gives some insight into the size of barriers to charge transport [70, 87]. Under conditions of an infinite cluster, there will be connectivity between sites as defined by bond percolation. Each of the bonds then can be treated as a resistor giving rise to a network of conductances spanning the entire cluster. For the sites that are not connected, charge moves through hopping. Eventually the charge transport will be described by hopping and percolation.

3.5 Hall effect in percolation systems

In the discussion so far, hopping is considered as the basic mode of charge transport in a percolation network. The conductivity has been shown to follow Arrhenius and/or non-Arrhenius temperature dependence depending on the temperature regime and nature of the nanocomposite material. In general, variable range hopping has been shown to be confined to low temperatures, while nearest neighbour hopping is common at high temperature. Pure Arrhenius type conductivity shall be shown to be

characteristic of silicon nanoparticle networks over an extended temperature range. In addition to analysing the conductivity of these inhomogeneous materials, Hall effect measurements are important to complement the understanding of the electrical transport properties. The Hall effect has commonly been used for many years to measure the transport properties of single crystalline semiconductors [88-90].

The Hall effect is the generation of a voltage difference, V_H across a semiconductor placed perpendicular to a magnetic field, $\vec{B}$ that is transverse to the current as shown in Fig. 3.14.

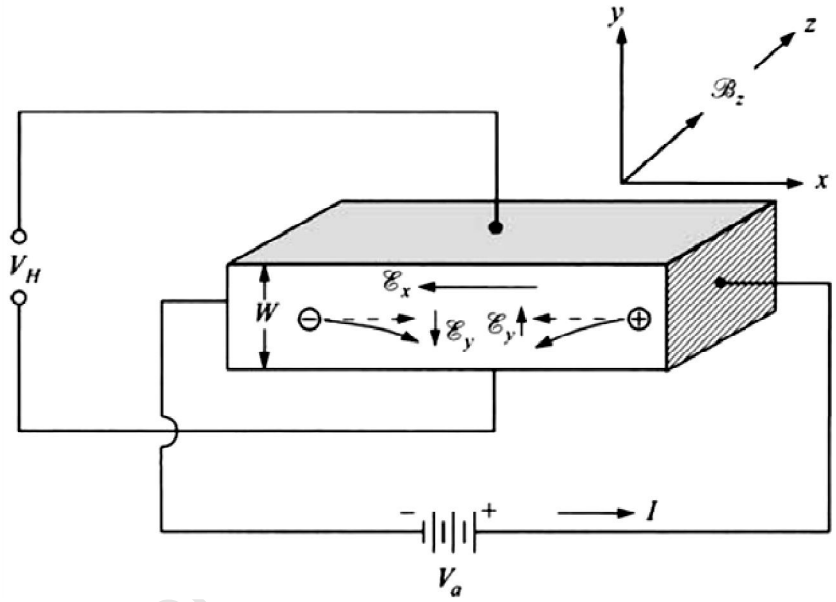

Fig. 3.14: Principle of the Hall effect [26]

As explained in chapter 2, for semiconductors with both electrons and holes, the drift current density under an applied field $\vec{E}$ is given by

$$J = \sigma E = q\left(\mu_n n + \mu_p p\right)\vec{E}\,, \tag{3.33}$$

and the conductivity becomes

$$\sigma = \frac{1}{\rho} = q\left(\mu_n n + \mu_p p\right)\vec{E}\,, \tag{3.34}$$

where ρ is the resistivity. Suppose $n >> p$ (i.e. *n*-type semiconductor), then

$$\rho = \frac{1}{q\mu_n n}, \tag{3.35}$$

and $$\sigma = q\mu_n n. \tag{3.36}$$

From Fig. 3.14 suppose the sample is *p*-type. The holes experience a downward force given by

$$F = qv_x \times \vec{B}_z. \tag{3.37}$$

The holes accumulate up at the bottom side of the sample as shown in the diagram [91]. This creates an electric field, $\vec{E}_y$ along the positive y axis. For an *n*-type sample, electrons will also accumulate at the bottom surface setting up a voltage of opposite polarity. For the presence of *p*- and *n*-type carriers, the net current density is given by

$$J = nq\mu_n\left(\vec{E} + \vec{v}_n \times \vec{B}\right) + pq\mu_p\left(\vec{E} + \vec{v}_p \times \vec{B}\right), \tag{3.38}$$

and under steady state conditions, the current density in the *y* direction is zero. For holes the carrier velocity is related to the current density by

$$J_x = qv_x p. \tag{3.39}$$

Under steady state conditions, the electric field along the y direction balances exactly the Lorentz force such that the carriers travel parallel to the applied electric field E_x. Thus

$$qE_y = qv_x B_z, \tag{3.40}$$

and

$$V_H = E_y W = \frac{J_x B_z W}{qp}. \tag{3.41}$$

If we take into account scattering of carriers, [26, 92]

$$V_H = R_H J_x B_z, \tag{3.42}$$

where R_H is the Hall coefficient given by

$$R_H = \frac{r_H}{qp} \text{ if } p >> n, \tag{3.43 (a)}$$

$$R_H = \frac{-r_H}{qn} \text{ if } n >> p. \tag{3.43 (b)}$$

and r_H is the Hall factor given by

$$r_H = \frac{\langle \tau_m^2 \rangle}{\langle \tau_m \rangle^2}, \tag{3.45}$$

and τ_m is the mean free time between collisions for charge carriers [26]. Equations (3.44 (a)) and (3.44 (b)) assume conduction by a single type of carrier. The Hall coefficient for two types of carriers will be described by [92-93]

$$R_H = \frac{r_H}{q} \frac{\mu_p^2 p - \mu_n^2 n}{q(\mu_p p + \mu_n n)^2}. \tag{3.46}$$

It can be seen in equation (3.46) that the sign of R_H reveals the majority carrier type of the material. The Hall mobility is given by

$$\mu_H = |R_H| \sigma. \tag{3.47}$$

Hall mobility differs from drift mobility, μ which does not contain the Hall factor, r_H . They are related by the equation

$$\mu_H = r_H \mu, \tag{3.48}$$

and r_H typically ranges between 1 and 2 and is slightly below 1 at high fields. The Hall factor is different for both carriers due to their different effective masses. It depends on the scattering mechanisms in a material.

Hall effect measurements are reasonably straight forward for single crystalline materials [94]. Inhomogeneous materials such as polycrystalline materials are characterised by many interfaces which give rise to a random distribution of barriers to current flow or result in carrier depletion. For geometric reasons, the current is then constrained to flow in non-uniform patterns, limiting the effective mobility [94]. Electric current will follow preferred paths determined by a percolation process [95-

96]. Efforts to provide a comprehensive explanation to the observed anomalous Hall effect in percolation networks have not been univocal. However Skal and Shloviskii [97] and Levinshtein et al [98] converged at the conclusion that for two dimensional networks, the Hall coefficient is constant. This was also in agreement with the prediction by the effective medium theory [99]. For materials in which the transport is determined by hopping, there is an anomaly in the sign of the Hall coefficient [100].

In general, the Hall mobility for disordered materials is temperature activated and is given by

$$\mu_H = \mu_0 \exp\left(\frac{-\Phi}{k_B T}\right), \tag{3.49}$$

where the pre-exponential factor μ_0 shows weak temperature dependence [97].

4 Experimental techniques

This chapter describes the synthesis and characterisation of electrically active silicon nanoparticles, formulation of the silicon inks, printing and characterisation of the printed layers through to the electrical measurements performed on the printed silicon. Primarily the nanoparticles used were produced by high energy milling. For comparison, boron doped *p*-type silicon nanoparticles produced by chemical vapour synthesis (CVS) [1], were characterised using the same techniques.

4.1 Powder production

Silicon nanoparticles were produced by the milling of bulk silicon using an 800W Siebtechnik laboratory disc mill. This is a high energy vibratory mill equipped with a four way adaptor to accommodate four milling vessels.

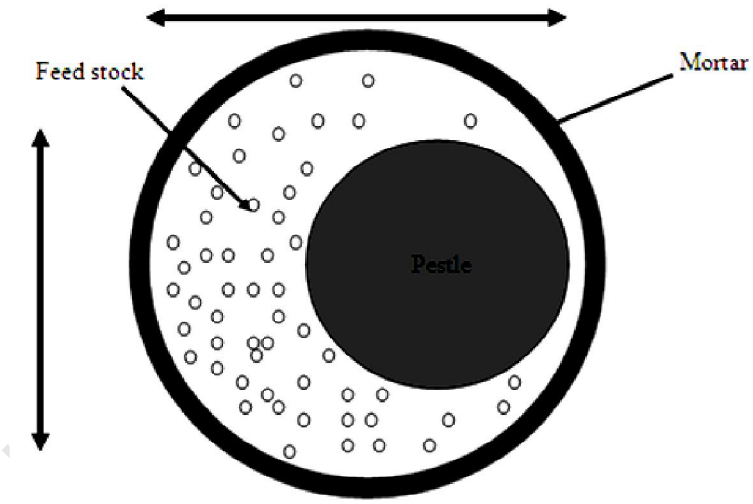

Fig. 4.1: Milling action inside a milling vessel of the vibratory pulveriser.

Each of the pots consists of a cylindrical cavity (mortar) of inner diameter 8 cm and depth of 3.7 cm. The pestle has a diameter of 5.5 cm, height of 3.3 cm and a mass of about 0.6 kg. The lids are fitted with O-rings to provide a seal. When mounted on the four way adaptor they are clamped under a rubber pad and a heavy metal plate. The milling vessels and pestles are made of 5200 chrome steel. The vibratory action of the mill results in the fixed pots vibrating in two axes as represented schematically in Fig. 4.1. This in turn sets the pestle into rotational and lateral motion, hammering the silicon against the mortar to produce progressively smaller particles. In this study, the feedstock materials for the milling were 2503 metallurgical grade

silicon supplied by Silicon Smelters, Polokwane, South Africa, and Czochralski grown *p*- and *n*-type silicon wafers of resistivity 0.01-0.05 Ω cm supplied by Siltronix, St Louis, USA. Both types of feedstock material were used essentially in the form supplied except that they had to be broken into smaller pieces of centimetre dimensions before loading into the pots. According to the manufacturer's analysis, the purity of the 2503 metallurgical grade silicon is 99.4 %, with the main impurities being Fe at 0.21 % and Al at 0.144 %. Other specified impurities were Ca, Ti, Cr, P, and Ni with concentrations, in ppm, of 230, 129, 62, 43 and 18 respectively. Before loading the silicon, the pots were cleaned by milling quartz for 15 minutes after which the contaminated quartz was discarded and the remaining quartz dust removed with dry compressed air. The pots were subsequently cleaned with acetone and then with ethanol. Each pot was then loaded with silicon and the pots closed for dry milling. Milling was performed continuously for 5 hours except for interruptions to monitor the clamping of pots. On completion of the milling, the pots were allowed to cool down to the ambient temperature of 20 - 25^{o}C before harvesting the powder in its dry state.

4.2 Characterisation of the powders

Transmission electron microscopy (TEM) and scanning electron microscopy (SEM) were used to study the morphology of the nanoparticles.

4.2.1 Morphology and internal structure of the silicon nanoparticles

A small amount of powder was dispersed in about 5 ml of ethanol in a test tube by sonication using a 100 W bath sonicator for one minute and an aliquot was immediately drawn from the centre of the suspension using a micropipette. The suspension was deposited on holey carbon coated TEM grids. This was followed by drying the grids in air at room temperature for 2 hours and then in an oven at 60 ^{o}C for 15 minutes.

A JEOL 2100 transmission electron microscope with a 200 kV acceleration voltage and LaB_6 filament was used in bright field mode at magnifications up to 30 000×, to determine the agglomeration, shape and crystallinity of the nanoparticles. The microscope has a point resolution of 0.2 nm and is equipped with a Gatan US1000, 2048 × 2048 pixel CCD camera. TEM images were taken at random from different positions on the TEM grids. Imaging of

samples was performed through focus starting with under focus, and ending at over focus conditions. Imaging of lattice planes near the surface was also performed at higher resolution.

4.2.2 Size distribution of nanoparticles produced by milling

Pellets of silicon powder were produced by loading about $0.5\,g$ of the silicon powder into a stainless steel cylinder and compressing the powder at a pressure of about 50 MPa using a hydraulic press. The pellets were 10 mm in diameter and about 3 mm thick. The compressed pellet was then placed on a microscope stub whose surface was covered with carbon glue. Care was taken not to break the pellet while at the same time ensuring that the pellet was stuck firmly to the stub. The prepared stubs were then mounted onto a sample holder and loaded into a Leica Stereoscan S440i SEM for analysis, in secondary electron mode at an accelerating voltage of 20 kV.

4.3 Ink formulation

The ink making procedure employed in this study was a simple but long process that ensured that all components of the silicon ink were mixed appropriately to achieve a stable ink [2, 3]. The binder used was a commercial acrylic ink base supplied by Marchem, Cape Town, South Africa. Mixing was performed by adding powder and thinner sequentially to the binder. Particle concentrations of 50%, 60%, 70%, 80%, and 88% by weight relative to the binder have been used for milled metallurgical grade silicon powder in this work. For the purpose of comparing the properties of printed metallurgical grade silicon, only 88% particle concentration was used for powder produced by chemical vapour synthesis (CVS), and milled *p* and *n*-type silicon wafers. The thinner used was reagent grade propan-1, 2 diol (propylene glycol) supplied by Sigma-Aldrich, Steinheim, Germany, which shall be referred to here as glycol. Rheological tests performed on the silicon inks have established that the inks show shear thinning behaviour as well as being partially thixotropic and viscoelastic [4]. The shear thinning behaviour is the main requirement for screen printing, and thus the silicon inks could all be screen printed. The printability of the ink was determined by measuring the contact angle of the ink on a glass surface using a contact angle goniometer [4]. The goniometer is equipped with a digital camera used to photograph the ink drop for measuring the contact angle. A photograph of a typical milled silicon ink drop deposited on a

microscope slide is shown in Fig. 4.2. Image J, an image analysis freeware package, was used to determine the contact angle. Two angles, θ_1 and θ_2 shown in Fig. 4.2, were measured between the planes tangent to the surface of the ink and the image of the ink surface mirrored by the glass slide.

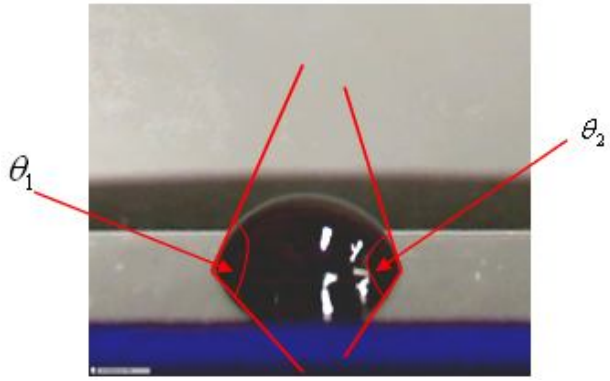

Fig. 4.2: Photograph of a 2503 metallurgical grade silicon ink drop placed on a microscope slide for contact angle measurement. The contact angle is the average of the semi angles of θ_1 and θ_2.

The contact angle was determined by calculating the average of the semi-angles corresponding to θ_1 and θ_2. Typically, contact angles on glass of 50 ± 5^{o} at ambient temperatures of $22 \pm 2\,^{o}\mathrm{C}$ and relative humidity of $50 \pm 5\%$ produced printable silicon inks.

A mass loss experiment was also performed to investigate the drying properties of the binder and solvent. This was achieved by placing a known mass of each material on 10 microscope slides and monitoring the change in mass over a period of 5 days. The analysis of the mass-time evolution of the components yielded information concerning the required duration for drying of a printed film.

4.4 Printing

An ATMA AT-60PD semi-automatic flatbed screen printer was used to print the test samples. Besides application of ink on to the screen, and mounting of substrate on to the print bed, the printing operation is fully automatic. A vacuum bed holds the substrate during a print stroke or during setting up as required by the operator. Squeegee speed, off-contact, and print stroke settings were adjusted digitally while other variables such as squeegee pressure and position of the vacuum table were adjusted manually using micrometer screws. The screens used were manufactured by Register Screen (Pty) Ltd, Cape Town, South Africa, and were

made from Sefar monofilament polyester fibre with a mesh count chosen according to the type of ink to be printed. A mesh count of 150 lines per cm was used for silver ink, and 100 lines per cm for silicon inks. In the case of silver screens, the mesh had a thread diameter of 31µm whereas for silicon screens the thread diameter was 40 µm. A photograph of a typical screen used is shown in Fig. 4.3. During screen manufacture, the mesh is stretched and fixed onto a rectangular aluminium frame of dimensions $70 \times 80\,\text{cm}^2$. The stretched screen is then coated with a dual purpose photoresist on both sides; with an additional layer of photoresist then applied to the bottom of the screen for good edge definition of the stencil. The design, which is printed on transparency, is then placed in the centre of the screen and the screen exposed to light. This is followed by washing the photoresist from the unexposed parts which correspond to the intended design. The average tension of the screens before use was 24.2 ± 2 N/cm for screens used to print both silver and silicon.

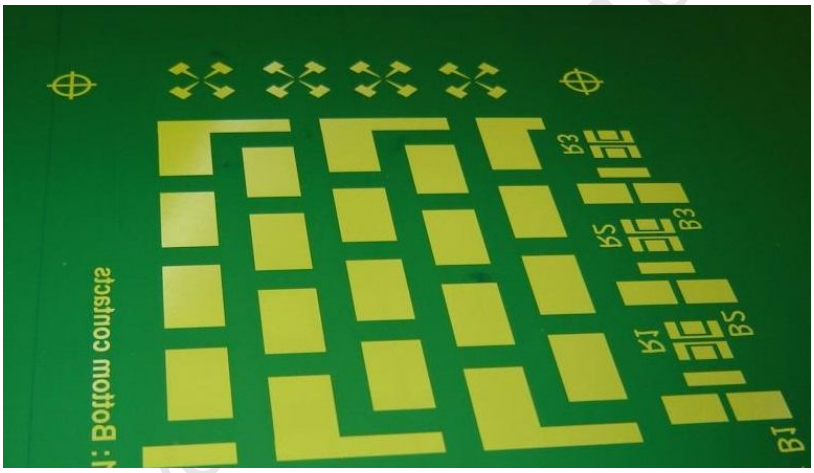

Fig. 4.3: Typical screen showing open and masked areas.

The yellow sections in Fig. 4.3 are open areas in the stencil through which ink can be printed. A trailing edge squeegee made of polyurethane of 70 Shore A hardness was used [5]. In this work the squeegee angle was set to 20^o giving a nominal angle of attack of 70^o as shown in Fig. 4.4 for both silver and silicon inks [6]. The metal contacts were printed with silver ink supplied by Dupont Microcircuit Materials. The substrate used was 80 gm^{-2} plain paper with no pre-treatment.

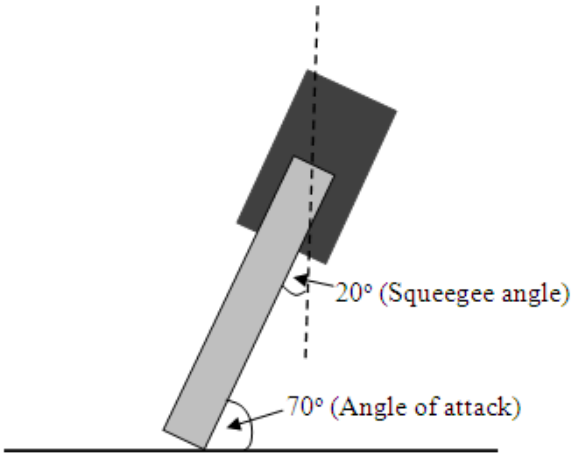

Fig. 4.4: Orientation of squeegee showing squeegee angle and angle of attack.

Using the ATMA AT-60PD screen printer, silver ink was printed using the minimum off contact setting, a squeegee angle of 20^{o} and a printing speed of $250mm/s$. A double stroke print mode was used to ensure a near uniform printed layer with no pinholes. The zero of the squeegee pressure was set by levelling the squeegee against the bed. A squeegee pressure setting of 2 mm was used to achieve uniform and reproducible printed layer quality. The silver contacts were allowed to dry for 24 hours under ambient conditions, before printing the nanoparticulate silicon inks. The sheet resistivity of selected silver layers was determined using a Lakeshore Hall effect measurement system in a van der Pauw geometry as described in section 4.8. For printing silicon inks, a squeegee speed of 200 mm/s was used for the same pressure setting. The screen tension was measured using a SEFAR TENSOCHECK 100 tensiometer before and after each print session to monitor changes in screen tension between print sessions. Printing was performed under prevailing ambient conditions of $22 \pm 2\,^{o}C$ and relative humidity of $50 \pm 5\%$. The printed silicon layers were allowed to cure under ambient conditions for at least 24 hours, before the structural and electrical characterisation was performed.

4.5 Structural characterisation of printed layers

The printed metal-semiconductor test structures were then analysed using optical microscopy, SEM and optical profilometry. Some of the printed samples were calendared to a thickness of about $10\,\mu m$ before analysis. Both top surface and cross-sectional imaging were performed using SEM. For surface analysis, squares measuring 5 mm×5 mm were cut out using a sharp stainless steel blade and fixed to 8mm diameter aluminium microscope stubs covered with carbon glue. These were then sputtered with gold palladium to avoid possible charging of the

surface. In the case of cross-sectional SEM samples, the cut samples were embedded into carbon glue on microscope stubs, with the clean cut face of the sample oriented upwards, and then sputtered with gold palladium. In another approach, to obtain the cross-sectional view of the printed layers, strips measuring 5 mm×5 mm were cut out from middle portions of the printed layers. These were then cast in a mould containing epoxy resin. The resin was then cured in an oven at 100 ^{o}C over a period of 24 hours. After curing, the topmost part of the sample was shaved off using a Reichert Leica Ultra-cut S Microtome equipped with a glass knife until a clear cross-sectional view of the sample was obtained. Silver ink was used to draw a line from one end of the exposed sample cross-section down the surface of resin to the carbon coated stub to reduce possible charging of sample. For all types of samples, both secondary electron imaging (SEI) and full quadrant backscattered electron detection (QBSD) imaging were employed.

In a separate experiment, a Wild Photomakroskop M400 optical microscope was used to provide an impression of the printed layers at magnifications of 6.5, 12.5, and 32X.

To ascertain the roughness of the printed layers, a Veeco NT9100 optical profiler was used in vertical step interferometry (VSI) mode to scan the surface topography of the printed layers.

4.6 Electrical characterisation

All electrical measurements were performed using a Lakeshore Hall system shown in Fig. 4.5. Essentially, it is a Hall effect measurement system (HMS) that can perform variable field and variable temperature magneto-transport measurements with high accuracy. This HMS is a collection of advanced integrated instruments and control software which include: a high precision voltmeter (Keithley 2182A Nanovoltmeter), a constant current source (Keithley 6220 precision current source), high precision ammeter (Keithley 6485 picoammeter), Lakeshore 642 Electromagnet Power Supply unit with electromagnet, Lakeshore 475 DSP gaussmeter, HMS Matrix amplifier, Lakeshore 340 temperature controller, cryostat with heating and cooling system.

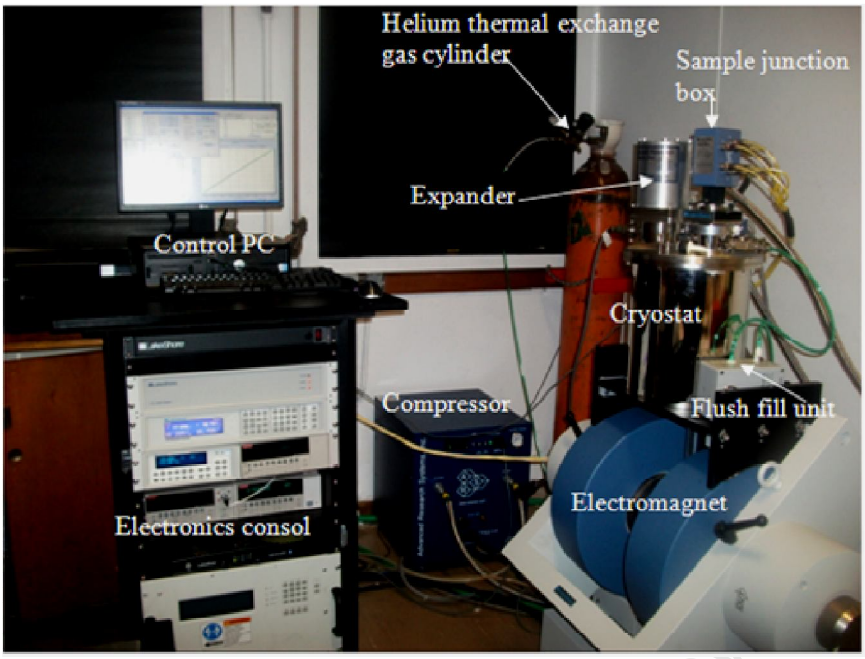

Fig. 4.5: The Lakeshore 75014 CCRSM Hall measurement system [7].

The HMS allows for completely automatic operation of the measurements by means of control software supplied by Lakeshore Inc.. The system is programmed to minimize thermal offsets during measurement by utilising a DC current reversal technique. A typical illustration of this capability is with the Keithley 6220 precision current source which works in conjunction with the Keithley model 2182A [7]. It provides a bipolar output current, providing a four quadrant source or sink operation, and the Keithley model 2182A performs analogue to digital conversions and uses an algorithm to provide the output of the measurement. The model 2182 is then able to measure voltage on both the positive and negative alterations of the current source. The average difference of the two readings cancels the thermal EMF component of the measurement. In addition, the model 6220 is capable of sweeping current and hence provides a facility to vary the current in predetermined steps. In a similar fashion, various field sweep methods, with field reversal to eliminate material resistivity errors, can be used to determine magnetoresistance, resistivity, Hall coefficient, mobility, four wire resistance, or hysteresis loops as may be relevant to a measurement. The Lakeshore software and the Lakeshore model 340 temperature controller are also capable of providing a stable temperature environment for samples. To understand how temperature control is achieved in the HMS, components of the operational schematic of the model 75014 CCRSM (closed cycle refrigeration sample module) are shown in Fig. 4.6.

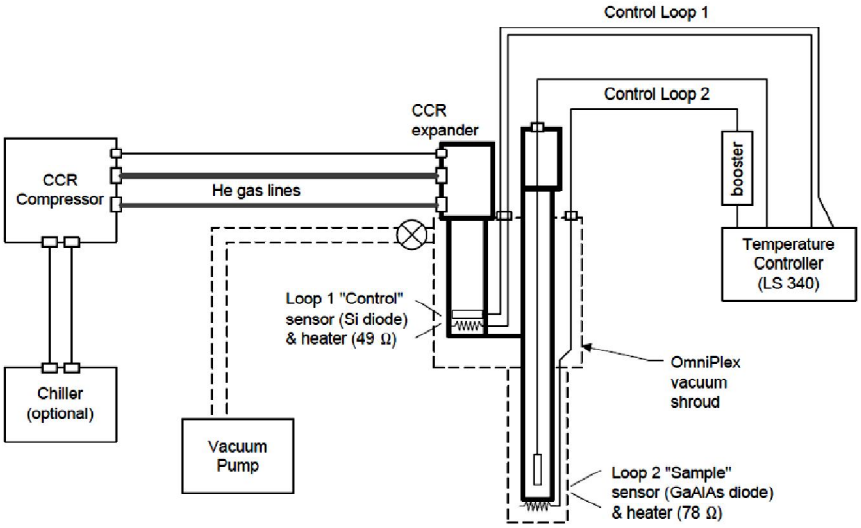

Fig. 4.6: Model 75014 CCSRM Operational schematic [7].

The HMS temperature control system is composed of two loops each consisting of a heater and a temperature sensor. These are designated loop 1 and loop 2 in Fig. 4.6. The cryostat is delineated in heavy lines in the diagram. The loop 1 heater, which is of higher power than loop 2 heater, controls the temperature of the cold head. The loop 2 heater and sensor are situated next to the sample. The sample temperature sensor is attached to the back of the sample card. The sample heater is used to precisely control the temperature of the sample. The function of other components in Fig. 4.6 will be described in later sections. The HMS controls temperature by means of the Lakeshore model 340 temperature controller. A typical temperature control system for a Lakeshore model 340 temperature controller is shown in Fig. 4.7. The model 340 integrates many of the elements of a complete control system [8, 9], but does not provide cooling. Hence the load (the cryostat) must accommodate a temperature sensor for feedback and a resistive heater for heating.

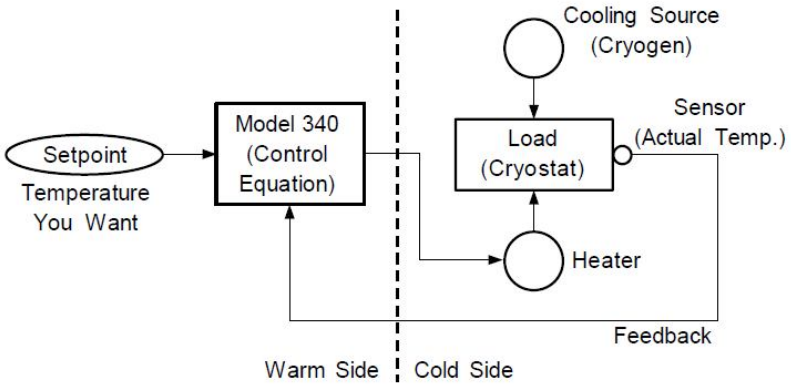

Fig. 4.7: Temperature control system with model 340 controller [8].

Using the feedback, the model 340 PID controller can implement a control equation with an algorithm that calculates the amount of heating needed to keep the load at the set point temperature [9]. Fig. 4.8 shows the response of the sensor temperature during a temperature change. Between times t_1 and t_2, the set point of both loop 1 and loop 2 is changed from the initial temperature to the final set point at a constant rate.

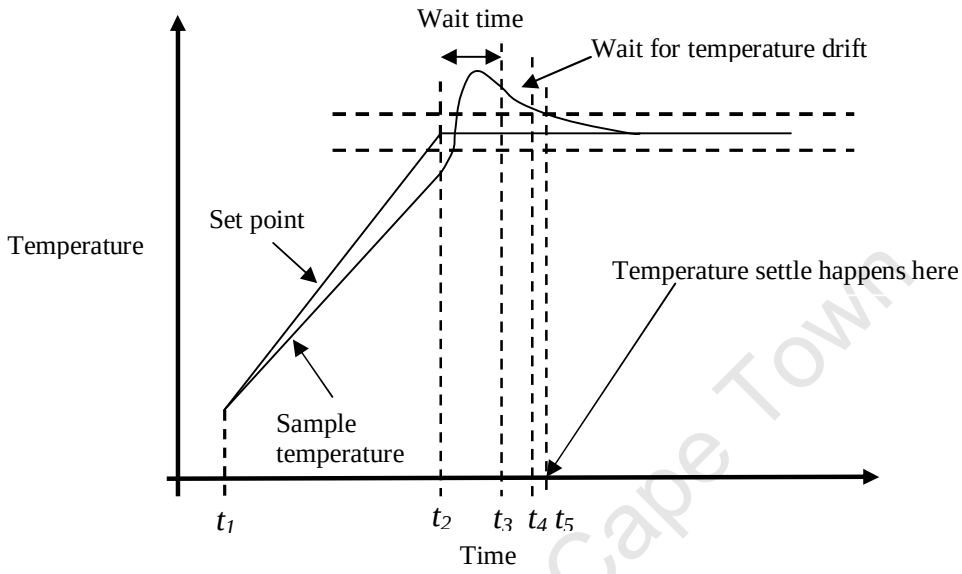

Fig. 4.8: Sample sensor temperature during set point ramping [9].

By t_2, the loop 1 temperature has already attained the set point temperature, but a waiting time period (t_2 to t_3) is allowed for the sample temperature as it overshoots. At t_3, the temperature drift, time derivative of the sample sensor temperature, is calculated along with the difference between the sample sensor temperature and the final set point. When the drift is less than a certain preset value (at t_4), and when the difference is less than the temperature band (at t_5), the system recognises the temperature as having settled and a measurement takes place.

To perform Hall effect measurements, the HMS can use two types of sample geometries: the Hall bar and the van der Pauw structure. The Van der Pauw technique can be used to measure the resistivity or Hall coefficient of a thin arbitrarily shaped sample with four Ohmic contacts placed on the periphery. There are five conditions that must be satisfied to use this technique [10, 11]:

- The sample must have a flat shape of uniform thickness.
- The sample can be of any shape but must be simply connected, i.e it must not have any holes or non-conducting islands or inclusions.

- The sample must be homogeneous and isotropic
- All four contacts must be located at the edges of the sample
- The area of the contact must be at least one order of magnitude smaller than the area of the entire sample.
- The sample thickness must be much less than the width and length of the sample and it is preferred that the sample be symmetrical to reduce errors in the calculations.

Uniformity and homogeneity of the printed layers was guaranteed by calendaring layers of 80% particle loading which were well above the upper percolation threshold for the printed silicon. Contacts to the printed layers were symmetrically arranged (see Fig. 4.10) and the ratio of the size of the contacts to the diameter of the printed circular test structure was about 0.1, which complied with the van der Pauw criteria.

The HMS performs measurements on the van der Pauw structure over two regions, A and B, as shown in Fig. 4.9.

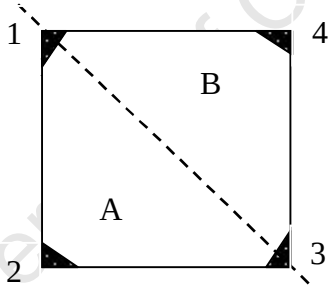

Fig. 4.9: van der Pauw geometry.

Defining the sample geometry in this way enables the measurement system to do the necessary current reversal permutations to eliminate thermal voltage offsets and misalignment errors. To illustrate how the HMS calculates the electronic transport parameters, consider the geometry shown in Fig. 4.9. Let V^{+}_{ijkl} indicate a voltage measured across terminals k and l, with k positive, while a positive current flows into terminal i and out of j. First the system calculates two resistivities, ρ_A and ρ_B as

$$\rho_A = \frac{\pi f_A t}{\ln 2}\left\{\frac{V^{+}_{12,43} - V^{-}_{12,43} + V^{+}_{23,14} - V^{-}_{23,14}}{I^{+}_{12} - I^{-}_{12} + I^{+}_{23} - I^{-}_{23}}\right\}, \tag{4.1}$$

and

$$\rho_B = \frac{\pi f_B t}{\ln 2}\left\{\frac{V^+_{34,21} - V^-_{34,21} + V^+_{41,23} - V^-_{41,23}}{I^+_{34} - I^-_{34} + I^+_{41} - I^-_{41}}\right\}. \tag{4.2}$$

It then proceeds to calculate geometrical factors f_A and f_B which are functions of resistance ratios Q_A and Q_B respectively, given by

$$Q_A = \left(\frac{R^+_{12,43} - R^-_{12,43}}{R^+_{23,14} - R^-_{23,14}}\right) = \left(\frac{V^+_{12,43} - V^-_{12,43}}{I^+_{12} - I^-_{12}}\right)\left(\frac{I^+_{23} - I^-_{23}}{V^+_{23,14} - V^-_{23,14}}\right), \tag{4.3}$$

and

$$Q_B = \left(\frac{R^+_{34,21} - R^-_{34,21}}{R^+_{41,23} - R^-_{41,23}}\right) = \left(\frac{V^+_{34,21} - V^-_{34,21}}{I^+_{34} - I^-_{34}}\right)\left(\frac{I^+_{41} - I^-_{41}}{V^+_{41,23} - V^-_{41,23}}\right). \tag{4.4}$$

If either Q_A or Q_B is greater than 1, the reciprocal is used. f and Q are related through the equation

$$\frac{Q-1}{Q+1} = \frac{f}{\ln 2}\cosh^{-1}\left\{\frac{1}{2}\exp\left[\frac{\ln 2}{f}\right]\right\}, \tag{4.5}$$

which can be solved numerically. Ideally the two resistivities ρ_A and ρ_B should agree to within 10%. The average resistivity is given by

$$\rho_{av} = \frac{\rho_A + \rho_B}{2}. \tag{4.6}$$

The Hall coefficient can be calculated in a similar way to obtain an average value, R_{Hav}. The Hall mobility is then given by

$$\mu_H = \frac{|R_{Hav}|}{\rho_{av}}. \tag{4.7}$$

All measurements of the electronic transport properties of a material require adequate preparation that satisfies the requirements of the technique to be used, for example the van der Pauw geometry. The subsequent sections give details of how the samples were prepared and how the HMS was fully utilised to perform measurements which revealed the charge transport mechanism in printed nanoparticulate silicon networks.

4.6.1 Test structure designs

The test structure design for two terminal *VI* measurements was as shown in Fig. 4.10. It consisted of an inner electrode, (a) and a concentric outer electrode, (b), bridged by a layer of printed nanoparticulate silicon, (c). The outer electrode was broken as shown in (b) and both electrodes were extended to form pads to facilitate soldering to a measurement circuit.

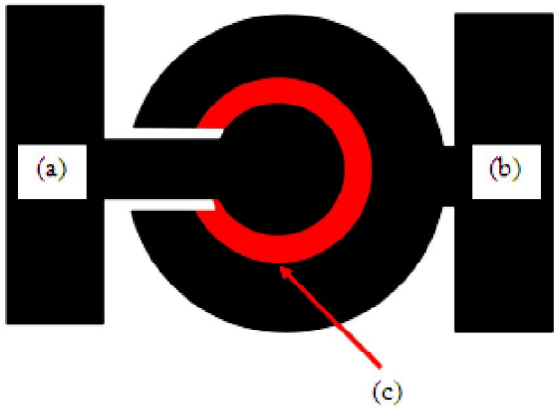

Fig. 4.10: The cup and ball design used for variable temperature *IV* measurement.

The gap between the contacts was 200 µm to ensure a reasonably low resistance for reliable measurements. For Hall effect measurements, a van der Pauw structure shown in Fig. 4.11 was used. This allowed for four point resistivity and Hall effect measurements to determine transport parameters. The van der Pauw structure consisted of printed silver bottom contacts which were 200 µm apart overlaid by a printed silicon layer in the form of a disc with a diameter of 200 µm.

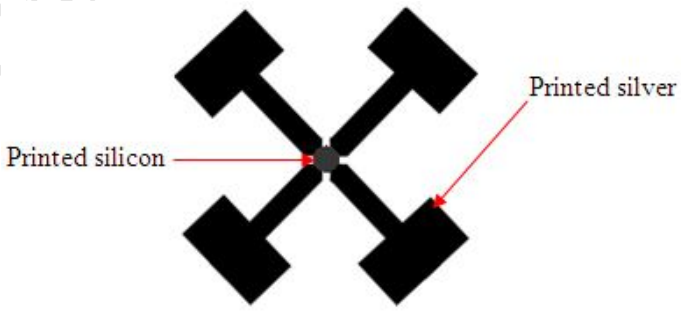

Fig. 4.11: The van der Pauw test structure.

The locus of the circumference of the silicon layer on the *V*-shaped silver contact tips described arc lengths which were approximately 90 µm, hence satisfying the van der Pauw requirement of 0.1 for the ratio of contact size relative to the dimensions of the material to be

measured, for high accuracy of measurement. In the final fully printed structures, the silver forms the bottom layer while silicon is the top layer.

4.6.2 Sample preparation for electrical measurements

Individual test structures were cut out from the A4 sheets of printed samples. Silver wire was then soldered onto the printed silver contacts. The silver wire was the means through which the test devices were connected to the variable temperature sample card of the HMS. This was followed by baking the devices in an oven at 80 ^{o}C to drive out moisture. The devices were then laminated between 25 µm thick polyethylene terephthalate (PET) films while warm to exclude moisture.

4.7 Variable temperature *IV* measurements

The model 75014 closed cycle refrigerator sample module (CCRSM) used in this work provides a variable temperature environment cooling with helium heat exchange gas. The sample is mounted on to a sample card which is situated at the lower end of the sample insert shown in Fig. 4.12.

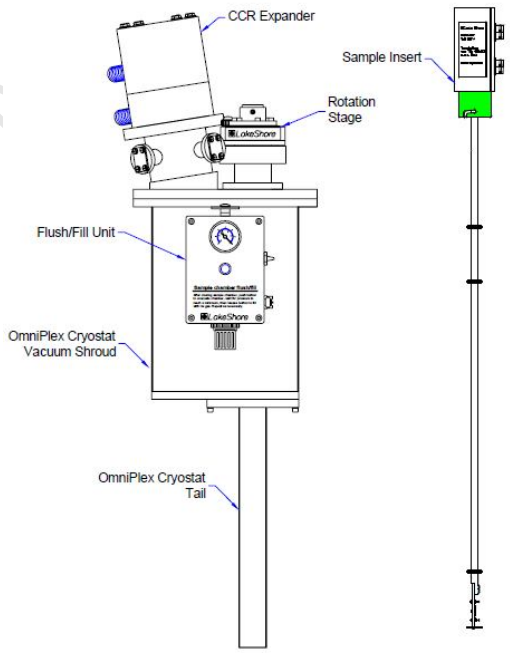

Fig. 4.12: Model 75014 CCRSM [7].

When the sample is inserted into the cryostat, it is positioned at the bottom of the cryostat tail where it is surrounded by helium gas at just above atmospheric pressure. Prior to the variable temperature measurements, the vacuum jacket of the cryostat was pumped down to 10^{-6} mbar before cooling down the cryostat.

The electrodes of the test devices were soldered to two of the sample card pins. The sample was then inserted into the sample chamber of the cryostat and the sample junction box locked in position so that the O-ring situated in the neck of the junction box sealed the mouth of the sample well, to prevent helium from leaking out of the sample chamber. The sample chamber was then purged with helium down to drive out air and hence excluding water vapour from the chamber. Using the system software, the HMS was set up to measure the *IV* characteristics of the sample by sweeping current and measuring voltage for temperatures ranging from 15 K to 345 K. A dwell time of 2 seconds was used during *IV* measurement. The IV measurements were done with the magnetic field switched off. Though the CCR can cool down to approximately 6 K, the system can measure with reliable accuracy from 15 K upwards in temperature. The maximum temperature that the system can measure is 350 K but 345 K was chosen for precautionary reasons. Ramping of temperature was performed at 1.5 K/min and a 45 minute period was allowed for settling at each preset temperature to allow temperature to equilibrate before measuring.

4.8 Variable temperature Hall effect measurements

Variable temperature Hall effect measurements are vital to the understanding of charge transport phenomena in materials. While measurements at room temperature are sufficient in many cases, transport properties can change significantly as the temperature varies. Measuring the sample material at variable temperatures allows carriers to be identified by their excitation energies and provides clues to the dominating scattering mechanism in materials.

The van der Pauw test samples were soldered on to the sample card as shown in Fig. 4.13. In this set up, four contacts (Pins 1 to 4 of the sample card) were used. The sample was then inserted into the sample chamber and the sample chamber was flushed with helium gas. The sample junction box has a rotation stage (see Fig. 4.13) which allows for variable orientation

of the sample in the magnetic field. The rotation stage was turned until the sample was oriented at 90^{o} to the magnetic field.

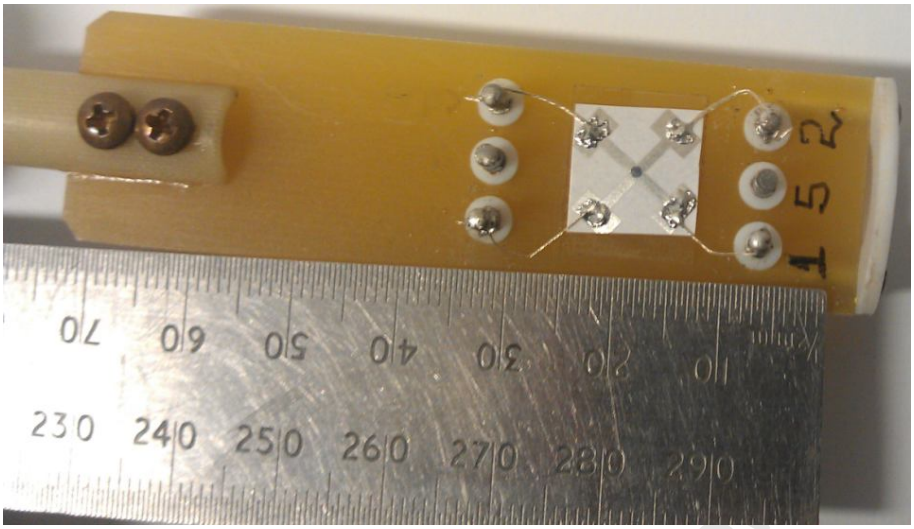

Fig. 4.13: Fully printed van der Pauw structure soldered onto a sample card.

For Hall effect measurements, like all direct measurements of electronic transport properties of a material, adequate electrical contact between the sample and measuring instrument is essential. The HMS was set up to measure *IV* characteristics to verify the ohmic behaviour at the contacts before executing variable field measurements at each temperature point. Measurement of $R_{13,13}$ and $R_{24,24}$ were used as a basic test to determine if all contacts were ohmic. In addition to *IV* measurements for contact verification, the HMS was also set up to carry out variable field measurements from 0 to 1T at temperatures from 15 K to 345 K. These measurements yielded information concerning the evolution of the mobility, carrier concentration, and resistivity of the material with temperature.

5 Results and analysis

In this chapter, the surface and internal structure of the silicon nanoparticles used in this study are presented. Analyses of the microstructure of the printed layers and data obtained from electrical and Hall effect measurements are correlated with the microstructure and preparation history of the printed silicon.

5.1 Morphology and internal structure of the silicon nanoparticles

A transmission electron microscope (TEM) micrograph of milled 2503 metallurgical grade silicon nanoparticles is shown in Fig. 5.1. As is obvious from the image, the particles form clusters which vary in size. In previous work, printed films of these particles have been probed using SAX and it was established that the primary particles are of average size of 70nm [1]. However, it is not easy to identify the primary particles in the micrograph in Fig. 5.1. It is clearly evident that the particles cluster in powder form, well before further processing routines such as ink making and printing.

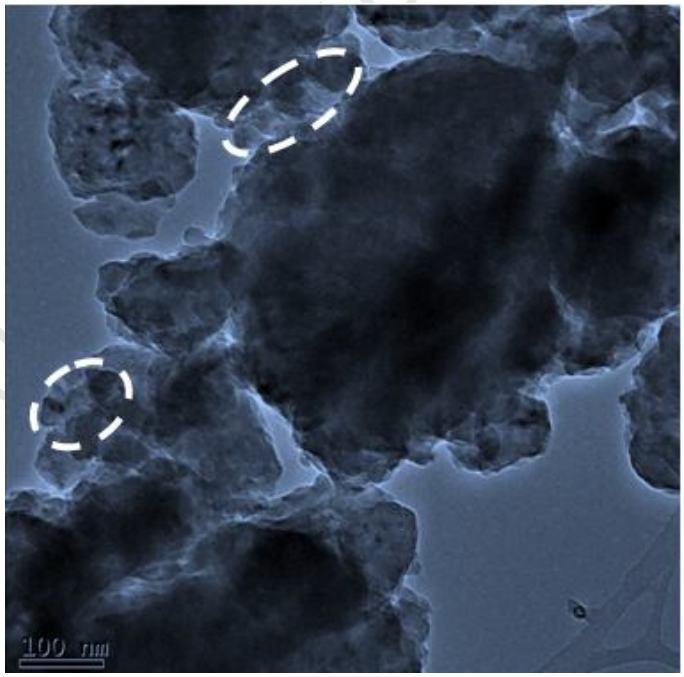

Fig. 5.1: TEM micrograph of a 5hr milled metallurgical grade silicon nanoparticle. Outlines of primary particles can be seen in delineated regions.

With a closer look at Fig. 5.1, it can be seen that there is considerable overlap between particles in a cluster so that it is difficult to ascertain the exact boundaries of the individual

particles making up the cluster. However, closer investigation of the marked regions in Fig. 5.1 shows some blurred outlines of particles or small aggregates thereof. The images of nanoparticles from milled *n*- and *p*-type wafers were similar to those in Fig. 5.1 except that these nanoparticles were of larger average size as will also be shown in the subsequent section on SEM. The milled particles are all irregularly shaped with aspect ratios in the order of $2:1$. Small particles have a lower aspect ratio, being more rounded than the large ones. In a broad sense, the particles are rough and elongated with large size dispersion. This description is in agreement with observations reported in earlier investigations on the morphology of the particles except that there was no mention of the tendency of the particles to form persistent clusters [2].

A TEM micrograph of silicon nanoparticles produced by chemical vapour synthesis (CVS) is displayed in Fig. 5.2.

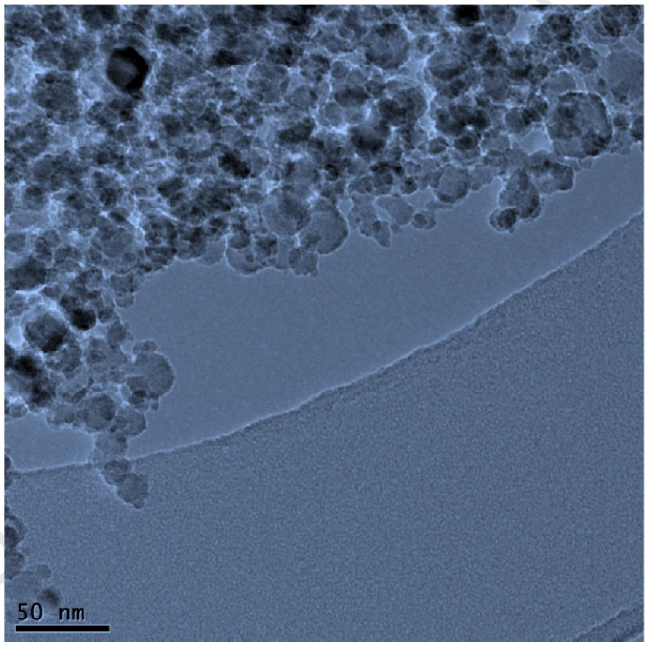

Fig. 5.2: TEM image of nanoparticles produced by CVS.

The image clearly shows that the particles are spherical and are reported by Scriba et al [3] to have an average diameter in the range of 35 nm. The primary particles are reported to be multifaceted; forming branched chains with some evidence of sintering of adjacent particles and displaying appreciable overlapping of particles [3].

Observations of lattice planes of both types of powder are shown in Fig. 5.3. The internal structure of a milled silicon nanoparticle is shown to be polycrystalline as shown in Fig. 5.3(a).

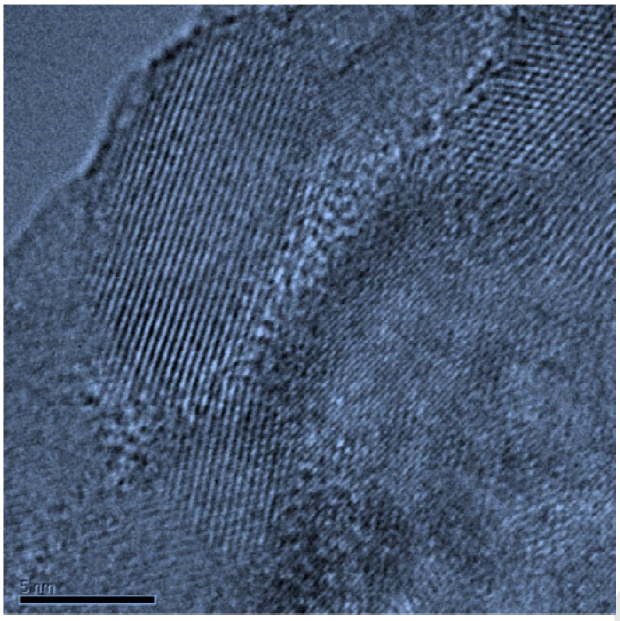

Fig. 5.3 (a): HRTEM micrograph showing the internal structure of a silicon nanoparticle produced by milling [2].

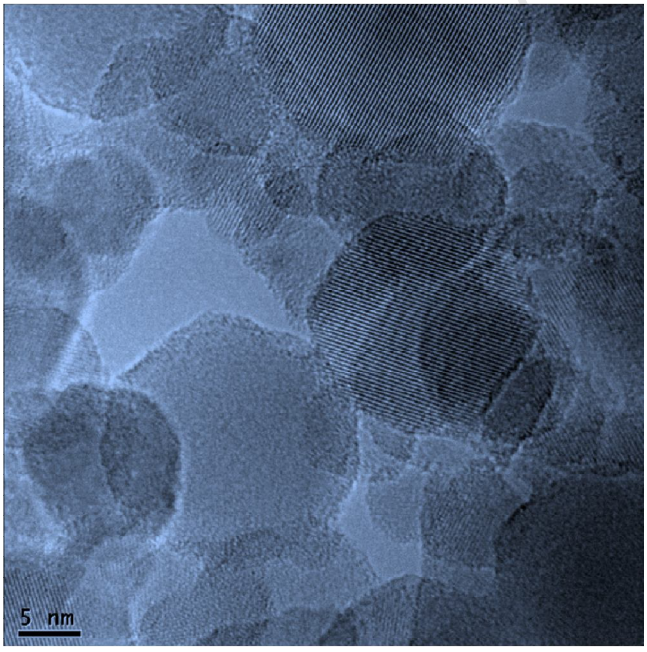

Fig. 5.3 (b): HRTEM micrograph showing the internal structure of a silicon nanoparticle produced by CVS.

Fig. 5.3 (b) shows that a large proportion of the nanoparticles produced by CVS are mono-crystalline. The absence of diffraction lines on some parts of the micrographs may be

attributed to particles that do not satisfy diffraction conditions and hence they show no lattice planes.

The electron diffraction pattern for milled *p*-type powder is shown in Fig. 5.4. The differently rotated single crystalline diffraction patterns, overlaying weak continuous rings were similar in all milled powders. The width of the rings is similar to the size of the spots, which is an indication that there is little amorphous fraction in the samples. For milled particles, it is possible that only a few particles could be illuminated, hence the observed superimposed diffraction patterns and the rings suggest that these particles are polycrystalline.

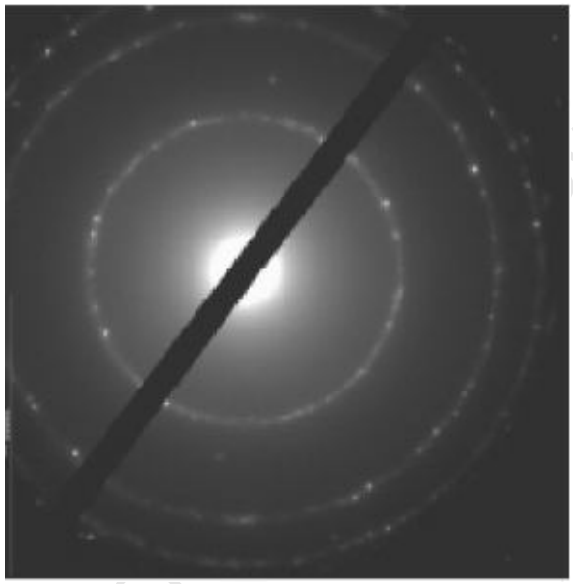

Fig. 5.4: Electron diffraction pattern for milled *p*-type silicon.

No conclusive electron diffraction pattern analysis could be assigned to the particles produced by CVS owing to the large number of small particles illuminated by the electron beam.

5.2 Size distribution of nanoparticles produced by milling

Images obtained using scanning electron microscopy (SEM) on metallurgical grade silicon pellets are shown in Fig. 5.5. The shape and size of the particles is the same as that observed under TEM. Clusters of silicon nanoparticles are clearly evident in the SEM picture.

The size distribution of particles produced by milling is shown in Fig. 5.6. The description of the size distributions were based on the log-normal distribution fitted to histograms

constructed from line scans of the grey scale intensity in the SEM micrographs obtained for pellets. The descriptive statistics of the size distributions were as shown in TABLE I.

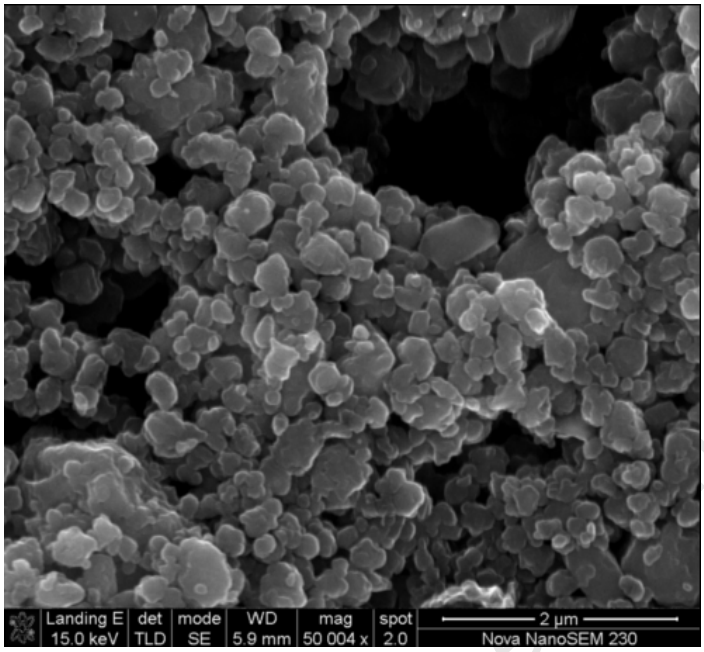

Fig. 5.5: SEM image of a compressed pellet of nanoparticles milled from 2503 grade silicon.

Silicon nanoparticles milled from 2503 grade silicon have a smaller average size and are less polydisperse than nanoparticles produced by milling *n*- and *p*-Si wafers.

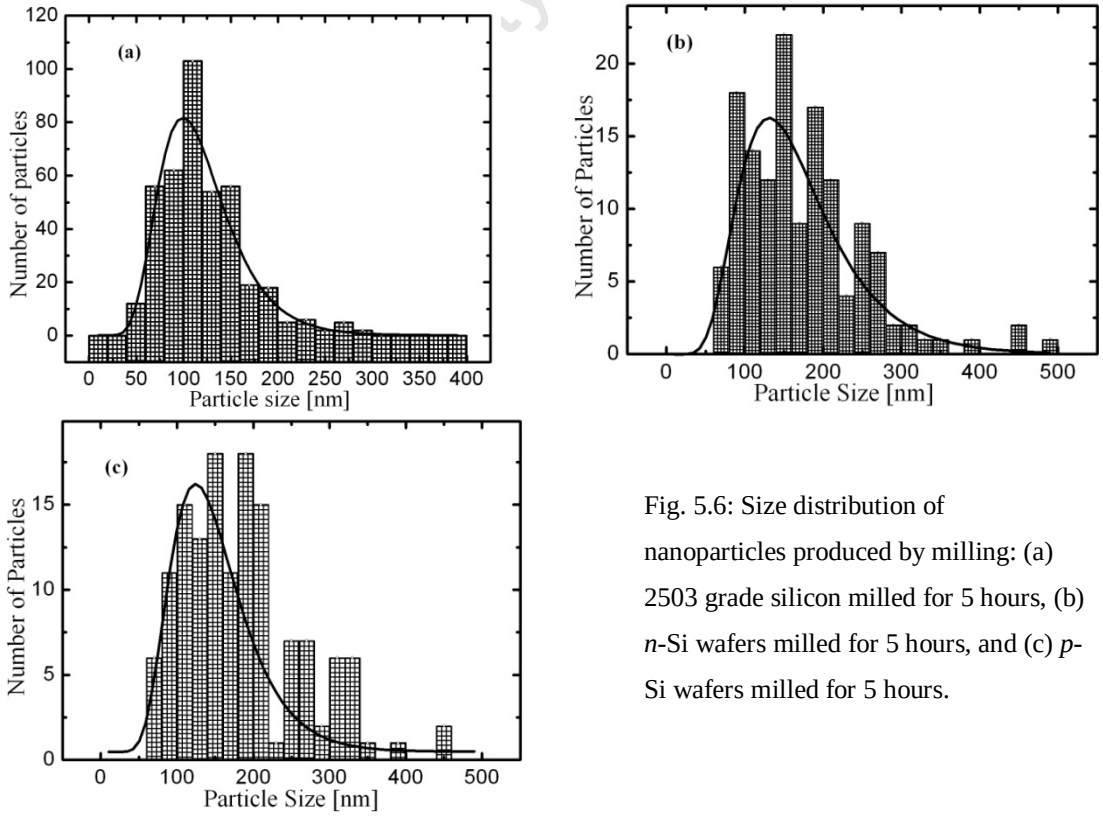

Fig. 5.6: Size distribution of nanoparticles produced by milling: (a) 2503 grade silicon milled for 5 hours, (b) *n*-Si wafers milled for 5 hours, and (c) *p*-Si wafers milled for 5 hours.

TABLE I: Size distribution of nanoparticles produced by milling different types of bulk silicon.

Type of silicon nanoparticles	Median (nm)	Standard deviation
2503	112.1 ± 2.7	0.347 ± 0.012
p	140.8 ± 6.0	0.355 ± 0.041
n	155.9 ± 7.3	0.415 ± 0.043

Despite differences in their size distribution, nanoparticles produced by milling are similar in their shape and surface characteristics.

5.3 Curing of printed layers

The curing time for printed silicon was established indirectly by the mass loss experiment described in chapter 4. The change in mass of binder with time, t, was as shown in Fig. 5.7.

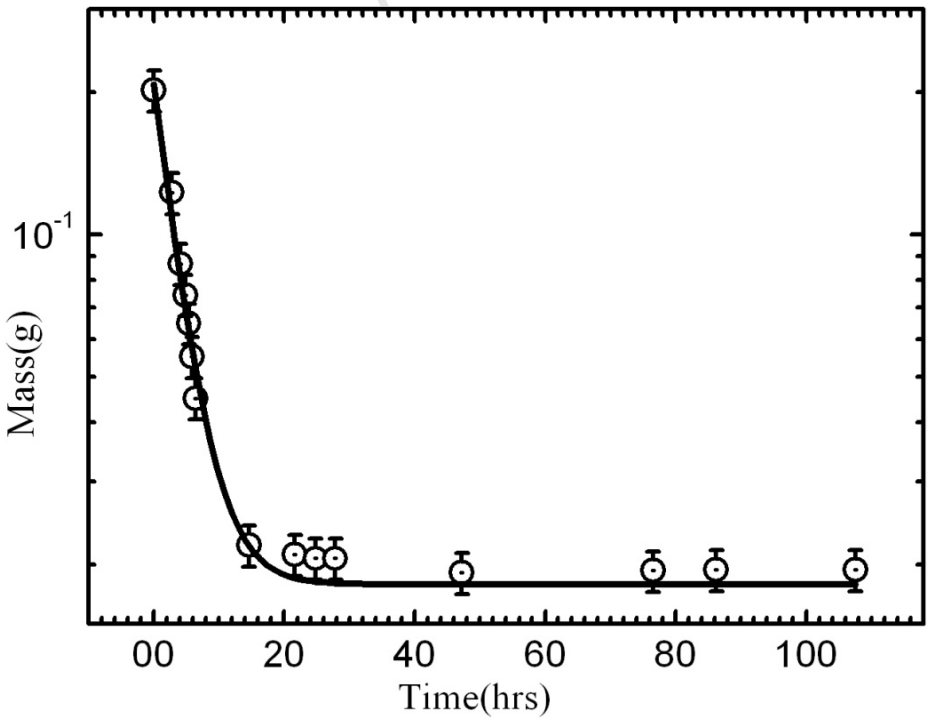

Fig. 5.7: Change in mass during drying of the binder

The drying profile for the binder can be described by the function

$$m = m_0 \exp\left(\frac{-t}{\tau}\right) + m_f , \qquad (5.1)$$

where m_0 is the initial mass of the binder, which after drying leaves a residual mass, m_f, and τ is the drying time constant. For the 10 samples of binder measured, the average residual mass as a proportion of the initial binder weight was $(8.7 \pm 1.8)\%$ with a drying time constant of (3.7 ± 0.2) hours.

The residual proportion of the binder can be used to estimate the thickness of a possible layer of insulating binder material covering the particles. For a spherical primary nanoparticle of radius r, covered in a shell of insulating binder material of thickness d, and a density of silicon about twice that of the acrylic binder; for a mass of silicon m_s, with density ρ_s and a mass of binder m_b of density ρ_b,

$$\frac{\rho_b}{\rho_s} = \frac{1}{2} = \frac{m_b}{m_s}\frac{V_s}{V_b} , \qquad (5.2)$$

where V_s and V_b are the volumes of silicon and binder respectively. For a silicon ink of 80% particle concentration, the ink contains 20% by mass of binder material which after curing reduces to a residue of about 8.7%. Thus

$$\frac{V_b}{V_s} = 0.0435. \qquad (5.3)$$

Alternatively,

$$\frac{V_b}{V_s} = \frac{4\pi(r+d)^2 d}{\frac{4}{3}\pi r^3}, \text{ but } r >> d, \text{ and so}$$

$$\frac{3r^2 d}{r^3} = 0.0435,$$

giving $$d = \frac{0.0435r}{3}. \qquad (5.4)$$

The size of primary particles used in this study has been determined by SAXS measurements to be 80nm [1]. Thus

$$d = \frac{0.0435 \times (40\ \text{nm})}{3} \quad \approx \quad 0.58\ \text{nm} \ .$$

The predicted thickness of approximately 5.8 angstroms simply shows that there cannot be complete coverage of the nanoparticles in the printed layer. The coverage of particles by the binder cannot be expected to be uniform owing to the small proportion of the binder and the large binder molecules which tend to accumulate giving rise to the partial coverage.

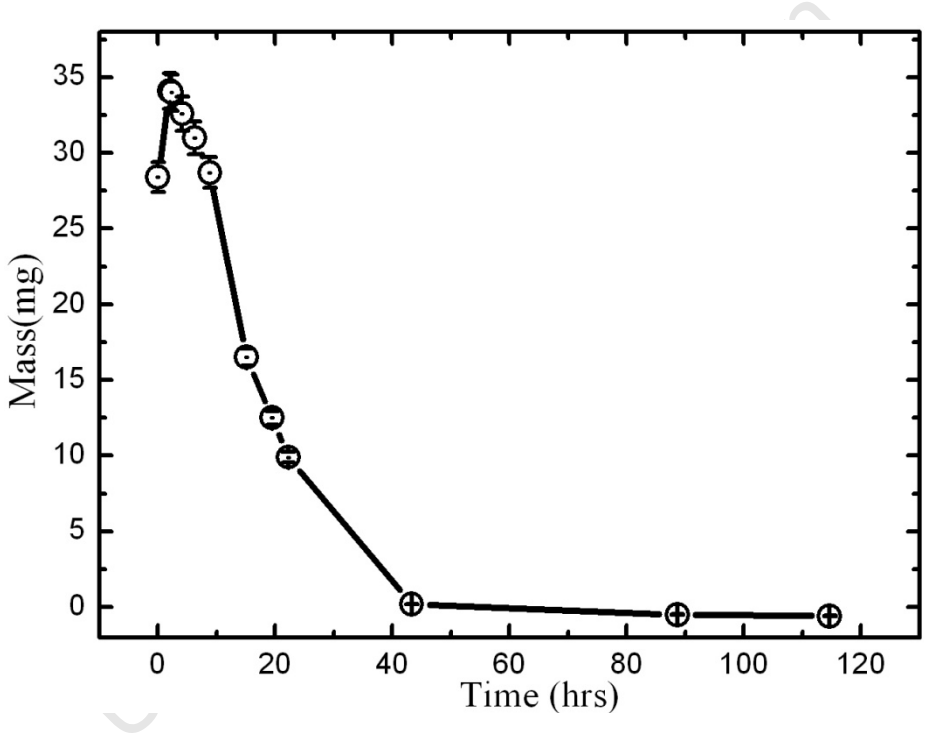

Fig. 5.8: Change in mass during drying of propylene glycol.

Glycol, which was used as a dilutant in the ink, first increased in mass at the beginning of the experiment and then evaporated leaving no residue. The initial increase in mass during the first two hours can be attributed to the absorption of water from air by the glycol. No obvious phenomenological equation could be fitted to the full drying profile shown in Fig. 5.8. However it can be said that all the glycol evaporated after 40 hours. This drying time is about twice as long as that of the binder. This is plausible since the glycol is meant to retard drying of the binder; hence its drying time is expected to be longer.

The drying characteristics of printed silver were investigated by tracking the change in resistance of the printed layers over time. The input of Girma Goro Gonfa [4] is duly acknowledged in this respect. In Gonfa's investigations, it was established that the silver (Dupont Luxprint 5000 conductor) printed on paper takes 20 hours to fully cure under ambient conditions. The curing is limited by two major processes: polymerisation of the binder, and evaporation of the solvent [4].

When fully dry, both printed silicon and silver layers were dry to the touch. Some of the samples printed from high particle concentration silicon inks, such as 88%, could be easily rubbed off using a finger, whereas those of low particle loading were robust and more mechanically stable.

5.4 Morphology of printed layers

Fig. 5.9 shows optical micrographs of silver-paper, silicon-paper and silver-silicon boundaries viewed from the top of the printed layers.

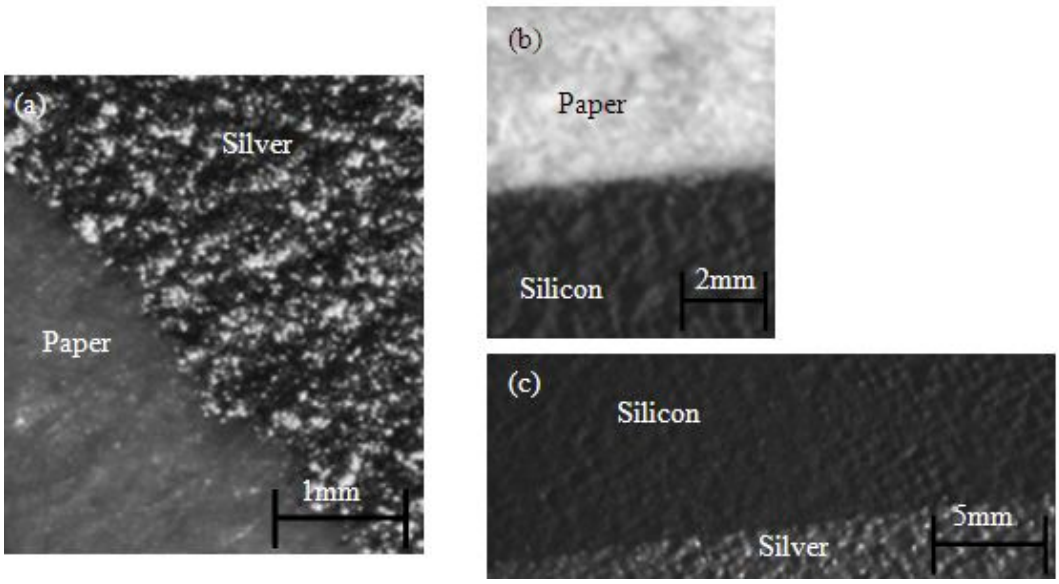

Fig. 5.9: Optical micrographs showing edge definition between (a) silver-paper, (b) silicon-paper, and (c) silver-silicon interfaces.

The edge definition of the printed layers shows tolerances within 0.1mm, which was acceptable for the purpose of this study. Printed silicon layers were generally rough with a square array quite evident on the surface, as shown in the SEM image in Fig. 5.10. This pattern is an artefact arising from the printing screen mesh.

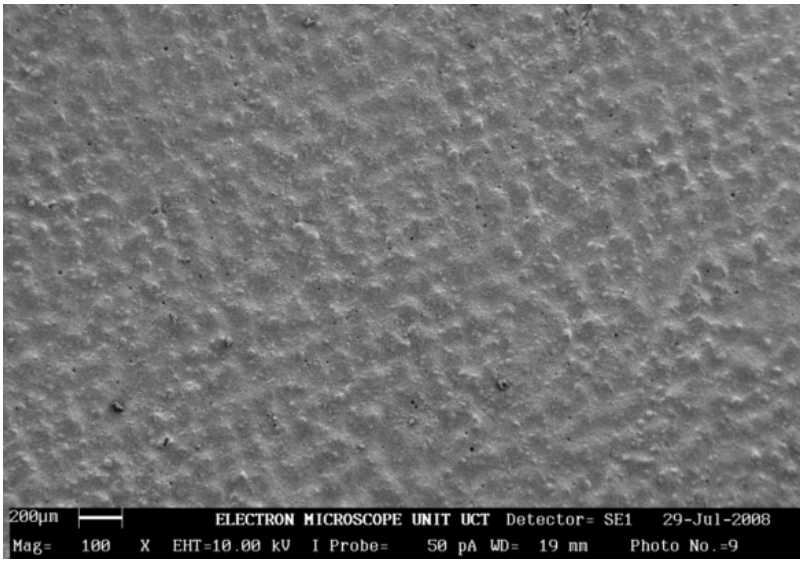

Fig. 5.10: SEM of printed silicon surface.

The mesh pattern was not as obvious for printed silver layers. This difference might be a result of different rheologies of the two inks; the silver ink having a relaxation time which is long enough to level out the pattern of the screen. Pinholes were a common feature in printed silicon layers compared to silver layers, possibly for the same reason. After calendaring a silicon layer such as the one shown in Fig. 5.10, the mesh pattern is levelled out and the layer becomes less rough as shown in Fig. 5.11.

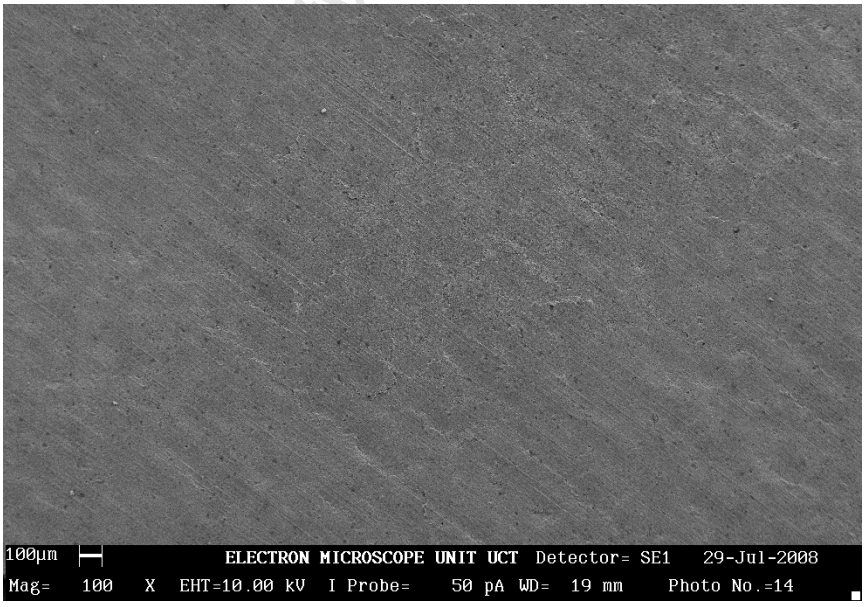

Fig. 5.11: Calendared silicon layer.

3D plots showing the surface topology of calendared and uncalendared silicon layers, as seen using an optical profiler, are shown in Fig. 5.12. It is worth noting the reduced prevalence of pinholes in the calendared silicon layer compared to the original layer.

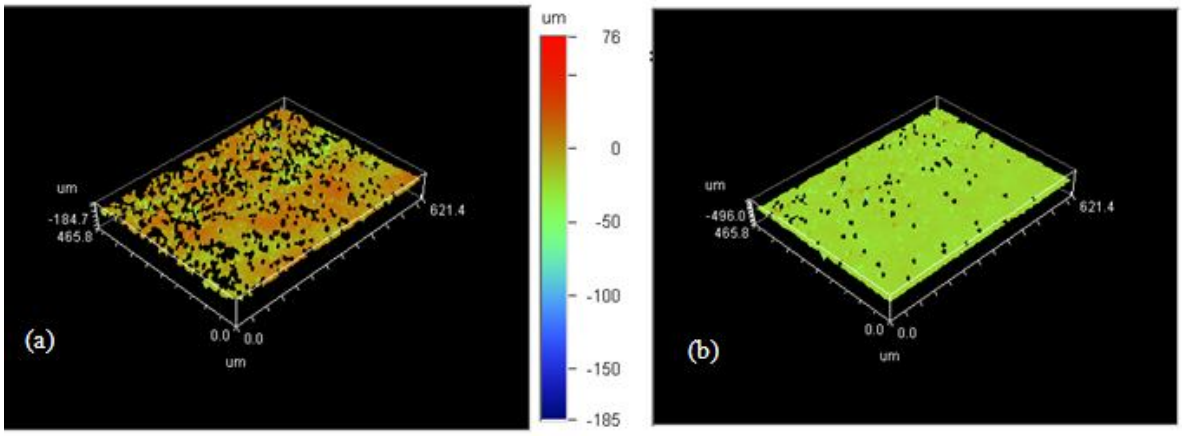

Fig. 5.12: Occurrence of pinholes in (a) calendared and (b) uncalendared 2503 metallurgical silicon layers.

The calendared layers show an average thickness of about $10\,\mu m$ with peaks reaching up to $15\,\mu m$, whereas uncompressed layers had an average thickness of $30\,\mu m$.

A higher magnification SEM image for a silicon layer printed from a metallurgical grade silicon ink of 80% particle loading is shown in Fig. 5.13. The layer was coated with gold palladium, which can be seen in the micrograph as a film covering the particles and should not be misinterpreted as a binder. The image shows clustering of nanoparticles which also aggregate to form a self similar web of clusters that constitutes an unbroken semiconducting backbone.

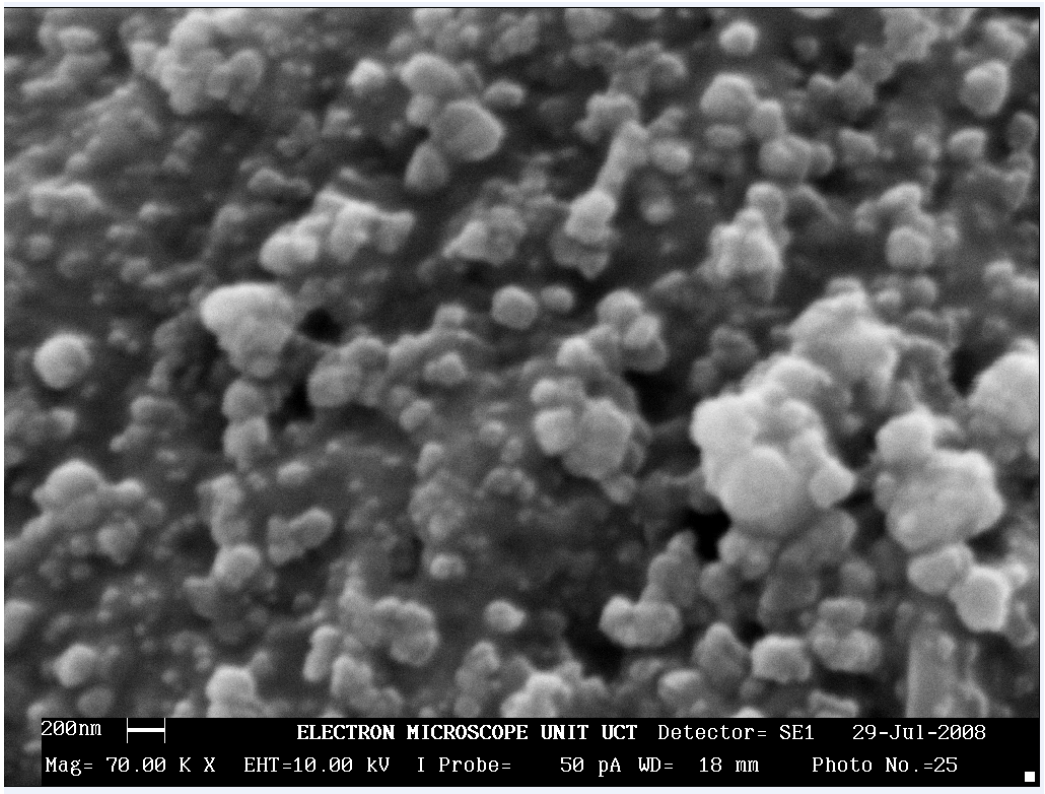

Fig. 5.13: Secondary electron SEM images of printed nanoparticulate metallurgical grade silicon layer.

Similar features were seen for printed layers made from the other silicon nanoparticles, except for the variations in the size of the nanoparticles. The structure can result in a network of connected particles which results in a multitude of charge transport paths.

Surface observation alone could not provide information concerning the internal structure of the printed layers [5, 6]. A cross-sectional SEM image of a metallurgical grade sample of 80% particle concentration prepared by microtoming is shown in Fig. 5.14. In (a), the sample embedded in the resin is clearly seen as a thin strip extending from left to right in the centre of the image. The higher resolution image of a section of the sample is shown in (b). The different layers of the composite structure are labelled. Due to the tearing forces involved during microtoming, some features of the sample were damaged. The paper ripped apart as shown in the image. The resin probably dissolved the silicon layer causing it to split. However, for the section where the paper substrate is not damaged, there is no delamination of the printed silver from the paper substrate.

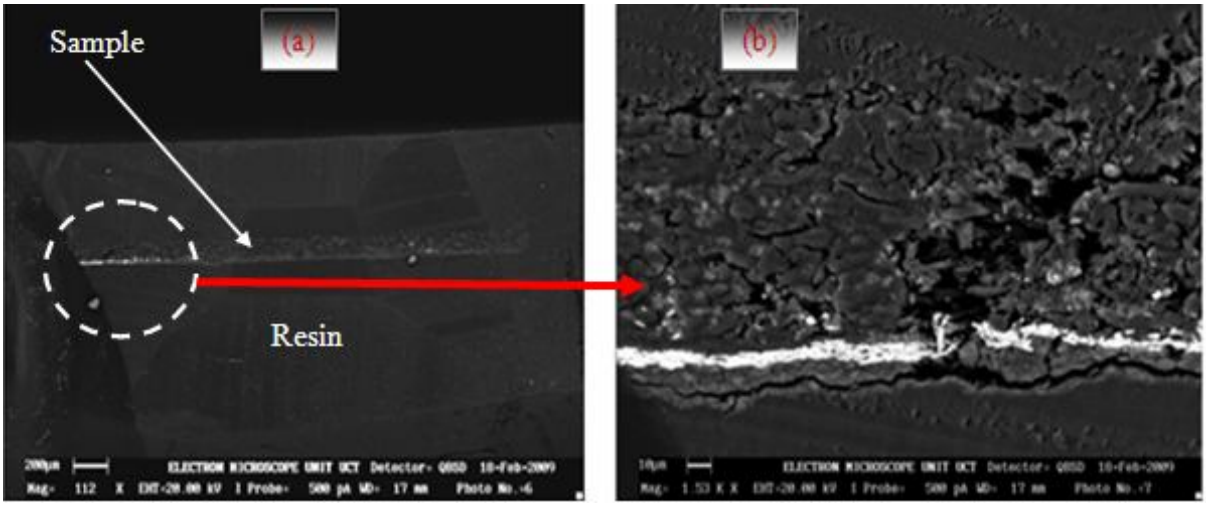

Fig. 5.14: QBSD cross-sectional view of a sample prepared by microtoming.

Fig. 5.15 shows another cross-sectional SEM image of a layer of silicon printed on paper prepared by simply cutting the sample and analysing without casting it into a resin.

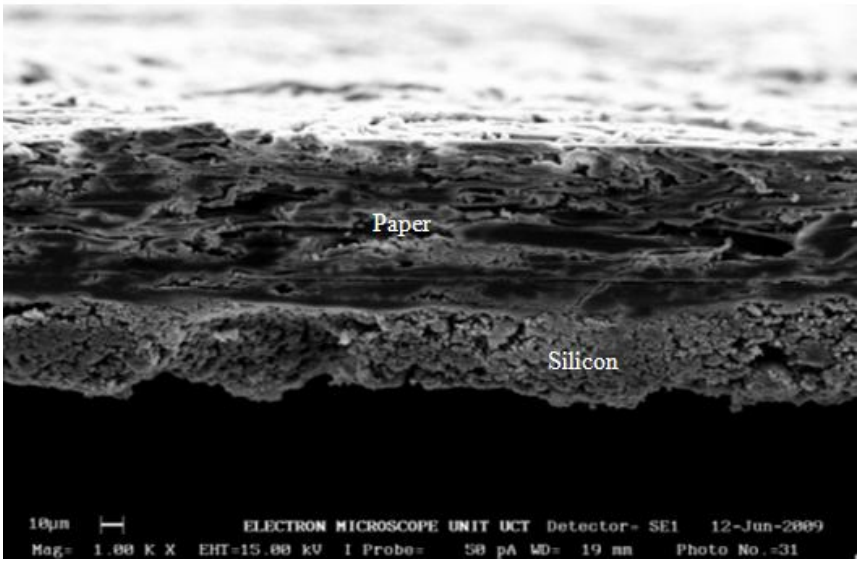

Fig. 5.15: Cross-sectional SEM micrograph of an uncalendared layer of silicon printed on paper. The sample was not embedded in a resin.

The thickness of the printed silicon layer before calendaring was seen to be of the order of $35 \pm 15\,\mu m$ in agreement with profileometry. The printed layer is highly porous and rough mainly as a result of the screen mesh structure; hence the layers were calendared before further electrical measurements. After calendaring, the thicknesses of the printed layers were in the order of $15 \pm 5\,\mu m$.

5.5 Electrical characterisation

5.5.1 *IV* measurements

As described in chapter 4, the test structures used for IV measurements are composed of printed silicon which bridges the gap between printed silver contacts. A typical *IV* characteristic is shown in Fig. 5.16. At low voltage, there is only a small current, implying that the sample is highly resistive. At high voltage, the current increases non-linearly. The shape of the *IV* curve indicates a symmetric diode configuration typical of a varistor. This shape is preserved for all temperatures, except that the curvature becomes stronger as the temperature decreases. In addition, the *IV* curves have a finite slope for all temperatures, which means that the material always has a finite conductance at all temperatures. The insert shows the same data plotted on a semi-log plot showing that the non-linear current-voltage characteristics do not have a power law dependence which would indicate space charge limited conduction, but are due to the presence of diode junctions

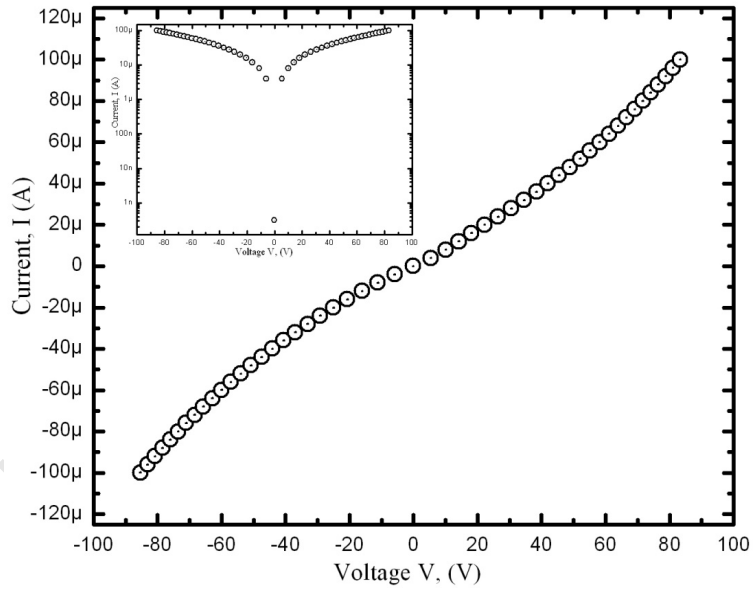

Fig. 5.16: Typical *IV* curve for a cup and ball test structure at 300 K. The inset shows the same data in a semi-logarithmic representation.

The presence of symmetry in the *IV* curve is not surprising as the test structure is symmetric at both the macroscopic and the microscopic level. At the macroscopic level, the silver contacts which are printed from the same silver ink form the bottom contacts to a printed silicon layer. At microscopic level, the printed silicon is composed of nanoparticles which form a network of conducting paths. Symmetry is also expected at the interface between adjacent particles since the particles consist of the same material. The printed test structure is

therefore characterised by numerous interfaces [7-8]. However, neither the silver-silicon interfaces nor the particle-particle junctions alone may be said to solely limit the shape of the *IV* curve. The shape is expected to be associated with the overall effect of these interfaces. However the metal-metal junction formed at the soldered joint between the silver lead and the printed silver is expected to insignificantly influence charge transport. Based on symmetry considerations in the microstructure of the printed layers, the *IV* characteristic can be said to resemble two diodes connected back to back, as can be represented by the equivalent circuit shown in Fig. 5.17.

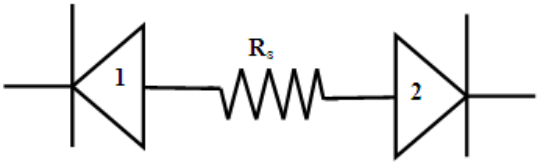

Fig. 5.17: Equivalent circuit for the printed test structure.

The diodes, 1 and 2, are drawn in lieu of the effective junction imparting symmetry to the IV curve, and R_s is the lumped series resistance of the sample and measurement system. The series resistance arises from interconnections between junctions, leads connecting the sample to the measurement instruments, the internal structure of the interfaces, and the bulk resistance of particles. In the equivalent circuit shown in Fig. 5.17, one of the two diodes will always be reverse biased irrespective of the direction of current. This would normally mean that only the saturation current would pass through the equivalent circuit. The *IV* curve shown in Fig. 5.16 shows that current continually increases and does not saturate. The reverse biased diode must therefore be in breakdown condition to obtain the characteristics observed in Fig. 5.16. In fact, this is the case as it shall be shown that the applied voltage of approximately 50 V exceeds the activation energy for conduction which shall be shown to be approximately 0.2 eV. When one of the diodes in Fig. 5.17 is in breakdown, the equivalent circuit reduces to that shown in Fig. 5.18.

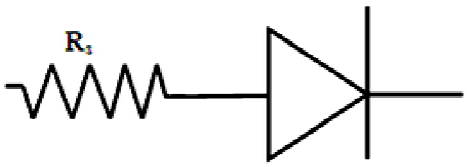

Fig. 5.18: Equivalent circuit of the nanoparticle system under high voltage.

An alternative equivalent circuit to the one shown in Fig. 5.17 consists of two diodes connected in anti-parallel in series with a resistance as shown in Fig. 5.19

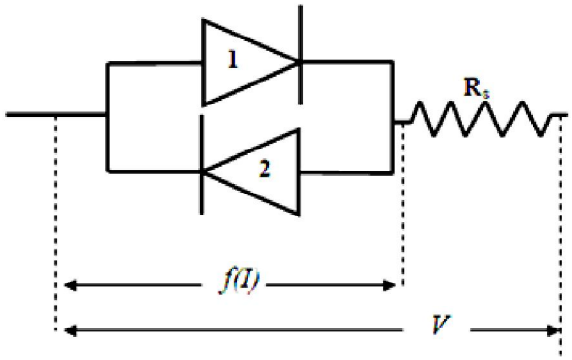

Fig. 5.19: Alternative equivalent circuit for the nanoparticle network.

If there is a current from left to right through the circuit shown in Fig. 5.19, diode 1 will be forward biased. The reverse is true if the current is in the opposite direction. For either direction of current, the equivalent circuit reduces to that shown in Fig. 5.18. Thus the circuits shown in Fig. 5.17 and Fig. 5.19 are equivalent under the operating conditions. Assuming the standard equation for a real diode, the current, I_D, through a diode under applied voltage, V, at temperature, T is given by

$$I_D = I_0\left[\exp\left(\frac{eV_D}{\eta k_B T}\right)-1\right], \tag{5.5}$$

where e is the electronic charge, η is the diode ideality factor, k_B is the Boltzmann constant, V_D is the voltage drop across the diode and I_0 is the diode reverse saturation current. If the *IV* curve of diode 1 in Fig. 5.19 can be described by equation (5.5), then the current, I_1, due to diode 1 is given by

$$I_1 = I_0\left[\exp\left(\frac{e(V-IR_s)}{\eta k_B T}\right)-1\right] \quad , \tag{5.6}$$

and I_2 through diode 2 is given by

$$I_2 = -I_0\left[\exp\left(\frac{-e(V-IR_s)}{\eta k_B T}\right)-1\right], \tag{5.7}$$

where it is assumed that η is the same for both diodes since the charge flows through the same material, and from symmetry considerations the magnitude of the saturation current and ideality factor should be the same for the two diodes. The net current, I, through the sample is then given by

$$I = I_1 + I_2$$

$$I = I_0\left[\exp\left(\frac{e(V - IR_s)}{\eta k_B T}\right) - \exp\left(\frac{-e(V - IR_s)}{\eta k_B T}\right)\right]. \tag{5.8}$$

Rearranging equation (5.8) to express V explicitly in terms of I yields

$$V = \frac{\eta k_B T}{e}\ln\left|\frac{1}{2}\left\{\left(\frac{I}{I_0}\right) + \sqrt{\left(\frac{I}{I_0}\right)^2 + 4}\right\}\right| + IR_s \ . \tag{5.9}$$

Equation (5.9) was fitted to *VI* curves at each temperature point to extract η , R_s and I_0. Fitting was performed using Origin software, employing a least-linear squares fitting routine with statistical weighting of the residuals and a Levenberg-Marquardt algorithm. Equation (5.9) produced excellent fits to the *VI* curves, except for those measured at temperatures below 50 K. The inconsistency in fitting *IV* curves at a low temperature of 15 K is illustrated in Fig. 5.20 (a).

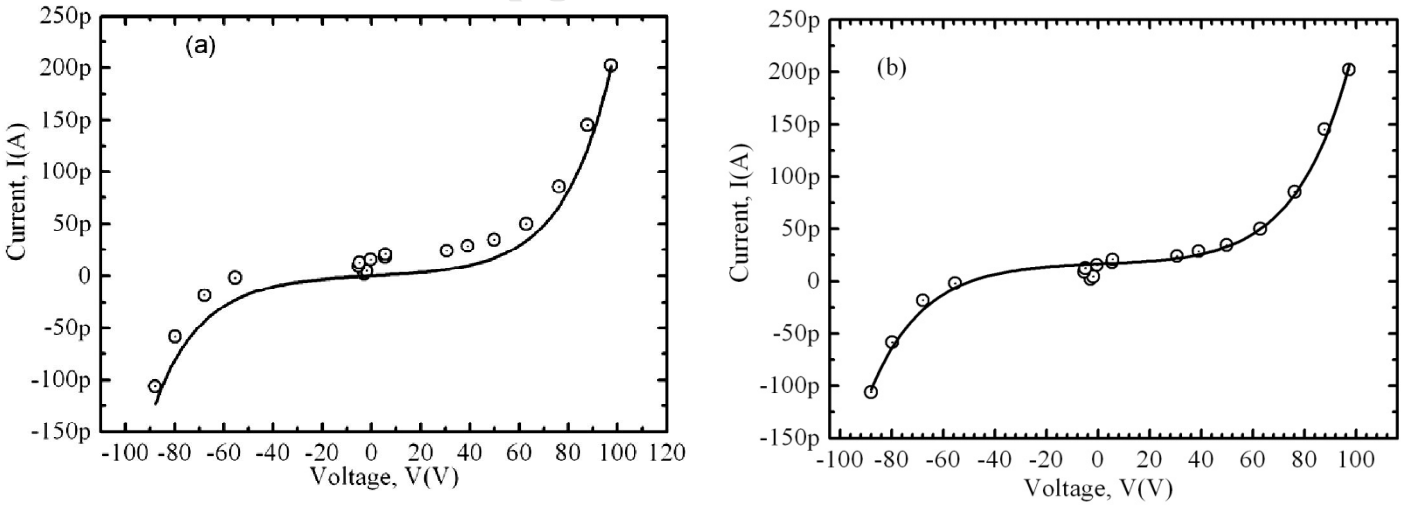

Fig. 5.20: Quality of fits for low temperature *IV* curves; (a) fitted with no consideration of parallel conductance, and (b) fit includes parallel conductance.

However, the fits to low temperature *IV* curves were improved by modifying equation (5.9) to include a parallel resistance R_p. By reconsidering the circuit shown in Fig. 5.19, the voltage applied across the circuit can be expressed as

$$V = f(I) + IR_s \ , \tag{5.10}$$

where $f(I)$ is the voltage-current characteristic of the diodes given by equation (5.9). The effective resistance of the circuit, R_{eff}, is given by

$$R_{eff} = \frac{V}{I} = \frac{f(I)}{I} + R_s \, . \tag{5.11}$$

If R' is the effective resistance incorporating the parallel resistance, then the circuit in Fig. 5.19 modifies to that shown in Fig. 5.21.

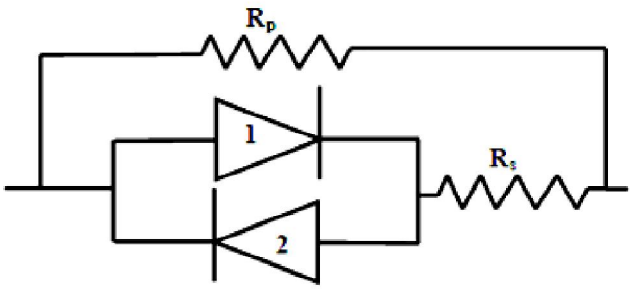

Fig. 5.21: Improved circuit model of the printed test structure showing the parallel resistance which manifests at low temperature.

The new effective resistance can be expressed as

$$\frac{1}{R'} = \frac{1}{R_p} + \frac{1}{R_{eff}} \ ,$$

giving $$R' = \frac{R_p R_{eff}}{R_{eff} + R_p} \, ,$$

and hence $$R' = \frac{R_p\left(\frac{f(I)}{I} + R_s\right)}{\frac{f(I)}{I} + R_s + R_p} \quad . \tag{5.12}$$

Expressing the applied voltage, V in terms of the effective resistance yields

$$V = IR' = \frac{R_p I\left(f(I) + IR_s\right)}{f(I) + IR_s + IR_p}. \qquad (5.13)$$

Equation (5.13) was fitted to the *VI* data for temperatures ranging from 15 to 50 K. The best fits were obtained by fitting *I* as a function of *V* with $R_s = 0$ using equation (5.8) as shown in Fig. 5.20 (b). The parallel conductance varied from 10^{-13} to 10^{-11}S depending on the nature of the devices and can be attributed to parasitic conductance through the substrate and/or sample card and leakage to ground through leads connecting the sample to the measurement set up. The series resistance values were significantly lower implying that, at these temperatures, most of the voltage drop is across the diode junctions. Fitting equation (5.13) to higher temperature *VI* curves yielded values of R_p which were insignificant compared to the other resistances. Moreover the fits were characterised by unreasonably large errors. Thus for temperatures greater than 50K, voltage was fitted as a function of current, neglecting the presence of R_p as shown in Fig. 5.22.

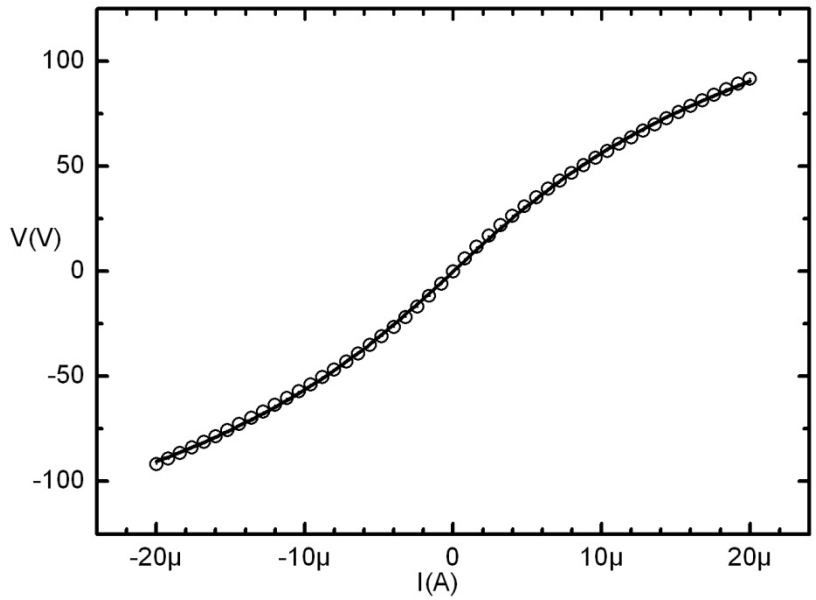

Fig. 5.22: Fitted *VI* characteristic of a metallurgical grade silicon sample.

Metallurgical grade silicon devices were expected to show the least conductivity since they were not highly doped. Nanoparticles produced by hot wire synthesis were highly doped *p*-type silicon; hence they were anticipated to show the highest conductance. It should be straight forward to understand that the conductivities of the printed silicon layers correlate with the preparation history of the nanoparticles and device fabrication. Control of the deposition of the functional material onto the substrate, uniformity of the printed films and

adhesion between printed layers dictate the overall conductance features of the printed devices.

The evolution of the *IV* curves with temperature is demonstrated in Fig. 5.23. Symmetry of the *IV* curves is preserved over the extended temperature range from 15-345 K, but the resistance, seen by the slope of the curve, decreases with temperature.

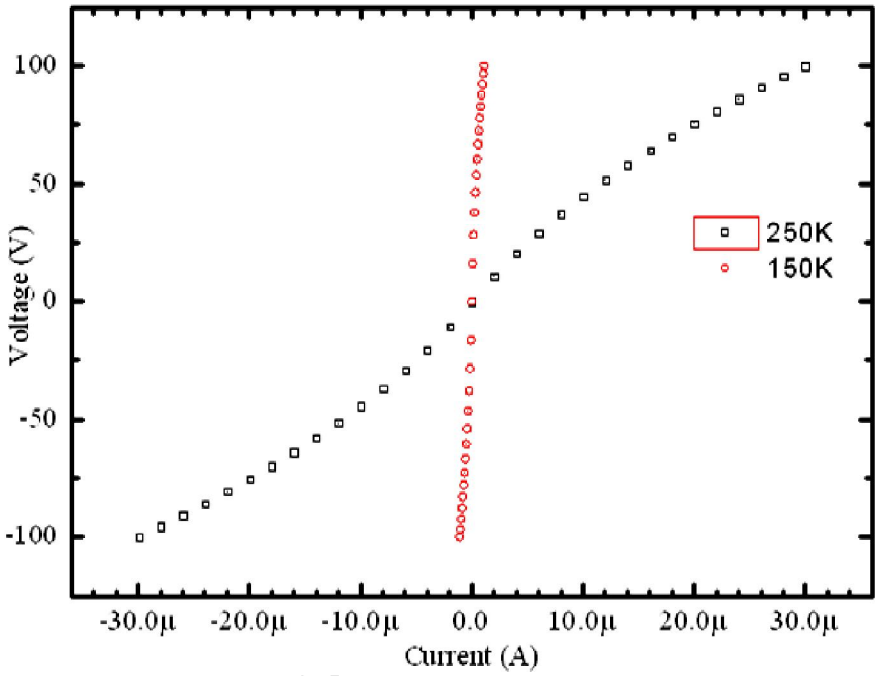

Fig. 5.23: *IV* curves at different temperatures of a typical test structure at 150 K and 250 K.

A plot of differential resistance determined from the slopes of *VI* curves obtained over the extended temperature range for a printed metallurgical grade silicon device is shown in Fig. 5.24. It is obvious from the graph that for a constant voltage, the differential resistance, dV/dI decreases with temperature. This is strong evidence that charge transport is thermally activated. For high temperatures, the differential resistance shows significantly weak curvature and the slopes of the curves decrease at higher absolute potentials as temperature increases.

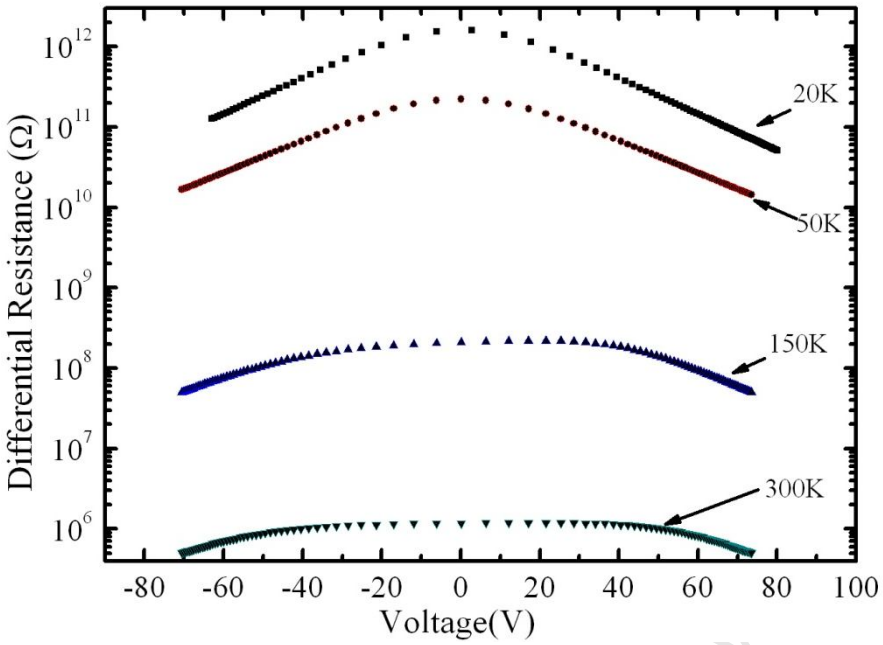

Fig. 5.24: Differential resistance curves for a metallurgical grade silicon test structure taken over an extended temperature range of 15-345 K.

Thus, at high temperatures the differential resistance is less sensitive to applied voltage. At low temperature, in addition to temperature sensitivity being significant, the differential resistance shows stronger dependence on applied voltage. Thus, in addition to thermal activation, the conductance of the nanoparticle system is also susceptible to electric field activation.

From equation (5.8), an analytical equation for the differential current of the nanoparticle system can be derived as

$$dI = \frac{I_0 e}{\eta k_B T}\exp\left(\frac{e(V - IR_s)}{\eta k_B T}\right)dV - \frac{I_0 e R_s}{\eta k_B T}\exp\left(\frac{e(V - IR_s)}{\eta k_B T}\right)dI$$
$$-\left[\frac{-I_0 e}{\eta k_B T}\exp\left(\frac{-e(V - IR_s)}{\eta k_B T}\right)dV + \frac{I_0 e R_s}{\eta k_B T}\exp\left(\frac{-e(V - IR_s)}{\eta k_B T}\right)dI\right] \quad ,$$

and

$$dI = \frac{I_0 e}{\eta k_B T}\left[\exp\left(\frac{e(V - IR_s)}{\eta k_B T}\right) + \exp\left(\frac{-e(V - IR_s)}{\eta k_B T}\right)\right]dV$$
$$-\left[\frac{I_0 e R_s}{\eta k_B T}\left\{\exp\left(\frac{e(V - IR_s)}{\eta k_B T}\right) + \exp\left(\frac{-e(V - IR_s)}{\eta k_B T}\right)\right\}dI\right] \quad .$$

Hence the differential conductance is

$$\frac{dI}{dV} = \frac{\dfrac{I_0 e}{\eta k_B T}\left[\exp\left(\dfrac{e(V - IR_s)}{\eta k_B T}\right) + \exp\left(\dfrac{-e(V - IR_s)}{\eta k_B T}\right)\right]}{1 + \dfrac{I_0 e R_s}{\eta k_B T}\left\{\exp\left(\dfrac{e(V - IR_s)}{\eta k_B T}\right) + \exp\left(\dfrac{-e(V - IR_s)}{\eta k_B T}\right)\right\}} \quad . \tag{5.14}$$

For low applied voltage and current

$$\lim_{(I,V)\to(0,0)} \frac{dI}{dV} = \frac{2I_0 e}{\eta k_B T + 2eI_0 R_s}, \tag{5.15}$$

such that for low voltage, the differential conductance, G_0 can be considered to be

$$G_0 = \frac{2I_0 e}{\eta k_B T + 2eI_0 R_s} \quad . \tag{5.16}$$

Equation (5.16) was used to calculate the low voltage differential conductance using the parameters η, R_s and I_0 for the different temperatures. Low voltage and current conditions were chosen for the determination of conductance, because under these conditions the diode will be dominating compared to the series resistance R_s. In addition, the shape of the limiting barrier will not be distorted under low voltage conditions; hence its full height can be more closely approximated. Moreover it was convenient to determine the conductance under defined conditions for all samples to eliminate data redundancy arising from variations in voltage and current spans for the different types of samples. The variation of the low voltage differential conductance with temperature for a printed metallurgical grade silicon sample is shown in Fig. 5.25.

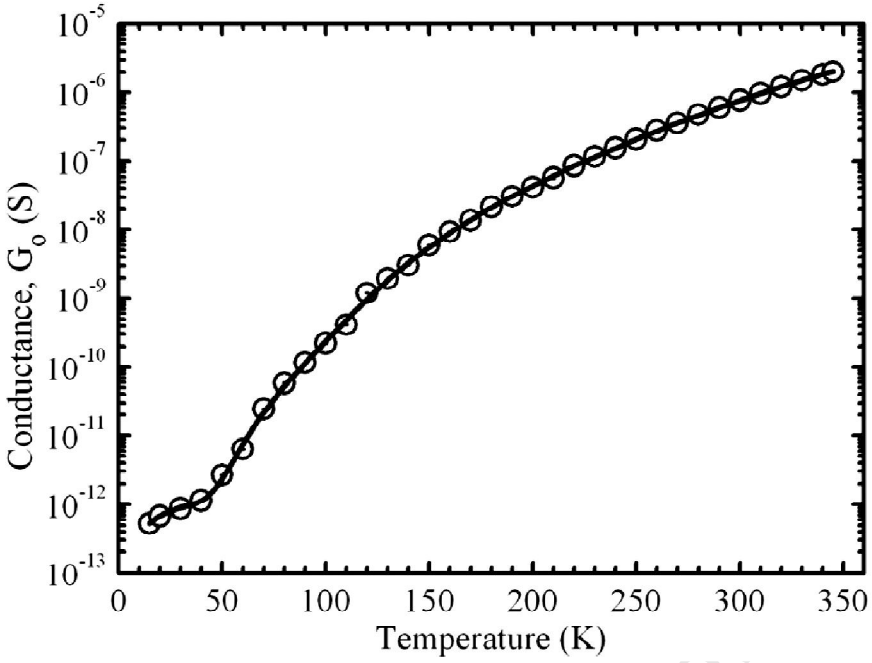

Fig. 5.25: Variation of low voltage differential conductance with temperature for a printed metallurgical grade silicon device. Plotted points represent the experimental data and the solid line is the model fit to the experimental data. Statistical errors are similar in size to the plot symbols.

By adopting a parallel conductance model [9, 10], namely that the conductance is considered to be the sum of the conductances, $g_i = g_{0i}\exp(-\beta_i/T)$, from k parallel paths through a conducting network, giving an overall conductance, G_0, given by

$$G_0 = \sum_{i=1}^{k} g_{0i}\exp\left(\frac{-\beta_i}{T}\right), \tag{5.17}$$

where the pre-factors g_{0i} provide information concerning the conductance of the path requiring activation energy of characteristic temperature β_i at absolute temperature T. G_0 corresponds to the definition in equation (5.16). Initially a spectral analysis was applied in which equation (5.17) was fitted to the data with $k = 31$ and the characteristic temperature values β_i fixed at $10, 20, 50$ and then in increments of 100 up to 2800. Fitting equation (5.17) to the experimental data for printed metallurgical grade silicon devices invariably resolved four clusters of β values as shown in Fig. 5.26.

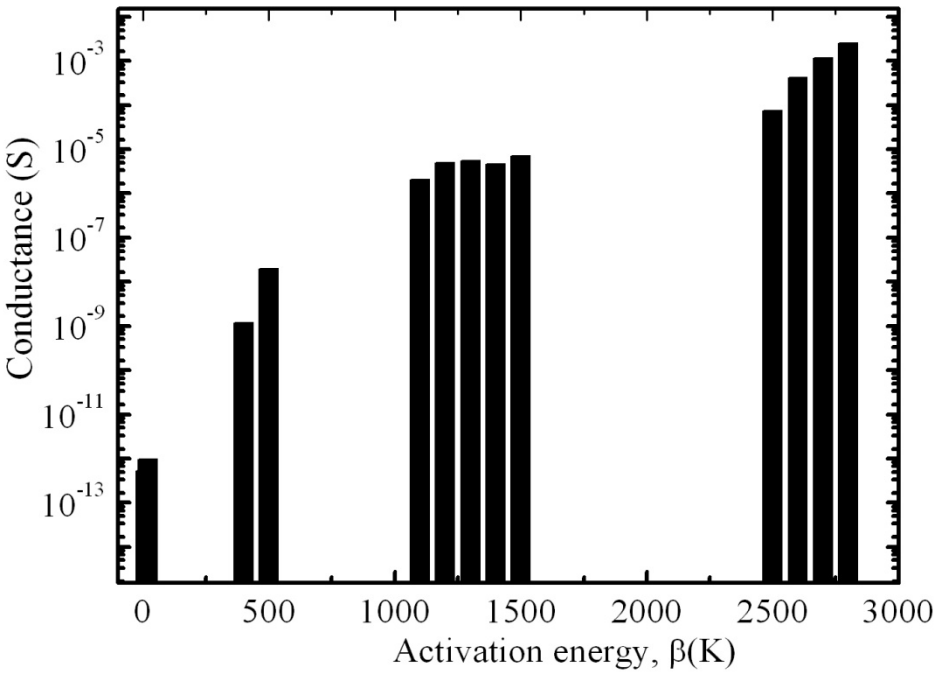

Fig. 5.26: Occurrence of activation energies for charge transport in a printed metallurgical grade silicon nanoparticle network.

The β values are an indicator of the activation energies limiting charge transport in the nanoparticle network. The pre-factors g_{0i} correlate with the intensity of the conductance associated with particular activation energy β_i. This fitting exercise provided a guideline with respect to the number of exponential terms required in equation (5.17) to fit the low voltage conductance-temperature data. Over an extended temperature range of 15-345K, the low voltage conductance, G_0, was therefore described by four components as

$$G_0 = g_{01}\exp\left(\frac{-\beta_1}{T}\right) + g_{02}\exp\left(\frac{-\beta_2}{T}\right) + g_{03}\exp\left(\frac{-\beta_3}{T}\right) + g_{04}\exp\left(\frac{-\beta_4}{T}\right). \qquad (5.18)$$

The model defined in equation (5.18) is shown as a solid line in Fig. 5.25. The appearance of the β values on the $G_0 - T$ profile was ascertained by first deriving the relationship between β and temperature, T. If one term of equation (5.18) is considered: $G = g_0\exp(-\beta/T)$, then

$$\frac{dG}{dT} = \frac{\beta g_0}{T^2}\exp\left(\frac{-\beta}{T}\right),$$

or

$$\frac{dG}{dT} = \frac{\beta G}{T^2}.$$

Therefore

$$\beta = \frac{T^2}{G}\frac{dG}{dT}. \qquad (5.19)$$

Equation (5.19) was then used to calculate effective β values at each temperature. The variation of β with temperature is displayed in Fig. 5.27. Of interest are the four saddles appearing on the $\beta - T$ profile. These are delineated by the broken elliptic outlines superimposed on the curve. At low temperature a sharply defined plateau is evident. The sharpness of the plateaus becomes smeared as temperature increases, as can be seen in increased slopping of the shoulders. At low temperature (15-40 K), only one β can be seen. As temperature increases to 100 K, and between 50-100 K another plateau can be perceived, but it is less sharply defined. The smearing of the plateaus may be due to the mixture of the low temperature βs with the next one becoming effective just below 100 K. More smearing of the otherwise flat regions continues to appear at higher temperatures as it becomes more difficult to resolve the activation energies. Thus, the nanoparticle system is characterised by a distribution of barriers which cluster around four characteristic values.

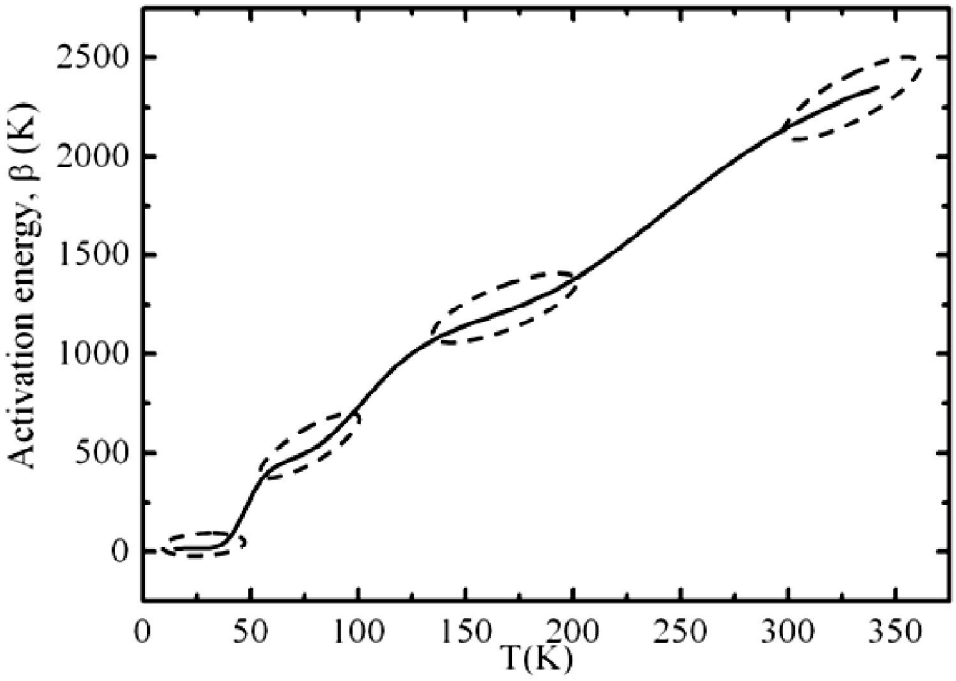

Fig. 5.27: Evolution of activation energy with temperature. The saddle points are delineated by circular outlines.

To more clearly determine the four characteristic activation energies, the curve in Fig. 5.27 was differentiated and a graph of $\frac{d\beta}{dT}$ against β was plotted as in Fig. 5.28.

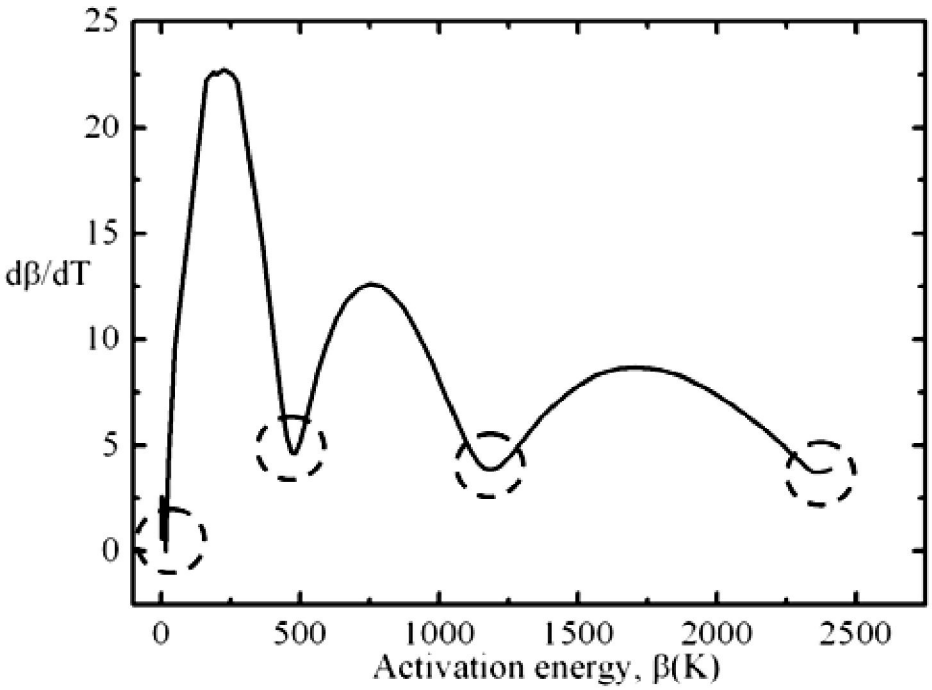

Fig. 5.28: Resolution of characteristic activation energies for a 2503 grade silicon sample.

The minima, demarcated by broken circles, give the characteristic activation energies associated with the saddle points in Fig. 5.27. These four β values were consistent with those obtained from direct fitting of the $G_0 - T$ data using equation (5.18).

Table II: Activation energies for milled metallurgical grade silicon samples of different particle concentrations.

Particle Concentration (%)	β_1 (K)	β_2 (K)	β_3 (K)	β_4 (K)
50	-	262 ± 26*	1408 ± 394	
60	-	-	709 ± 82*	2280 ± 329
70	13.27 ± 3.68	345 ± 47	1033 ± 37	2194 ± 84
80	12.15 ± 1.89	451 ± 54	1162 ± 70	2284 ± 125
88	13.33 ± 1.44	444 ± 38	1232 ± 46	2418 ± 139

* These activation energies may identify with those under which they have been classified. The discrepancy is perceived to be a measurement artefact related to the samples being highly resistive, yielding noisy data. This might have affected the resolution of the exponential terms in the fitting procedure.

Milled silicon samples of particle concentrations of at least 70% typically yielded $\beta_1 = 15\,K, \beta_2 = 450\,K, \beta_3 = 1200\,K,$ and $\beta_4 = 2300\,K$. For particle concentrations of 50% and 60%, the samples were too resistive to be measurable below 100 K. As such, only two characteristic activation energies could be resolved. Moreover, the data for these two particle loadings was noisy resulting in poor fits to the $G_0 - T$ plots. TABLE II summarises the activation energies for milled metallurgical grade silicon test devices of different particle concentrations.

The effect of particle loading on the activation energies is clearly shown in Fig. 5.29. Within the uncertainty of measurement, the low temperature activation energy β_1 is invariant for different particle concentrations as shown in Fig. 5.29 (a).

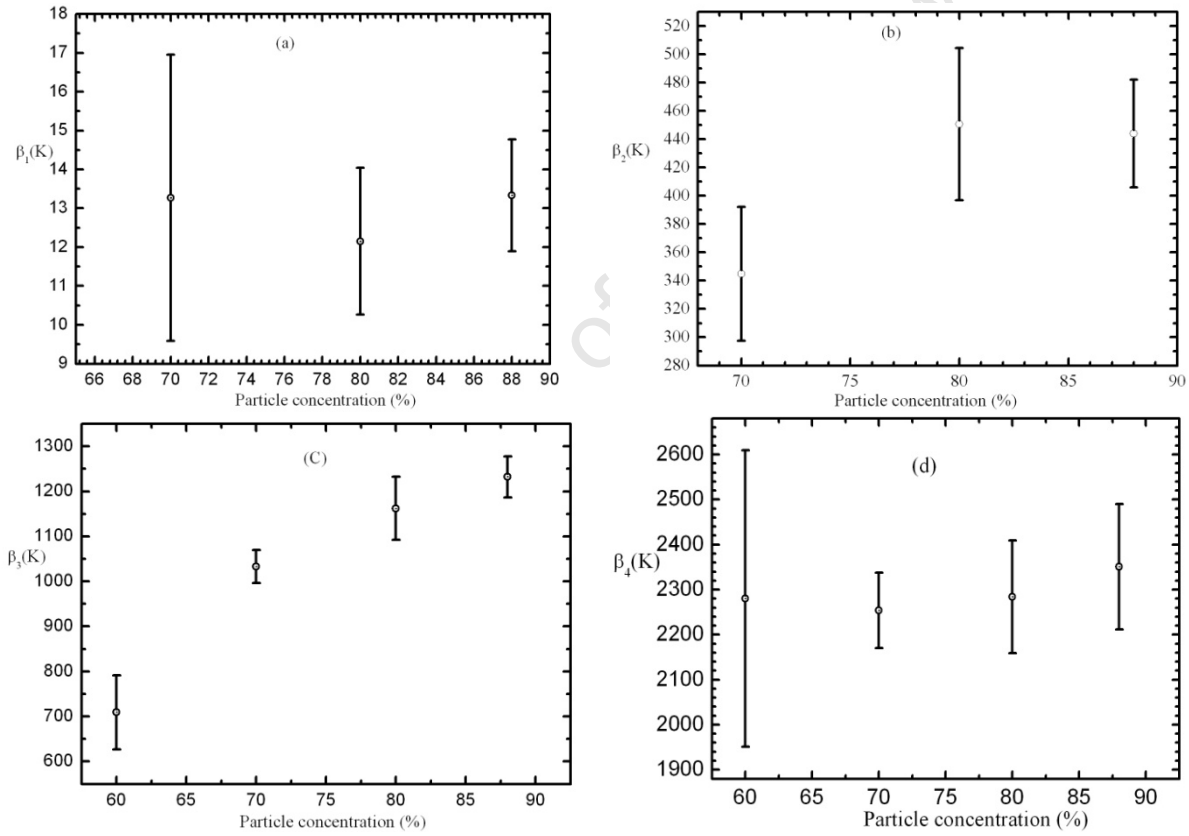

Fig. 5.29: Influence of particle loading on activation energies for milled M-Si test devices.

Clearly the three higher activation energies (Fig. 5.29 (b)-(d)) are influenced by particle concentration, but with a tendency to saturate at higher particle concentrations. The high temperature activation energy, β_4 is not as sensitive to particle concentrations greater than 70% as is the case with β_3. The small error bars in Fig. 5.29 (c) can be attributed to the energy activated processes which are associated with more conduction paths which give good

statistics. The highest activation energy β_4, implies more difficult transitions hence giving large scatter in the resolved values. At low temperature, the samples were highly resistive resulting in noisy data which results in the large error bars on the activation energies β_1 and β_2.

Activation energies of different types of printed silicon devices are shown in TABLE III.

TABLE III: Activation energies for different types of printed silicon at 88% particle loading.

Type of silicon	β_1 (K)		β_2 (K)	β_3 (K)	β_4 (K)
M	13.3 ± 1.4		444 ± 22	1232 ± 46	2418 ± 140
p	18.3 ± 6.2		452 ± 13	1180 ± 110	2168 ± 110
n	14.2 ± 3.5		429 ± 21	1182 ± 78	2413 ± 180
CVS	15.3 ± 4.6	$180 \pm 54^*$		974 ± 21	

*This activation energy cannot identify with any of those observed for silicon produced from milled nanoparticles.

Printed layers produced from milled nanoparticles displayed similar activation energies for the extended temperature range of 15-345 K. The four types of printed silicon showed similar low temperature activation energy, β_1. Structures printed from *p*-type nanoparticles produced by CVS showed three characteristic activation energies, as opposed to four shown by samples from milled nanoparticles. Only the low temperature activation energy is similar to that observed for milled samples. The other two are distinct from those associated with milled samples. However, within uncertainty limits, the higher temperature activation energy of 974 K for particles produced by CVS may identify with β_3 of samples produced from milled nanoparticles. In a broad sense, printed silicon produced from nanoparticles synthesised by CVS displayed lower activation energies compared to those of milled nanoparticles.

In addition to information concerning the activation energies for charge transport, the pre-exponential factors g_{01}, g_{02}, g_{03} and g_{04} in equation (5.18) are expected to provide an insight into the conductances associated with the corresponding activation energies. These pre-exponential factors are also expected to be influenced by the integrity of the printed films and the preparation history of the test devices. Comparison of absolute values of the pre-exponential factors would result in data redundancy. In order to investigate the variation of these conductances with particle loading, normalised values were used. For each sample, the normalised conductance, a_i, associated with a pre-exponential factor g_{0i}, in equation (5.18) is given by

$$a_i = \frac{g_{0i}}{g_{01} + g_{02} + g_{03} + g_{04}}. \tag{5.20}$$

The average normalised conductance, A_i corresponding to a_i for a group of N samples of a particular particle loading is then given by

$$A_i = \frac{a_i^{(1)} + a_i^{(2)} + a_i^{(3)} \ldots a_i^{(n)}}{N}. \tag{5.21}$$

The variation of the normalised conductances with particle loading is shown in Fig. 5.28. The normalised conductances A_1, A_2, A_3, and A_4 correspond to the activation energies, β_1, β_2, β_3 and β_4 respectively.

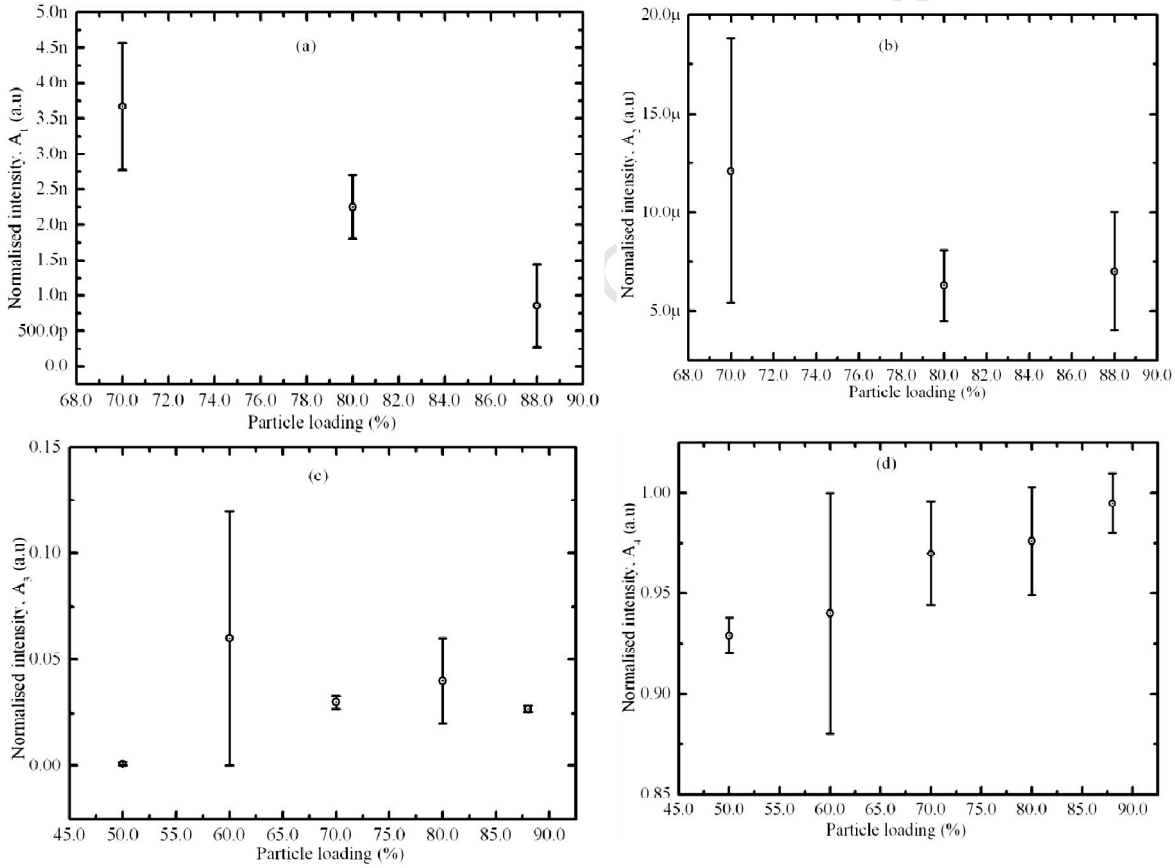

Fig. 5.30: Dependence of normalised conductances (a) A_1, (b) A_2, (c) A_3, and (d) A_4 with particle loading for metallurgical grade silicon samples.

The normalised conductance A_1 clearly decreases with particle loading for devices of 70% to 80% particle concentrations as shown in Fig. 5.30 (a). For A_2, corresponding to β_2, it can be said that the normalised conductances are similar within the given measurement uncertainties as shown in Fig. 5.30 (b). Fig. 5.30 (c) shows that A_3 is invariant for particle concentrations

above the upper percolation threshold and is lowest at 50% which is way below the upper percolation threshold. A_4 slowly increases with particle concentration with a tendency to saturate at high particle concentrations as in Fig. 5.30 (d). For a particular batch of samples, the normalised conductance prefactors were observed to increase with activation energy as illustrated in Fig. 5.31 for a group of samples of 80% particle concentration.

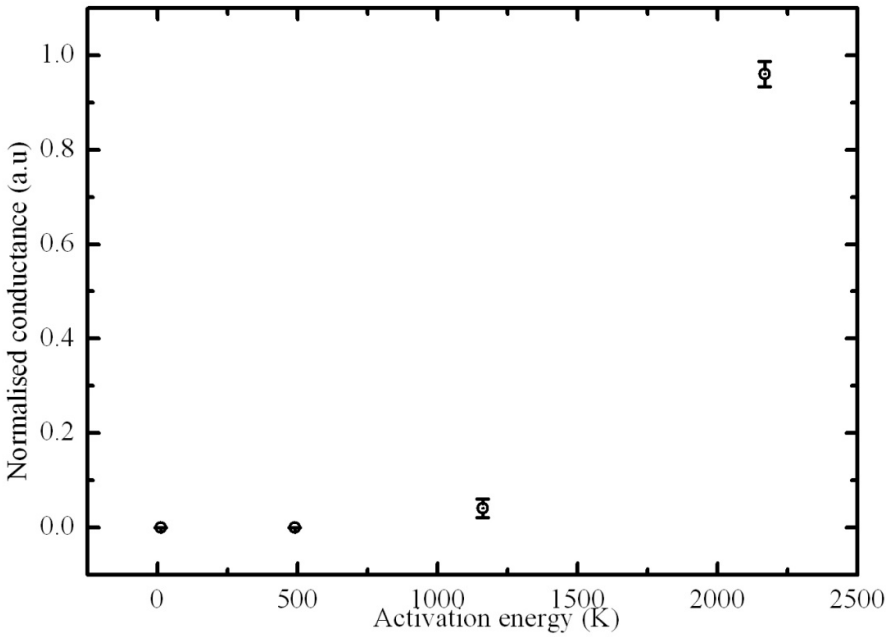

Fig. 5.31: Correlation between conductance prefactors and observed activation energy for 80% metallurgical grade samples.

Samples of other filler content and type showed a similar correlation. The normalised conductance prefactors is an indicator of the number of conduction paths. Fig. 5.31 shows that the number of conduction paths increases as the charge carriers acquire more thermal energy.

As outlined before, the fit to the *IV* characteristic yielded two parameters: the diode ideality factor, η, and the reverse saturation current, I_0. The evolution of I_0 with temperature for a cup and ball metallurgical grade silicon test structure is displayed in Fig. 5.32. The saturation current increases non-linearly with temperature as shown in Fig. 5.32. In fact, the increase in saturation current with temperature is exponential in nature and varies with temperature in a similar way as the low voltage conductance, G_0.

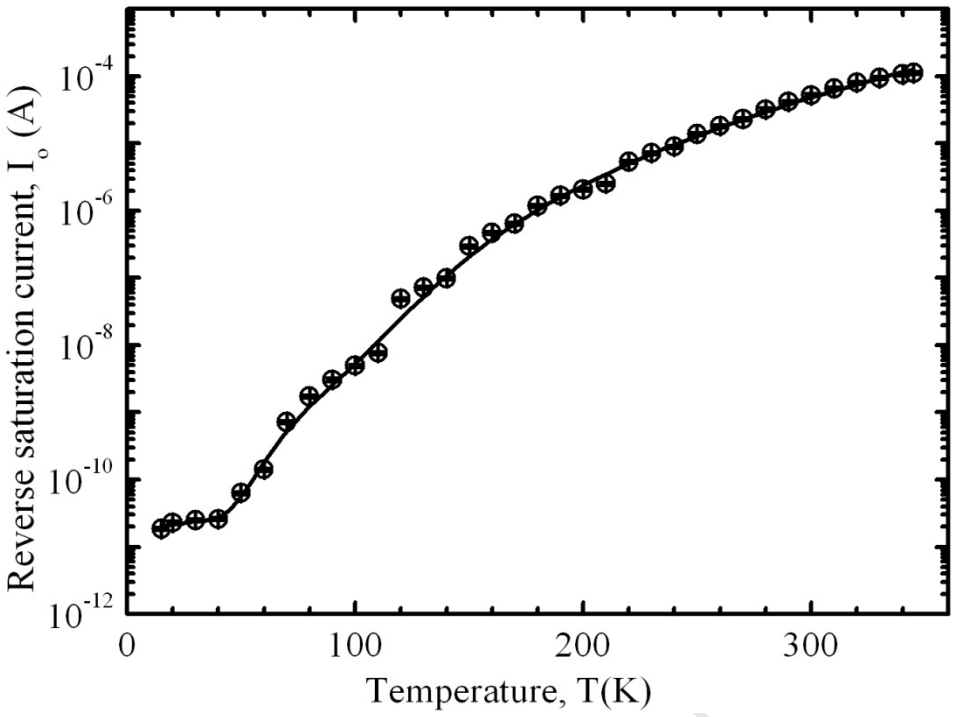

Fig. 5.32: Variation of saturation current with temperature for an M-Si test device.

The temperature dependence of the reverse saturation current was described by

$$I_0 = \sum_{i=1}^{4} l_{0i} \exp\left(\frac{-\beta_i}{T}\right), \tag{5.22}$$

where β_i is the activation energy for charge conduction and l_{0i} is a pre-exponential factor which is proportional to the rate at which carriers are moving over barriers of energy β_i independent of the applied electric field. The activation energies obtained from the *Io-T* fits are the same as those resolved from the conductance analysis.

The diode ideality factor is high at low temperature and decreases to a limiting value at high temperature for all samples measured as shown in Fig. 5.33. Generally, the diode ideality factor is very high, being about three orders of magnitude higher than that of a single junction diode at room temperature. This arises from the nature of the conducting nanoparticle network. A full discussion of the significance of the ideality factor for the nanoparticle network is given in chapter 6.

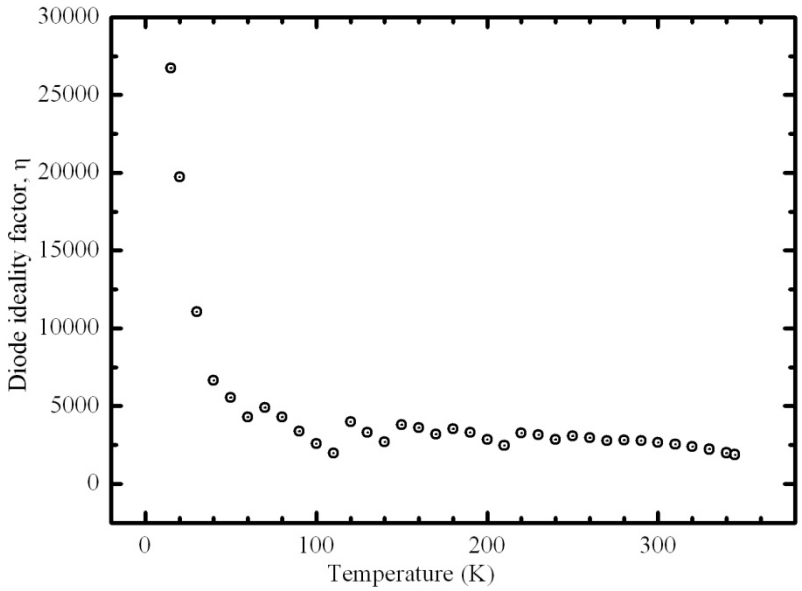

Fig. 5.33: Evolution of the diode factor with temperature.

Evident in the temperature profiles of I_0 and η are breaks in the otherwise smooth trends (e.g. at 70 K, 120 K, 210 K etc) giving an almost systematic clustering of data points. This was noted to be an artefact of the measurement process arising from instrument range change which was inevitable as the current source meter, nanovoltmeter and picoammeter were used in auto ranging mode as designed by the manufacturer, LakeShore Cryotronics Inc..

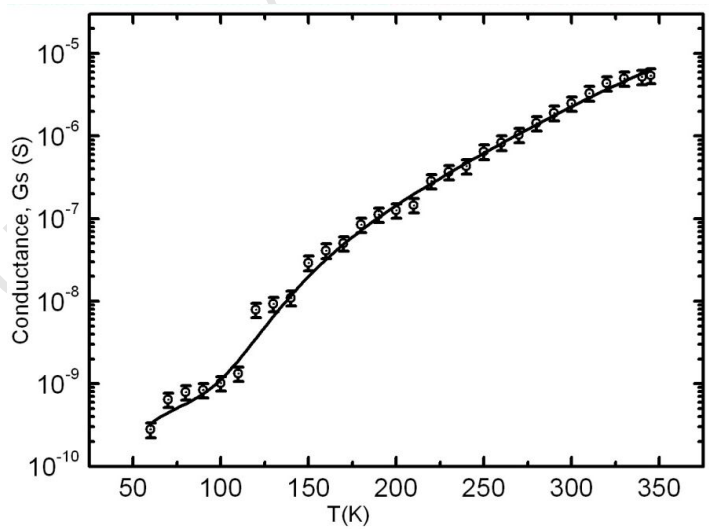

Fig. 5.34: Typical temperature dependence of series conductance for a printed metallurgical grade silicon sample.

The series conductance, $G_s = 1/R_s$ showed the same temperature dependence as the effective conductance described by equation (5.18). The breaks seen in the data points are due to instrument range change. The temperature dependence of the series conductance is shown in

Fig. 5.34. The same values of activation energies for conduction, β_i and the conductance pre-factors, g_{0i} were obtained from fitting equation (5.18) to the $G_s - T$ data for the same temperature range. This shows that charge transport along any established path is limited by the effective barrier. Only charge carriers of energy at least equal to the effective barrier can flow along the path.

5.5.2 Variable temperature Hall effect measurements

Field dependent Hall effect data for silicon printed from milled nanoparticle inks were obtained at different temperatures extending from 15 to 345K. The sample geometry was based on the van der Pauw structure shown in Fig. 4.11 and measurement was performed using the LakeShore Hall effect measurement system. A two carrier model was used to fit the principal components of a magneto-conductivity tensor [10]. A rank 2 conductivity tensor was assumed since the printed film is a 2-dimensional layer. During the Hall effect experiment, the HMS performs repeated measurements in longitudinal and transverse directions to the layer in the van der Pauw test structure to obtain the average electronic transport characteristics of the sample. For this reason, it is justified to use a symmetric conductivity tensor for the analysis. The principal components of the conductivity tensor are: the longitudinal component, σ_{xx}, and the transverse component, σ_{xy}. The analysis also assumes symmetry in the direction of electric current in the measurement process. This is plausible based on the fact that the four silver contacts were symmetrically arranged so that each axis joining opposite pairs of contacts was oriented at 45° to the print direction giving the same projection with respect to the direction in which the silicon is printed.

At a particular temperature, the conductivity tensor components for a material with a single type of charge carrier are given by [10]

$$\sigma_{xx} = \frac{nq\mu}{1+\mu^2 B^2}, \tag{5.23}$$

and

$$\sigma_{xy} = \frac{nq\mu^2 B}{1+\mu^2 B^2}, \tag{5.24}$$

where μ is the mobility, q is the charge, and B is the magnetic field. For a system with more than one carrier type, the mobilities and carrier concentrations have to be averaged over all carriers. For such materials, the total conductivity is given by [11]

$$\sigma_{xx} = \sum_{i}^{N} \frac{n_i q_i \mu_i}{1+\mu_i^2 B^2}, \tag{5.25}$$

and $$\sigma_{xy} = \sum_{i}^{N} \frac{n_i q_i \mu_i^2 B}{1+\mu_i^2 B^2}\ , \tag{5.26}$$

where $i=1, N=2$ in this study. To determine the carrier concentration and mobility of majority and minority carriers present in the nanoparticle network at each temperature, variable magnetic field measurements had to be performed. Fig. 5.35 shows the magneto-conductivity data for printed silicon using nanoparticles milled from *n*-type silicon.

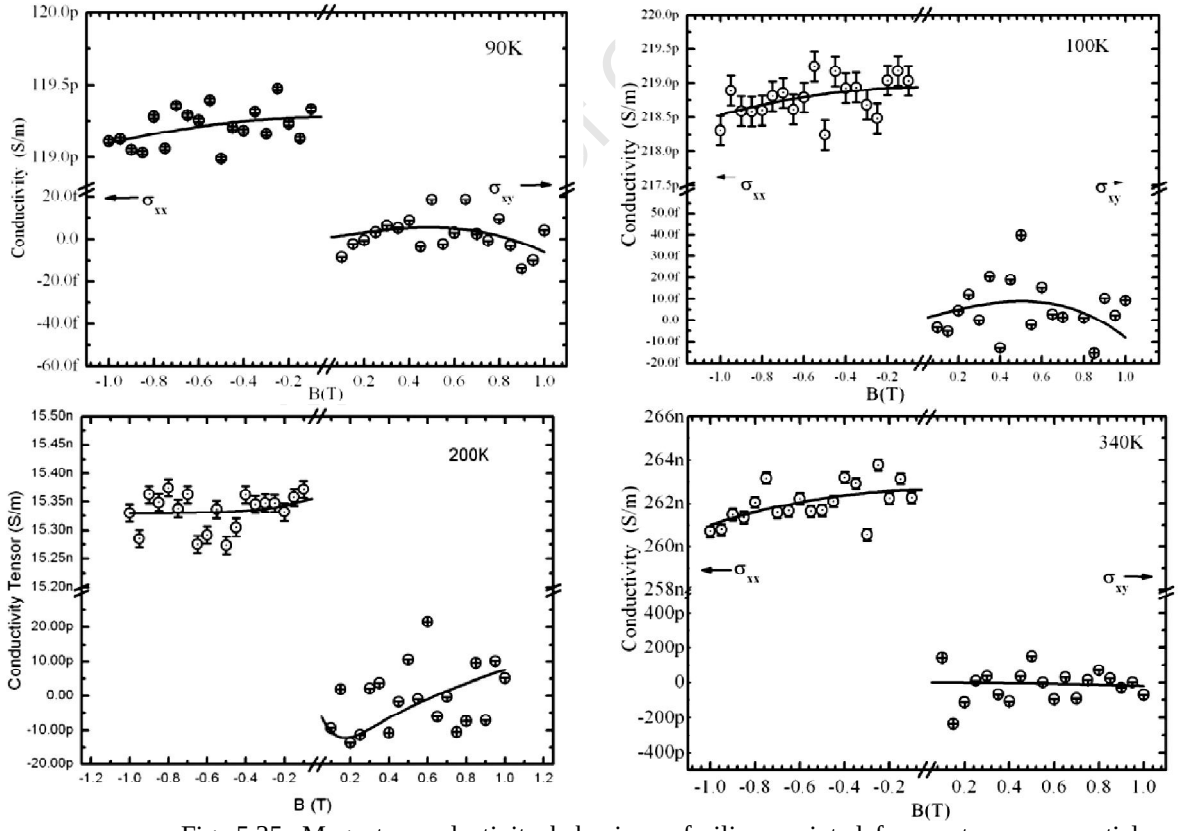

Fig. 5.35: Magneto-conductivity behaviour of silicon printed from *n*-type nanoparticles at different temperatures. The solid lines are the two carrier model conductivity tensor component fits to the measurement data points.

The data show significant scatter owing to the high resistivity of the material under study. However the variable magnetic field Hall effect measurements enables data analysis that yields statistical averaging of the electrical behaviour of the material.

To ascertain the influence of the substrate, the same variable temperature magneto-conductivity measurements were performed using a reference sample consisting of the substrate with printed contacts alone but no silicon. For temperatures below 280 K, the substrate alone was too highly resistive to be measurable. For temperatures of 280 K and above, the substrate showed a small contribution which was relatively constant as temperature increased. For temperatures from 280-345 K, the fitting procedure included a background correction to account for the contribution from the substrate. For lower temperatures, the substrate would not be expected to significantly influence the Hall effect data.

The analysis of the Hall effect data was performed in four steps. Initially equations (5.25) and (5.26) were fitted to the data to obtain mobility and carrier concentration values at each temperature point. Two pairs of such values were obtained at each temperature, the two pairs corresponding to the mobility and carrier concentration for each of the two carrier types. The temperature profiles for each of the four fit parameters was then plotted. Invariably the data was scattered about some average trend line in each case. In the second step, a phenomenological equation was fitted to the individual mobility temperature profiles so as to reconstruct clean data of the mobilities. In the third step, the mobility values obtained after the reconstruction were then set as fixed parameters in the magneto-conductivity model and the Hall effect data was refitted to obtain carrier concentration. Finally, the carrier concentration obtained in the third step was then set as fixed parameters in the magneto-conductivity model and fitting repeated to obtain mobilities.

Typical mobility and carrier concentration data for milled samples of 80% particle loading at 300 K are shown in TABLE IV. From the data, it is evident that the conductivity of the silicon nanoparticle network is characterised by two carrier types of opposite sign. All the measured samples showed a majority carrier type which was consistent with the doping of the bulk material. No reversal of the expected carrier type was observed. However for 10% of the metallurgical grade samples there was no difference in the orders of magnitude of the concentration for the two carrier types. This was not surprising since the metallurgical grade silicon was not of clearly defined resistivity; being reported by the manufacturer to contain,

among other impurities aluminium at 0.144% and phosphorous at 43 ppm which could make it *p*- and *n*-type doped respectively.

TABLE IV: Hall effect data for typical samples printed from milled silicon nanoparticle inks at 80% particle concentration as measured at 300 K. N and P represents *n*- and *p*-type silicon based samples respectively, where as M represents metallurgical grade silicon samples. The number '80' designates the particle concentration as a percentage. The last digits after '80' are the print numbers in the series. H is the test structure designation, and the last digit is the location of the test structure on the printed substrate. n_e and n_h are the electron and hole sheet concentrations, and μ_e and μ_h are the corresponding electron and hole mobilities respectively.

	N80-01H3	P80-028H3	M80-07H2
$n_h\,(1/\mathrm{m}^2)$	$(2.031 \pm 0.014)\mathrm{x}10^{13}$	$(7.366 \pm 0.018)\mathrm{x}10^{15}$	$(8.717 \pm 0.073)\mathrm{x}10^{12}$
$n_e\ (1/\mathrm{m}^2)$	$(-1.023 \pm 0.052)\mathrm{x}10^{15}$	$(-4.974 \pm 0.27)\mathrm{x}10^{13}$	$(-9.61 \pm 0.031)\mathrm{x}10^{15}$
$\mu_h\,(\mathrm{m}^2/\mathrm{Vs})$	$(6.087 \pm 0.035)\mathrm{x}10^{-4}$	$(5.83 \pm 0.10)\mathrm{x}10^{-4}$	$(3.67 \pm 0.018)\mathrm{x}10^{-4}$
$\mu_e\,(\mathrm{m}^2/\mathrm{Vs})$	$(6.343 \pm 0.071)\mathrm{x}10^{-3}$	$(2.03 \pm\ 0.43)\mathrm{x}10^{-3}$	$(1.44 \pm 0.039)\mathrm{x}10^{-4}$

The temperature dependence of the zero field conductivity of a printed *n*-type test structure is shown in Fig. 5.36. The behaviour is described by

$$\sigma = \sum_{i=1}^{4} \sigma_{0i} \exp\left(\frac{-\beta_i}{T}\right), \tag{5.27}$$

where σ_{0i} is a pre-exponential factor which depends on sample preparation history and β_i is the activation energy for conduction.

Fitting equation (5.27) to the data in Fig. 5.36 yielded four activation energies for conduction which are similar to those obtained from fitting conductance-temperature data described in section 5.5.1.

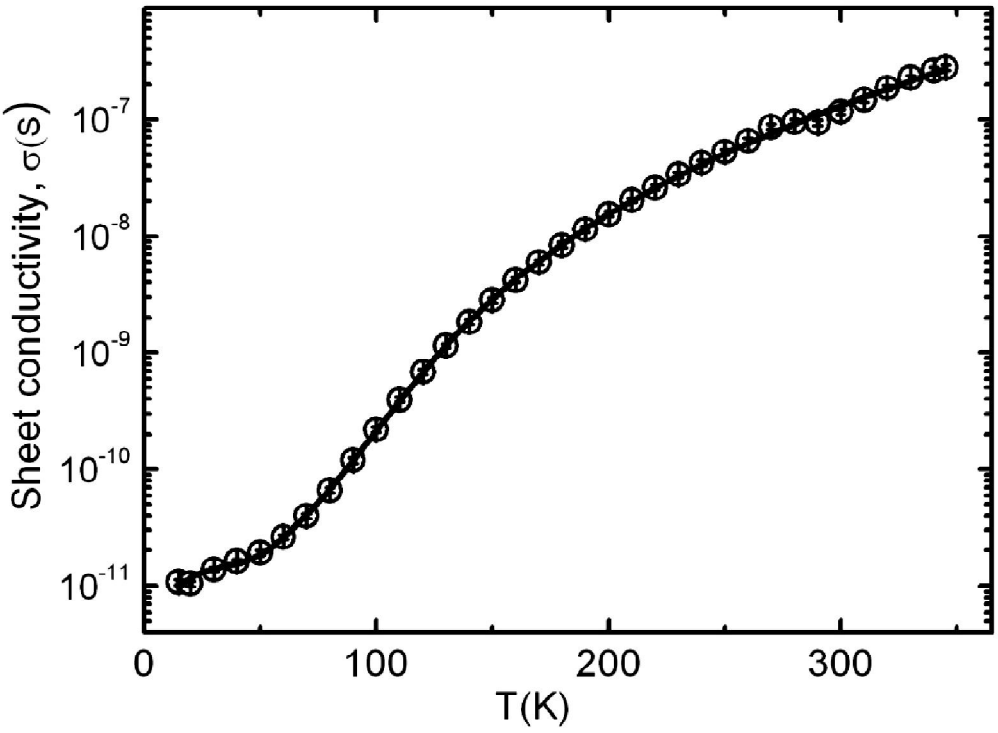

Fig. 5.36: Zero field conductivity-temperature behaviour of a test structure printed from milled *n*-type silicon nanoparticles at 80% particle loading. The solid line is a model fit to the measurement data points.

The normalised prefactors, σ_{0i}, obtained by fitting equation (5.27) to the conductivity data showed strong correlation with the corresponding normalised prefactors, g_{0i}, obtained from the conductance data. This correlation, shown in Fig. 5.37, is linear which further supports the consistency of data obtained from the two experiments.

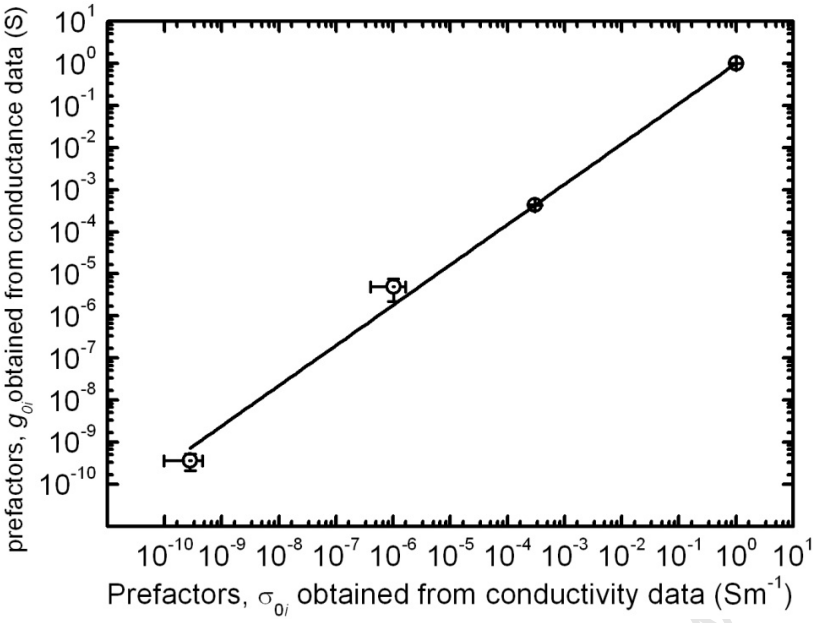

Fig. 5.37: Correlation between prefactors, g_{0i} and σ_{0i} obtained from variable temperature conductance and Hall effect data respectively. The solid line is a linear fit showing the strong correlation between the two sets of data.

The variation of the electron and hole concentration for an *n*-type and a *p*-type sample of 80% particle loading is shown in Fig. 5.38 (a) and (b) respectively. From Fig. 5.38, it can be seen that the carrier concentrations increase with temperature in an exponential fashion. The two carrier types show similar temperature dependence with both carrier concentrations changing by up to six orders of magnitude over the same temperature range of 15-345K. The shapes of the carrier concentration-temperature profiles are similar to the conductance temperature behaviour shown in Fig. 5.25 and Fig. 5.36. The temperature dependence of the carrier concentration can be described by

$$n = \sum_{i=1}^{4} n_0 \exp\left(\frac{-\beta_i}{T}\right) \tag{5.28}$$

where n_0 is a pre-exponential factor which is proportional to the number of carriers moving after acquiring a thermal activation energy of β_i. This model assumes that the transport of carriers is characterised by thermal activation over barriers of energy β_i. Equation (5.28) enables us to independently resolve the transport activation energies of the two carrier types.

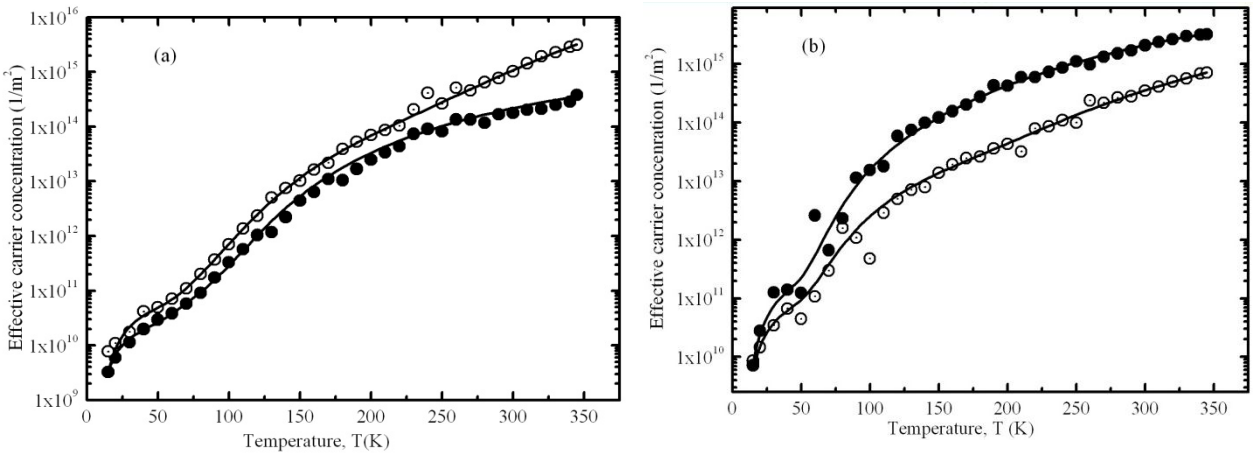

Fig. 5.38: Temperature dependence of sheet carrier concentration for (a) an *n*-type and (b) a *p*-type sample. Solid circles in the plots represent hole concentrations, whereas open circles represent electron concentration. Solid lines in (a) and (b) are model fits to the respective carrier concentrations. Statistical errors are similar in size to the plot symbols.

Both the majority and minority carrier concentrations tend to reach saturation at high temperature. The minority carrier concentration is always lower than the majority concentration as expected. After fitting equation (5.28) to the majority carrier concentrations, it was established that hole conduction is characterised by three activation energies over the temperature range of 15-345K as opposed to four observed for electrons. The three low temperature activation energies characteristic of hole conduction are also common to electron conduction. Hole conduction cannot occur over barriers requiring up to 2500K of activation energy, unlike electron conduction. Essentially, the observed activation energies are similar to those observed from the previous analyses of conductance, series resistance and conductivity. Despite the outlined differences in activation energies for holes and electrons, fitting equation (5.28) to the effective carrier concentration for both *p*- and *n*-type samples yielded the same activation energies as obtained from the conductance analysis. The number of activation energies for electron conduction are the same as those obtained from the conductance analysis. TABLE V (a) and (b) summarises the activation energies obtained from analysing the temperature dependence of the concentration of holes and electrons for an *n*- and a *p*-type sample.

TABLE V: Observed average activation energies for carrier conduction in printed silicon of 80% particle loading for (a) *p*-type samples, and (b) *n*-type samples.

(a)

	β_1 (K)	β_2 (K)	β_3 (K)	β_4 (K)
Electrons	54 ± 36	508 ± 130	1120 ± 94	2456 ± 190
Holes	61 ± 24	534 ± 71	1303 ± 130	-

(b)

	β_1 (K)	β_2 (K)	β_3 (K)	β_4 (K)
Electrons	43 ± 16	517 ± 110	1117 ± 89	2638 ± 280
Holes	41 ± 18	$478 \pm 93)$	1143 ± 130	-

The observations show that the transport of charge is characterised by thermal activation of carriers over barriers, which is consistent with the conductance-temperature measurements discussed in section 5.5.1. The relatively large uncertainties in the data are associated with the scatter typical of Hall effect measurements of highly resistive samples.

To get an insight into possible scattering processes affecting charge transport, the Hall mobilities of electrons and holes were plotted as functions of temperature as shown in Fig. 5.39. Both electron and Hall mobilities slightly decrease with temperature and nearly followed a power law behaviour. Electron mobility was higher than hole mobility as expected owing to differences in their effective masses.

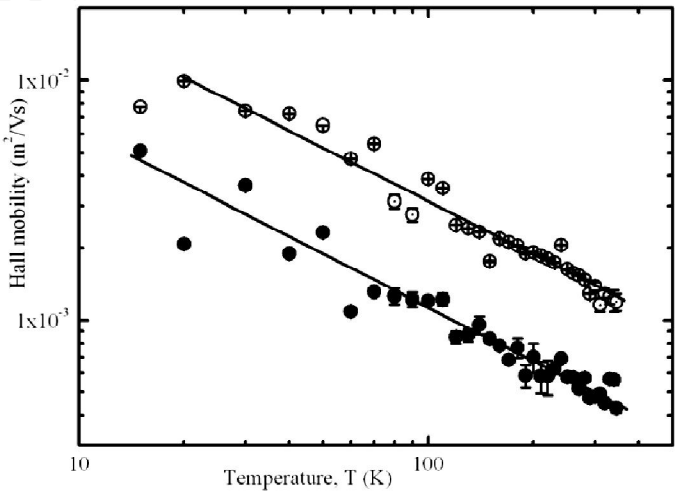

Fig. 5.39: Variation of Hall mobility of electrons and holes for a sample printed from *p*-type silicon nanoparticle ink at 80% particle loading.

The room temperature hole and electron Hall mobilities were in the order of $10-100\ cm^2/Vs$ and 1-10 cm^2/Vs respectively. In this nanoparticle system, Hall mobilities refer to the movement of carriers that have been displaced from the longitudinal current. The measured Hall mobility refers to the movement of carriers inside the particles in the transverse direction and gives negative temperature dependence as opposed to that observed in polycrystalline systems. The general decrease of mobilities with temperature is attributable to temperature induced scattering processes which become more pronounced as temperature increases. This is expected since the carrier relaxation time between scattering events decreases with temperature. As temperature increases, the density of phonons increases and acoustic phonon interaction is expected to increase. Theoretical calculations reveal that the temperature dependence of mobility due to acoustic phonon scattering in non-polar semiconductors such as silicon varies as $T^{-3/2}$ [12]. The temperature dependence of mobility in the printed silicon network can be described by a T^{-p} law, where $p = 0.725 \pm 0.055$ for both electron and hole mobilities. To a good approximation, the mobility therefore varies as $T^{-3/4}$. The reduction in the magnitude of the power law exponent from $3/2$ to $3/4$ can be attributed to additional scattering rates arising from the surface of the nanoparticles and the nature of the interface between the particles. This interface scattering effect is envisaged to be large and relatively constant resulting in very short times in between collisions giving rise to the characteristic low mobilities which weakly depend on temperature. This further supports the fact that the charge transport in the silicon nanoparticle network is interface dominated.

6 Discussion

Both the nanoparticles produced by chemical vapour synthesis (CVS) and high energy milling were electrically active, and provided the platform to study charge transport characteristics in the particle networks. The average size of milled particles had a log-normal size distribution with a median size of the order of 100 nm whereas those produced by CVS averaged 35 nm. The high energy milled silicon nanoparticles formed stable clusters of different sizes such that primary particles were not easy to resolve using microscopy techniques. TEM micrographs and SAXS measurements determined the average size of the silicon particles to be 80 nm [1]. Typically when printed they form dense clusters of average size of approximately 500 nm [2, 3]. It was shown that clustering of the particles occurs even in powder form before further processing procedures such as ink mixing and printing. Nonetheless, both the mixing of the powder with a liquid to form the ink, and the printing process may result in the rearrangement of the clusters. The need to fabricate uniform layers of ideally identical resistances between test devices was fully appreciated. However, the properties of the printed films were tightly linked to several production variables which could be traced to the nanoparticle production process, ink formulation, control of print parameters, and sample preparation for electrical characterisation. As a result, the final electrical characteristics were understood to be a compromise between each of these variables. In spite of this, close monitoring of all processes was performed to ensure a reproducible behaviour of test structures with a similar preparation history.

Scanning electron microscopy of the printed films revealed that the silicon layers were highly porous with most of the surface non-uniformity coming from the regular structure of the screen mesh pattern. It has been shown that there is no complete coverage of the particles by the insulating binder in the printed film, with the result that the network of particles resembles that of a nano-porous material. Calendaring the layers resulted in near smooth layers with reduced pinhole density and lower resistivity. In cross-sectional SEM images there was no evidence of delamination at the interface between the printed silver and silicon. Layers printed from silicon ink with a particle concentration less than 80% by weight showed excellent layer integrity and mechanical stability at the expense of conductivity. SEM micrographs of printed silicon films showed clustering of nanoparticles which in turn aggregated to form bigger clusters resulting in a self similar network of clusters. This network of clusters defines a multitude of percolation channels through which charge can

move. The arrangement of the constituent primary nanoparticles in the respective clusters can have a direct influence on the manner in which charge moves through the network. For particles which are touching, the dynamics of charge transport can be described by bond percolation theory, whereas for those in films printed from inks of particle concentration well below the upper percolation threshold, which may not be touching, charges move by diffusion or site percolation [4, 5]. In a broad sense, milled particles showed a more complex morphology than those produced by CVS. TEM images showed milled silicon nanoparticles to be irregularly shaped and rough as a result of chipping off during milling, with a broad size distribution characterised by more or less spherically shaped small particles and elongated to oblate spheroidal larger particles. Nanoparticles produced by CVS were smooth and faceted and formed branches and chains with a reasonable proportion of them showing signs of sintering. The morphologies of the particles are expected to influence the nature of barriers between the particle-particle or cluster-cluster interfaces. TEM has also revealed milled particles to be poly-crystalline. The grain boundaries associated with the internal structure of the particles represents another form of interface which presents similar potential barriers to charge transport as inherent in the particle-particle boundary. Nanoparticles produced by CVS were predominantly single crystalline, hence internal interfaces would not be expected to govern charge migration.

The *IV* characteristics for both types of printed silicon test structures typically showed a form associated with a symmetric diode, which is the same as that of a varistor, and which was sensitive to both electric field and temperature. The equivalent circuit of the test structure under operation consists of a diode in series with a resistor as shown in Fig. 5.18. This means that the charge transport is governed by the effective barrier or junction represented by the diode and the aggregated series resistance of the conduction path. The series resistance controls the shape of the *IV* curve under high absolute potential, whereas the effective diode dominates at low voltage. The differential resistance of the printed layer decreased with increasing temperature. This is evidence that charge transport in the nanoparticle network is thermally activated. It can also be noted from the varistor characteristics that the printed silicon is also susceptible to field activation. This study focused on the activation of transport, and therefore most results are presented in terms of the limiting conductance of the silicon network at zero applied voltage. Moreover, analysing conductance at low voltage reduced the influence of the series resistance, hence enabling the characteristics of the dominating junction represented by the diode to be studied. It is envisaged that for an interface between

particles or clusters, there is a potential barrier or well. If we consider a particle to particle interface as shown in Fig. 6.1, and for high electric field and thin potential barriers (common for highly doped materials),

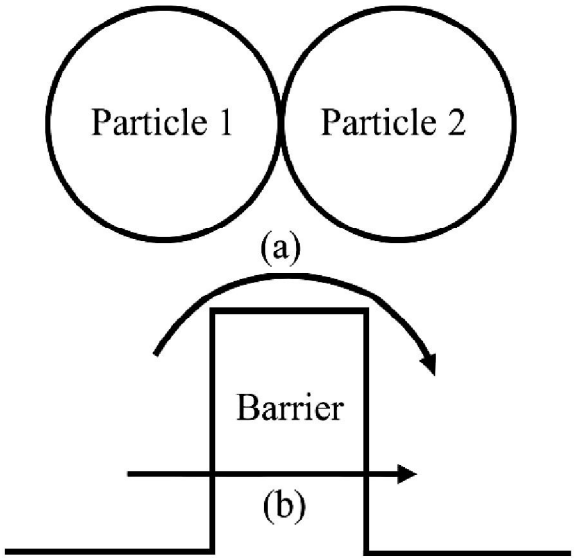

Fig. 6.1: Charge transport across a particle-particle interface. Carrier transport can be (a) activated over the barrier or (b) through tunnelling.

charge carriers tunnel through the barrier as shown in (b), whereas for lowly doped materials and at low electric field, carriers tend to surmount barriers as in (a). Moreover a high electric field distorts the shape of the barrier significantly. To extract information about the size of the barriers, using the conductance at low voltage ensured that the shape and size of barriers was not distorted. In this way the characteristic activation energies for charge transport were estimated. For conventional metal-bulk crystalline semiconductor interfaces, it is common practice to associate the symmetry of the observed *IV* curve with the two barriers at the metal-semiconductor boundaries [6]. The system under study is composed of a network of interfaces which are expected to present barriers to charge flow in addition to the two metal-semiconductor interfaces. Each of the individual interfaces presents a diode characteristic to the final and observed *IV* curve with the result that the system can be imagined to be composed of a network of such diodes in series and parallel such that at a particular temperature, only the effect produced by the limiting or effective barrier is observed. A simple illustration of this network of barriers is shown in Fig. 6.2. In each of these cases, the barriers marked with an asterisk limit the flow of charge from A to B. The remaining potential barriers do not play a significant role in limiting the charge transport.

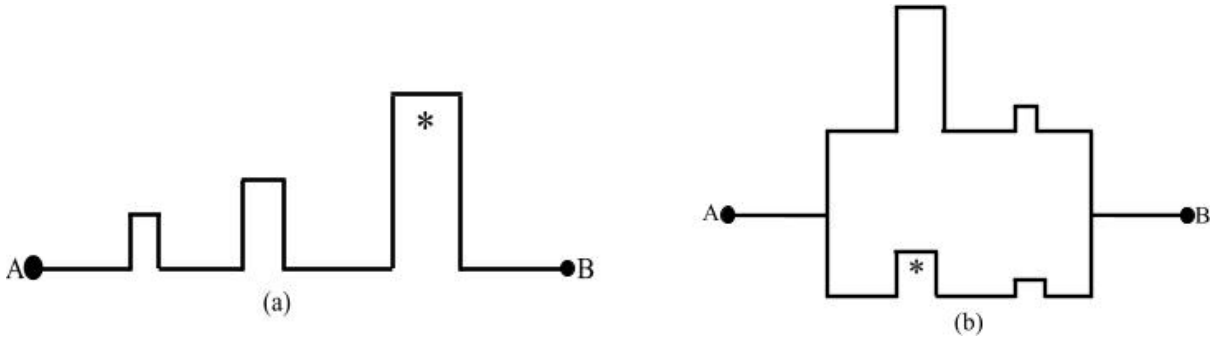

Fig. 6.2: Schematic illustration of the occurrence of the limiting barrier for (a) a series of different sizes of barriers, and (b) a parallel combination of barriers.

Fig. 6 (b) also shows the significance of a material having different potential percolation paths. The path containing the asterisked barrier dominates the charge transport owing to the smaller activation energy for transport. Hence the asterisked barrier limits the conductivity of the incumbent material since essentially no conduction occurs through the larger barrier in the alternative branch.

The low voltage conductance-temperature behaviour of the printed silicon networks has been shown to be described by a parallel conductance model that yields four characteristic activation energies for charge conduction in milled silicon nanoparticle networks. This means that the silicon nanoparticle network is characterised by a wide distribution of barriers whose energies cluster around four values. These activation energies were obtained as characteristic temperature values centred around 15 K, 450 K, 1200 K, and 2300 K. The effective activation energy measured at low temperature is the smallest and has been observed to be associated with the smallest pre-exponential factor in the conductance term $G_{01} = g_{01}\exp(-\beta_1/T)$. The higher the β value, the greater the pre-exponential factor. At low temperature, the charge carriers are expected to possess enough energy to surmount low barriers. As temperature increases, the thermal energy of the carriers increases, thereby enabling them to be excited over higher barriers. The pre-exponential factor in the conductance term is proportional to the number of paths contributing to the conductance at a given temperature. As temperature is elevated, the observed conductance manifests as an increase in the pre-exponential factor. This translates into an increase in the number of charge transport paths as carriers acquire enough energy to surmount larger barriers.

The diode ideality factor for the nanoparticle networks has been observed to be unusually high, ranging from about 1000 to 30000 for milled particles over the extended temperature

range of 15-345 K and one order of magnitude lower for nanoparticles produced by CVS. In general, the ideality factor is taken as unity for an ideal single step barrier such as the one schematically represented in Fig. 6.3 (a), and for bulk crystalline semiconductor materials in which drift and diffusion are the predominant transport mechanisms [7].

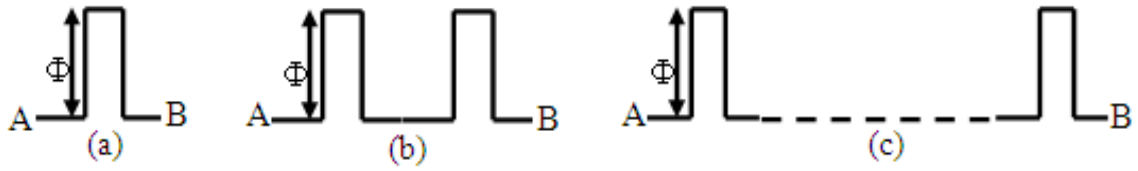

Fig. 6.3: Potential drop across step barriers of height Φ for (a) a single barrier, (b) two barriers, and (c) *n*-barriers.

If it is imagined that a potential difference, V, is applied across A and B in (a), the potential energy drop across the barrier will be proportional to $\exp(eV/K_BT)$. For two step barriers of the same height shown in (b), the potential drop across each barrier will be proportional to $\exp(eV/2K_BT)$. For η barriers, the potential drop will be proportional to $\exp(eV/\eta K_BT)$ where η is perceived to be the ideality factor in this context. An increase in the ideality factor scales the applied voltage resulting in reduced electric field at each individual barrier. This slows down carriers such that carrier recombination becomes more pronounced. The case of step barriers presented above is an oversimplified one. A high ideality factor may also be envisaged as being a superposition of barriers of different thickness, size and shape as shown in Fig. 6.4.

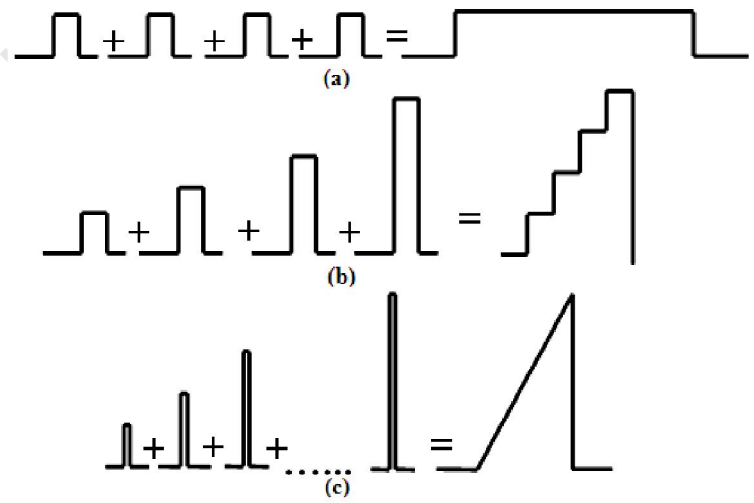

Fig. 6.4: Other considerations giving rise to high ideality factor: (a) wide step, (b) multiple step, and (c) sloping barrier.

An idealised wide step barrier can be viewed as resulting from the superposition of barriers of similar heights as shown in Fig. 6.4 (a). If the step barriers are of similar widths but different heights, then the effective barrier can be represented as in Fig. 6.4 (b). For several thin barriers of different heights, the effective barrier assumes a triangular shape as in Fig. 6.4 (c). In the light of Fig. 6.3, the diode ideality factor obtained as a fitting parameter to the IV curve of the test structures correlates with the number of barriers or interfaces crossed by carriers in moving through the nanoparticle network between two electrodes. The ideality factor is influenced by the number of junctions in the percolation path because the applied absolute potential is divided over a large number of junctions.

The ideality factor is very high at low temperature and decreases in a near exponential fashion with temperature. Combining this understanding of the ideality factor with the conductance and activation energy, a plausible explanation can be given in view of the charge transport mechanism in the nanoparticle silicon network. At low temperature, carriers have only enough thermal energy to surmount low barriers. In spite of the multitude of connected particles, the charge carriers can only follow paths of low activation energy. As a result the conduction path becomes long and winding. This tortuosity of the conduction path will manifest as high ideality factor as a result of carriers crossing many interfaces. If each particle is regarded as a resistor, then the long winding path will map out many resistors in series. This results in high resistance which shows as reduced conductance. As temperature increases, charge carriers acquire more energy to surmount higher barriers resulting in the conduction path being more direct resulting in relatively low values of the ideality factor.

Four activation energies were resolved for the nanoparticle network based on milled silicon, whereas only three were obtained for the network composed of particles produced by CVS. The smallest activation energy of 15 K was common to both silicon networks and was unaffected by the change in particle loading. The activation energies, β_2 and β_3 for milled silicon samples were sensitive to particle concentration with a tendency to saturate at high concentrations. β_4 was observed to be invariant with change in particle loading. Analysis of Hall effect data showed that this high activation energy, $\beta_4 = 2300K$ cannot be linked to the arrangement of the particles in the layer. The high activation energy was resolved for electron conduction only. This high activation energy is large enough in magnitude and spatial extent since an electron cannot tunnel through it or bypass it. A possible explanation for this might

be the presence of an electron trap state below the conduction band of the printed silicon. This is illustrated in Fig. 6.5.

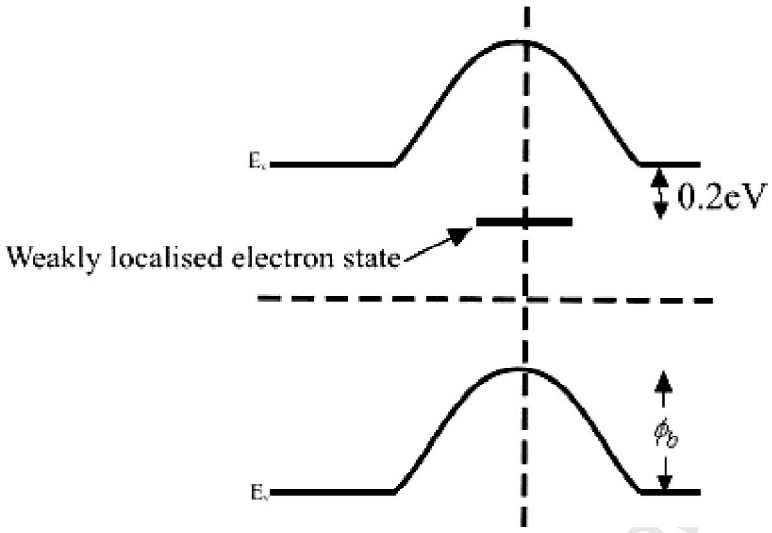

Fig. 6.5: Energy band diagram showing the electron trap state. ϕ_b is the barrier height due to interface band bending.

At high temperature, electrons hop via the trapped state, after acquiring energy of at least 0.2 eV, into the conduction band. This electron trap can be envisaged as a weakly localised electron state with an energy level corresponding to a characteristic temperature of approximately 2300 K. A possible candidate for this state is a silicon dangling bond which introduces a weakly localised energy state in the band gap at about 0.2 eV from the conduction band edge [8].

In section 5.5.2, the concentration of mobile carriers has been shown to be thermally activated. The temperature dependence of both holes and electrons has been shown to be characterised by three common activation energies, irrespective of the type of dopant. This implies that the three low temperature barriers to carrier transport are symmetric with respect to the type of charge carrier. Based on this, the three activation energies are attributable to the interface between particles. If two particles of silicon are in contact with each other as shown on a double interface energy band diagram in Fig. 6.6(a) and (b), the silicon particles will have their bulk Fermi levels matching since the particles are identical. A different Fermi level is anticipated at the interface due to the surface characteristics of the particles with the result that band bending occurs after equalisation of the Fermi levels, as shown in Fig. 6.6(c) and (d). Fig. 6.6 (a) and (c) show the dynamics of band bending in the case where the Fermi level of the interface is higher than that of the particles, which results in the formation of a

potential well. On the contrary, if the Fermi level of the interface is lower than the Fermi energy of the particles, a potential hill is formed. After equilibrium, electrons need to possess energy of at least $e\phi_b$ to move across the interface. Similarly, a hole needs the same amount of energy to migrate across the interface in the opposite direction.

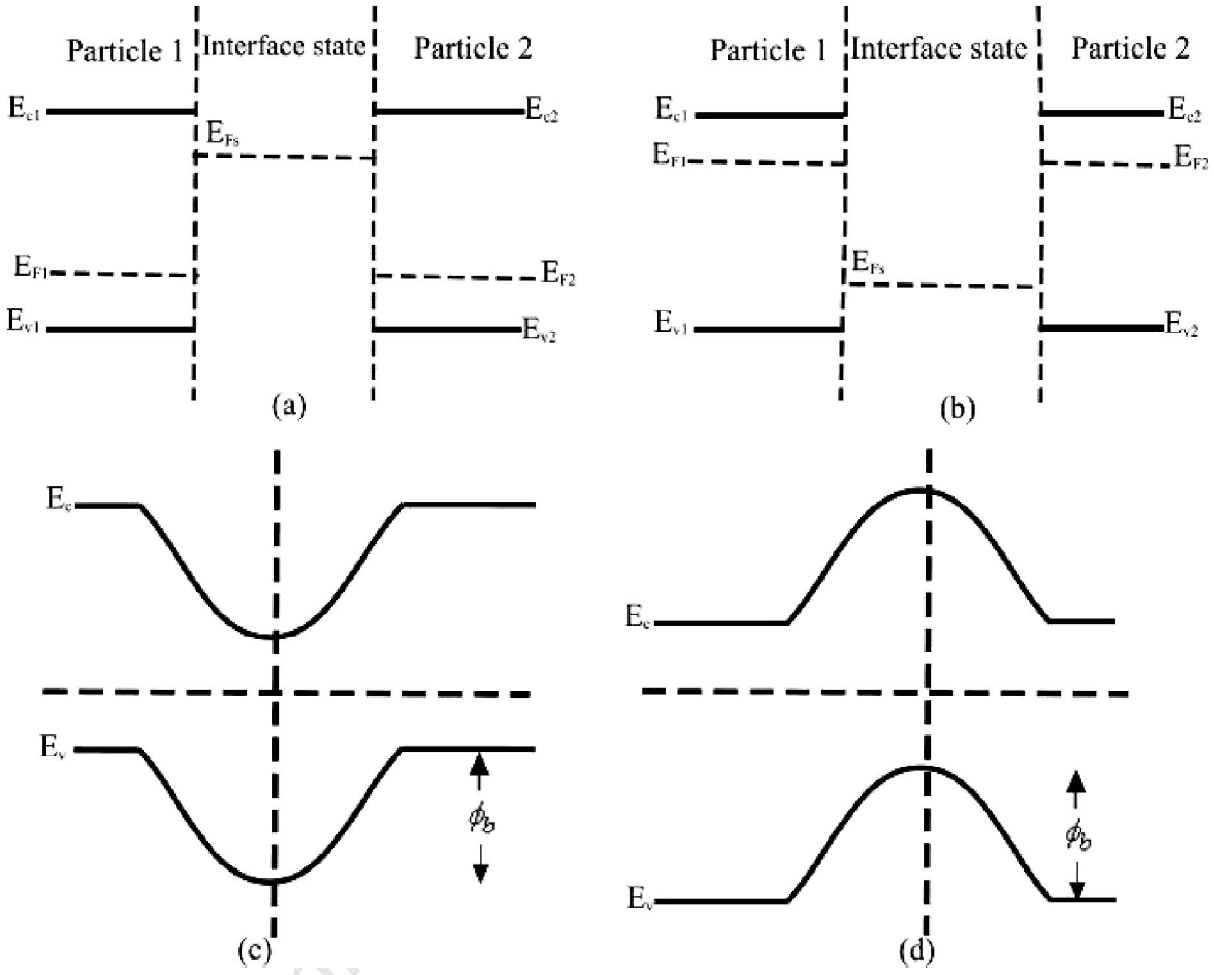

Fig. 6.6: Energy band diagram of identical particles in contact forming an interface with an effective Fermi level which is (a) higher and (b) lower than the common Fermi level of the particles before equilibrium. (c) and (d) show the band structure at equilibrium. E_{F1} and E_{F2} are the respective Fermi levels of particles 1 and 2. E_{v1}, E_{V2}, and E_{c1}, E_{c2} are the valence bands and conduction bands respectively. ϕ_b is the interface barrier height or depth of the potential well.

When the band bending is not so pronounced, as in the case where the Fermi level of the interface nearly matches that of the internal structure of the particles, the interface barrier becomes smaller but will still be symmetric with respect to transport of holes and electrons. This explanation tallies with the observation of the three common activation energies for charge transport.

Particles may be in contact in different orientations: face to face, and face to corner or face to edge. Based on this explanation, the activation energy of 15 K is associated with particles that make good contact with each other and in contact face to face as can be expected in a dense cluster. The activation energies of 450 K and 1200 K may be associated with other particle orientations which are more likely to be at cluster-cluster interfaces, i.e face to edge or face to corner.

Alternative explanations for the occurrence of the characteristic activation energies may be based on considering the distance between the particles. It is expected that the transitions across wide gaps are more difficult than those across narrow separations. Correspondingly, wide separations require higher activation energy than for particles in intimate contact. In this study, the interrelation between activation energy and separation between particles and clusters may be supported by the fact that for a particular particle loading, the activation energy for charge transport increases with temperature. At high temperatures, charge carriers have more energy to hop to more distant sites. The consideration of separation between the conducting segments becomes questionable if the dependence of activation energy on particle concentration is considered. It is logical to expect the separation between the particles to decrease with increase in particle loading. This would directly translate to a lowering of the activation energy for conduction. This is not the case for the silicon nanoparticle network under this study. The activation energies gradually increased with particle concentration. The contact between particles is poor in high particle loading samples, resulting in slightly higher barriers possibly due to wider separation between particles.

For the chemical vapour synthesised nanoparticles, the activation energy of 15 K is for particles making good contact, whereas the 180 K and 970 K represent activation of carrier transport between the clusters. The fourth activation energy cannot be resolved because these particles are heavily *p*-type and the electron trap cannot influence the hole transport. The differences in the size of activation energies between the two types of silicon nanoparticles are due to the different morphology of the particles. The effective area of contact between particles may be influenced by the surface structure of the particles with the result that rough particles such as those produced by milling would be expected to show different charge transport features from those seen in particles produced by CVS, which are smooth and have flat surfaces [9]

Essentially the observed temperature dependent conductivity behaviour of the silicon nanoparticle network is due to the transport of carriers across barriers. The observed apparent increase in carrier concentration with temperature should not be interpreted as carrier excitation across the band gap, but as the increase in concentration of mobile carriers. Carrier excitation across the band gap is not expected since the activation energies involved cannot exceed 0.2 eV which is only about 18% of the band gap of silicon. Thus, findings from the Hall effect experiment are consistent with conductance-temperature measurements which established the presence of barriers which limit the movement of charge carriers.

Accordingly, the conductivity of a printed silicon network is limited by charge transport across the interface between particles. The increase in apparent carrier concentration is indirect evidence for the thermal activation of carriers over barriers. The observed activation energies for conduction have been shown to be characteristic of the printed silicon. Samples printed from silicon nanoparticles of different morphology are characterised by different activation energies for charge transport.

Electrical conductivity is dependent on the carrier concentration and mobility of charge carriers. The temperature dependence of conductivity in turn depends on the combined temperature dependencies of carrier concentration and mobility. For bulk semiconductor materials, the mobility is generally expected to decrease with temperature due to the interaction of moving charge carriers with impurity centres in the case of doped materials [10], and scattering from lattice vibrations [11]. It has been shown that for the printed milled silicon nanoparticle network, the Hall effect mobility very slightly decreases with temperature. This can be taken as an indirect indication that the observed behaviour of the charge transport is not significantly due to the internal structure of the nanoparticles. It may be attributed to a dominant carrier scattering process occurring in the nanoparticle network. It can be speculated that the dominant scattering processes occur at the interface between the particles. The observed effective carrier concentration increases by up to six orders of magnitude over the extended temperature range of 15-345 K. However, this does not translate to an increase in carrier generation. In the nanoparticle system under study, there is no carrier generation. Carriers are injected from the electrodes and their transport is modulated by barriers in the system. The increase in the effective carrier concentration is due to an increase in the mobility of carriers across particle interfaces.

The measured Hall mobilities are comparable to those of highly resistive single crystalline silicon [12], yet the effective conductivity of the printed silicon is lower. Moreover, the measured carrier densities for the printed silicon composite show a significant reduction compared to the room temperature carrier densities of the parent bulk materials. The explanation to this lies in interpreting the Hall effect experimental data. The Hall effect experiment measured local mobilities in the particles. Subject to applied fields, charge carriers in a particle move at high average speed within a particle and are deflected in a direction transverse to their average drift velocity. These high mobilities are then measured by the Hall effect experiment. For a specific conductivity, the carrier concentration will then show as a low value. The measurement will then yield an apparent carrier concentration which is lower than the total carrier concentration. As mentioned before, this apparent carrier concentration correlates with the number of mobile carriers across the interface between particles and should not be considered as the total carrier concentration of the system.

7 Conclusion

This study has shown that the charge transport in a printed silicon nanoparticle system is unique. The charge transport is significantly limited by the properties of the interface between the particles making up the network and an electron trap. It is best described as single range hopping, as carriers move between particles and clusters, and percolation, as charge carriers map out preferred paths. Direct evidence of a hopping percolation transport model has been presented alongside a simple approach to resolve the activation energies for transport into their different components based on their origin.

The charge transport is characterised by the activation of carriers and the temperature dependence of conductivity essentially follows a superposition of pure Arrhenius behaviours. The *IV* characteristic of the printed silicon is marked by an unusually high ideality factor which is about three orders of magnitude higher than that expected of an ideal single junction diode. The high values of ideality factor arise from the scaling of applied absolute potential over many interfaces along the average conduction path. The ideality factor, which is proportional to the number of junctions in the percolation path, and the conductance show strong temperature dependence, which is characterised by the freeze-out of some percolation paths at low temperature.

Charge conduction in printed silicon samples produced using milled nanoparticles is characterised by four activation energies for conduction centred around 15 K, 450 K, 1200 K and 2300 K, whereas the conductivity of printed silicon from chemical vapour synthesized *p*-type nanoparticles could be described by the superposition of three Arrhenius dependencies corresponding to conduction paths with three activation energies of 15 K, 180 K and 970 K. The three low temperature activation energies for milled silicon samples were established by Hall effect measurements to be common for both hole and electron conduction. These can therefore be attributed to band bending at the interface between particles, since the interface barriers arising from the band bending are symmetric with respect to both electron and hole conduction. The highest activation energy of 2300 K was observed only for electron conduction and hence can be interpreted as arising from the activation of electrons from a trap state on the surface of the particles. In this light, the observed three activation energies in the printed chemical vapour synthesised samples, which were highly doped *p*-type, were all attributed to the barriers at the interface between particles since the conductivity is mainly dominated by hole conduction. The activation energy of 15 K originates from interface band bending of particles that are in contact face to face in both types of nanoparticles. The

activation energies of 450 K and 1200 K in layers produced from milled nanoparticles were slightly sensitive to particle loading and were associated with band bending at cluster-cluster interfaces. At these interfaces, particles can be in contact face to edge or face to corner. The sensitivity of these activation energies to particle loading is due to the fact that the contact between particles in a printed layer of high particle concentration is poor, possibly resulting in more distant separation between particles as particle loading increases. It then requires slightly higher activation energy to establish percolation paths through such interfaces.

Hall effect measurements have further shown that the Hall mobility inside the nanoparticles is very weakly dependent on temperature. The Hall mobility of electrons was higher than that of holes as expected due to differences in their effective masses. Holes and electrons showed similar temperature dependence of Hall mobility. This suggests the presence of a dominant scattering mechanism that affects holes and electrons in a similar way. This indirectly suggests that the charge transport is not significantly affected by the internal structure of the particles. As such, the observed increase in conductivity with temperature in the printed silicon nanoparticle system is attributed to an increase in the carrier hopping frequency over barriers. The increase in carrier transmission frequency shows as a positive temperature dependence of the apparent charge carrier concentration in the Hall effect data.

References

Chapter 1

[1] J.R. Sheats, Manufacturing and commercialization issues in organic electronics, *J. Mater. Res.* 19 1974 (2004).

[2] D.T. Britton and M. Härting, Printed nanoparticulate composites for silicon thick-film electronics, *Pure. Appl. Chem.*, **78**, 1723 - 1739 (2006).

[3] M. Härting, J. Zhang, D.R. Gamota, and D.T. Britton, Fully printed silicon field effect transistors, *Appl. Phys. Lett*. 94, 193509 (2009).

[4] D.T. Britton, E.A. Odo, G. Goro Gonfa, E.O. Jonah, and M. Härting, Size distribution and surface characteristics of silicon nanoparticles, *J. Appl. Cryst.*, **42**, 448 - 456 (2009).

[5] D.K. Rai, G. Beaucage, E.O. Jonah, D.T. Britton, S. Sukumaran, S. Chopra, G. Goro Gonfa, and M. Härting, Quantitative investigations of aggregate systems**,** *J. Chem. Phys.* 137, 044311 (2012).

[6] E.O. Jonah, D.T. Britton, P. Beaucage, D. K. Rai, G. Beaucage, B. Magunje, J. Ilavsky, M. R. Scriba, and M. Härting, Topological investigation of electronic silicon nanoparticulate aggregates using ultra-small-angle X-ray scattering, *J. Nanopart. Res.* **14,** 1249 (2012).

[7] N. F. Mott, and E. A. Davis, *Electronic processes in non-crystalline materials*, Clarendon, Oxford (1979).

[8] A. L. Efros and B. I. Shklovskii, Critical Behaviour of Conductivity and dielectric constant near the metal-non-metal transition threshold, *Phys. Stat. Sol*. B, **76**, 475 (1976).

[9] B. I. Shklovskii, and A. L. Efros, *Electronic properties of doped semiconductors*, Springer, Heidelberg (1984).

[10] I. Zvyagin, in *Charge transport in disordered materials with applications in electronics,* edited by S. D. Baranovski, John Wiley and Sons, Ltd, Chichester (2006).

[11] C. Tanase, E. J. Meijer, P. W. M. Blom, and D. M. de Leeuw, Unification of the Hole Transport in Polymeric Field-Effect Transistors and Light-Emitting Diodes, *Phys. Rev. Lett.* 91, 216601 (2003).

[12] I. P. Zvyagin, A percolation approach to the temperature and charge carrier concentration dependence of the hopping conductivity in organic materials, *Phys. Sta. Sol.* C 5, 3, 725 (2008).

[13] P. Sheng, B. Abeles, and Y. Arie, Hopping Conductivity in Granular Metals, *Phys. Rev. Lett.*, **31**, 44-47 (1973).

[14] Y. M. Strelniker, S. Havlin, R. Berkovits, and A. Frydman, Resistance distribution in the hopping percolation model, *Phys. Rev. E* 72, 016121-5 (2005).

[15] S. Kirkpatrick, Percolation and Conduction, *Rev. Mod. Phys.*, **45**, (5), 574 (1988).

[16] V. Ambegaokar, B. I. Halperin, and J. S. Langer**,** Hopping conductivity in disordered systems, *Phys. Rev. B* **4**, (8), 2612 (1976).

[17] D. Stauffer and A. Aharony, *Introduction to percolation theory*, Taylor & Francis, London (1992).

[18] M. Sahimi, *Applications of Percolation Theory*, Taylor and Francis (1994).

[19] G. Grimmett, *Percolation*, Springer (1989).

[20] M. Asif Khan, Michael S. Shur, John N. Kuznia, Q. Chen, J. Burm, and W. Schaff, Temperature activated conductance in GaN/AlGaN heterostructure field effect transistors operating at temperatures up to 300 ^{o}C, *Appl. Phys. Lett.* **66**, 1083 (1995).

Chapter 2

[1] C. R. Nave, *Abundances of the elements in the earth's crust*, Hyperphysics, Georgia State University, http://hyperphysics.phy-astr.gsu.edu/hbase/tables/elabund.html (Accessed on 2 July 2012).

[2] J. E. Kogel, N. C. Trivedi, J. M. Barker, *Industrial Minerals & Rocks: Commodities, Markets, and Uses*, Society for mining, metallurgy and exploration Inc. (SME). (2006).

[3] L. A. Corathers, U.S Geological Survey Minerals Yearbook-2009 (2011).

[4] D. A. Neamen, *Semiconductor Physics, Basic Principles*, 3rd Edition, McGraw-Hill, inc, New York (2003).

[5] H. P. Myers, *Introductory Solid State Physics*, Taylor and Francis Ltd, London (2002).

[6] C. Kittel, *Introduction to Solid State Physics*, 8th Edition, John Wiley and Sons Inc, New York (2005).

[7] C. A. Wert, R. M. Thomson, *Physics of Solids*, McGraw-Hill, Inc (1970).

[8] L. V. Azarov, *Introduction to solids*, McGraw-Hill, Inc (1960).

[9] P. Y. Yu, M. Cardona, *Fundaments of Semiconductors*, Spring-Verlag, Berlin (1999).

[10] S. M. Sze, K. NG. Kong, *Physics of Semiconductor Devices, 3rd Edition,*, John Wiley & Sons, Inc., Hoboken, New Jersey (2007).

[11] www.siliconfareast.com/lattice_constants.htm (Accessed on 12 July 2011).

[12] K. Santiran, *Basic Electronics: Devices, Circuits and IT Fundamentals*, PrenticeHall of India (2004).

[13] S. T. Pantelides, Defects in Amorphous Silicon: A New Perspective, *Phys. Rev. Lett.* **57**, 2979 (1986).

[14] H. J. Quiesser, E. H. Eugene, Defects in Semiconductors: Some Fatal, Some Vital, *Science*. **281**, 945 (1998).

[15] U. K. Mishra, J. Singh, *Semiconductor device Physics and designs*, Springer (2008).

[16] H. J Leamy, Charge collection scanning electron microscopy, *J. Appl. Phys.* **53** R51 (1982).

[17] C. R. M. Grovener, Grain boundaries in semiconductors, *J. Phys. C: sol. Stat. Phys.* **18**, 4079 (1985).

[18] M. R. Scriba, C. Arendse, M. Härting, D. T. Britton, Hot-wire synthesis of Si nanoparticles, *Thin sol. Films*, **56**, 844 (2008).

[19] G. Schön, U. Simon, A Fascinating New Field in Colloid Science: Small Ligand Stabilized Metal Clusters and Possible Applications in Microelectronics"; Part I: "State of the Art", *Colloid Polym. Sci*, **273**, 101 (1995).

[20] U. Simon, Charge transport in nanoparticle arrangements, *Adv. Mater*., **10**, 17 (1998).

[21] J. C. Love, L. A. Estroff, J. K. Kriebel, R. G. Nuzzo, and G. M. Whitesides, Self-assembled monolayers of thiolates on metals as a form of nanotechnology, *Chem. Rev.*, 105, **4**, 1103 (2005).

[22] F. E. Kruis, A. Goosens, and H. Fissan, Synthesis of semiconducting nanoparticles, *J. Aerosol Sci*, **27**, S165 (1996).

[23] R. Kelsall, I. Hamley, and M. Geoghegan, *Nanoscale science and technology*, John Wiley & Sons Ltd (2005).

[24] R. Yu, L. Chen, Q Liu, J. Lin, K-L. Tan, S. C. Ng, H. S. O. Chan, G. Q. Xu, and T. S. A. Hor, Platinum deposition on carbon nanotubes via chemical modification, *Chem. Mater.*, 10, 718 (1998).

[25] K. Tonokura, T. Murasaki, and M. Koshi, Formation mechanism of hydrogenated silicon clusters during thermal decomposition of disilane, *J. Phys. Chem. B*, **106**, 555 (2002).

[26] V. G. Kravets, C. Meier, D. Konjhodzic, A. Lorke, and H. Wiggers, Infrared properties of silicon nanoparticles, *J. Appl. Phys.*, **97**, (8), 084306 (2005).

[27] D.T. Britton and M. Härting, Printed nanoparticulate composites for silicon thick-film electronics, *Pure. Appl. Chem.*, **78**, 1723 - 1739 (2006).

[28] D. T. Britton, and M. Härting, Method of producing stable oxygen terminated semiconducting nanoparticles, *Patent cooperation treaty application*, WO 2009/125370 A1.

[29] J. E. Kogel, and N. C. Trivedi, *Industrial Minerals and rocks: Commodities, Markets and Uses*, SME (2006).

[30] M. Härting, G. G. Gonfa, E. A. Odo, M. R. Scriba, B. Magunje, M. J. van Staden and D. T. Britton, (Submitted for publication).

[31] F. Rinaldi, *Basics of molecular beam epitaxy (mbe)*, Universitat ULM, Annual research report (2002).

[32] A. A. Onischuck, A. I. Levykin, V. P. Strunin, M. A. Ushakova, R. I. Samolova, K. K. Sabelfeld, and V. N. Panfilov, Aerosol formation under heterogeneous/homogeneous thermal decomposition of silane: experiment and numerical modelling, *J. Aerosol Sci*., **31**, (8), 879 (2000).

[33] G. Glaspell, V. Abdelsayed, K. M. Saoud, and M. S. El-Shall, Vapor-Phase synthesis of metallic and intermetallic nanoparticles and nanowires: Magnetic and catalytic properties, *Pure Appl. Chem.*, **78**, (9), 1667 (2006).

[34] M. S. El-Shall, A. S. Edelstein, *Nanomaterials: Synthesis, Properties and Applications*, Institute of Physics, Philadelphia (1996).

[35] C. C. Striemer, R. Krishnan, P. M. Fauchet, Fabrication of nanostructure array by reactive ion etching and naosphere lithography, *J. Minerals, Metals, and Mater. Soc*., **50**, 20 (2004).

[36] G. G. Kirpilenko, V. D. frolov, E. V. Zavedeev, S. M. Primenov, V. I Konov, E. Y. Shelukhin, and E. N. Loubnin, Synthesis, characterisation and nanostructuring of (a-

C:H):Si and (a-C:H):Si:metal films, *Diamond and Related Mater.*, 15, (4-8), 1147 (2006).

[37] H. Li, R. H. Franken, R. L. Stolk, C. H. M. van der Werf, J. K. Rath, and R. E. I. Schropp, Controlling the quality of nanocrystalline silicon made by hot-wire chemical vapour deposition by using a reverse H_2 profiling technique, *J. Non-Cryst. Sol.*, **19**, 2087 (2008).

[38] M. J. Bogan, W. H. Benner, S. P. Han-Riege, H. N. Chapman, and M. Frank, Aerosol Sample Preparation Methods for X-ray Diffractive Imaging: Size-selected Spherical Nanoparticles on Silicon Nitride Foils, *Aerosol Sci.*, **38**, 1119 (2007).

[39] A. T. Heitsch, V. A. Akhavan, and B. A. Korgel, Rapid SFLS Synthesis of Si **...** with In Situ Alkyl-Amine Passivation, *Chem. Mater.*, **23**, 2697 (2011).

[40] T. Shimoda, Y. Matsuki, M. Furusawa, T. Aoki, I Yudasaka, H. Tanaka, H. Iwasawa, D. Wang, M. Miyasaka, and Y. Takenchi, Solution-processed silicon films and transistors, *Nature*, **440**, 783 (2006).

[41] R. A. Bley, S. M. Kauzlarich, A low-temperature solution phase route for the synthesis of silicon nanoclusters, *J. Am. Chem. Soc.*, **118**, 12461, 11016 (1996).

[42] C.-S. Yang, R. A. Bley, S. M. Kauzlarich, H. W. H. Lee, G. R. Delgado, Synthesis of alkyl-terminated silicon nanoclusters by a solution route*J. Am. Chem.* Soc., **121**, 5191 (1999).

[43] D. Neiner, H Wei Chiu, and S. M. Kauzlarich, Low-temperature solution route to macroscopic amounts of hydrogen terminated silicon nanoparticles, *J. Am. Chem. Soc.*, **128**, 11016 (2006).

[44] R. K. Baldwin, K. A. Pettigrew, J. C. Garno, P. P. Power, G. Liu, and S. M. Kauzlarich, Solution reduction synthesis of surface stabilized silicon nanoparticles, *J. Am. Chem. Soc.*, **124**, (7), 1150 (2002).

[45] J. L. Heinrich, C. L. Curtis, G. M. Credo, K. L. Kavanagh, M. J. Sailor, Luminescent colloidal silicon suspensions from porous silicon, *Science,* **255**, 66 (1992).

[46] S. Berhane, S. M. Kauzlarich, K. Nishimura, R. L Smith, J. E. Davis, H. W. H.Lee, M. L. S. Olson, L. L. Chase, Investigation of Colloidal Si Prepared from Porous Silicon, In *Mater. Res. Soc. Symp. Proc.*, San Francisco, 99 (1993).

[47] R.A. Bley, S.M. Kauzlarich, in: J.H. Fendler (Ed.), Nanoparticles in Solids and Solutions. Preparation, Characterization and Applications, VCH Publishers, New York (1997).

[48] R. A. Bley, S. M. Kauzlarich, J. E. Davis and H. W. H. Lee, Characterization of Silicon Nanoparticles Prepared from Porous Silicon, *Chem. Mater.*, **8**, 1881-1888 (1996).

[49] R. A. Bley, and S. M. Kauzlarich, A Low-Temperature Solution Phase Route for the Synthesis of Silicon Nanoclusters, *J. Am. Chem. Soc.*, **118**, 12461 (1996).

[50] R. A. Bley, S. M. Kauzlarich, *Synthesis of Silicon Nanoclusters*; Fendler, J. H., Ed.; Wiley-VCH: Weinheim, Germany (1998).

[51] J. D. Holmes, K. J. Ziegler, R. C. Doty, L. E. Pell, K. P. Johnston, B. A. Korgel, Highly Luminescent Silicon Nanocrystals with Discrete Optical Transitions, *J. Am. Chem. Soc.*, 123, (16), 3743 (2001).

[52] C. Steinhagen, V. A. Akhavan, B. W. Goodfellow, M. G. Panthani, J. T. Harris, V. C. Holmberg, and B. A. Korgel, Solution-liquid-solid synthesis of $CuInSe_2$ nanowires and their implementation in photovoltaic devices, *Appl. Mater. Interfaces*, **3**, 1781 (2011).

[53] A. M. Chockla, J. T. Harris, and B. A. Korgel, Size Controlled Growth of Germanium Nanorods and Nanowires by Solution Pyrolysis Directly on a Substrate, *Chem. Mater.*, **23**, 1964 (2011).

[54] J Marques-Hueso, R Abargues, J Canet-Ferrer, J L Valdes, J Martinez-Pastor, Resist-based silver nanocomposites synthesized by lithographic methods, *Microelectronic Engineering* **87**, (5-8), 1147 (2010).

[55] R. Abargues, K. Abderrfi, E. Pedrueza, R. Gradess, J. Marques-Hueso, J. L. Valdés, E. Jiménez, and J. P. Martinez-Pastor, In Situ synthesis of Ag and Au nanoparticles in different polymer thin films, *New J. Chem.*, **33**, (8), 1720 (2009).

[56] M. Ben Rabha., M. Saadoun, M. F. Boujmil, B. Bessaïs, H. Ezzaouia, and R. Bennaceur, Application of the chemical vapor-etching in polycrystalline silicon solar cells, *Appl. Surf. Sci.*, **252**, (2), 488 (2005).

[57] J. Valenta, A. Fučíková, I. Pelant, K. Kusová, K. Dohnalová, A. Aleknavičius, O. Cibulka, A. Fojtik, and G. Kada, On the origin of the fast photoluminescence band in small silicon nanoparticles, *New J. Phys.*, **10**, 1 (2008).

[58] C. C. Koch, *Dekkar Encyclopedia of Nanoscience and nanotechnology*, Marcel Dekkar, New York (2004).

[59] M. S. El-Eskandarany, *Mechanical Alloying for Fabrication of Advanced Engineering Materials*, William Andrew Publisher, New York (2001).

[60] P. R. Soni, *Mechanical Alloying*, Cambridge international Publishing, Cambridge (2001).

[61] H. W. Lau, O. K. Tan, B. C. Ooi, Y. Liu, T. P. Chen, and D. Lu, Characteristics of mechanically milled silicon nanocrystals embedded in TEOS thin films, *J. Cryst. Growth*, **288**, (1,2), 92 (2006).

[62] P. Unifantowicz, S. Vaucher, M. Lewandowska, and K. J. Karzydlowski, Structural changes of silicon upon high-energy milling investigated by Raman spectroscopy, *J. Phys.: Condensed matter*, **20**, 025205 (2008).

[63] I. Umezu, H. Minani, H. Senoo, and A. Sugimura, Structural changes of silicon upon high-energy milling investigated by Raman spectroscopy, *J. Phys.: Conference Series*, **59**, 392 (2007).

[64] T. Makino, M. Inada, K. Yoshida, I. Umezu, and A. Sugimura, Structural and optical properties of silicon nanoparticles prepared by pulsed laser ablation in hydrogen background gas, *Appl. Phys. A*, 79, 13911393 (2004).

[65] N. G. Semaltianos, S. Logothetidis, W. Perrie, S. Romani, R. J. Potter, S. P. Edwardson, P. French, M. Sharp, G. Dearden, K. G. Watkins, Silicon nanoparticles generated by femtosecond laser ablation in a liquid environment, *J. Nanopart. Res.*, Springer Science+Business Media B. V (2009).

[66] J. W. Mayer, S. S. Lau, *Electronic Material Science*, MacMillan (1990).

[67] B. van Zeghbroeck, *Principles of semiconductor devices and heterojunctions*, PrecticeHall (2009).

[68] R. Mulliken, *Spectroscopy, Molecular Orbitals and Chemical Bonding*, Nobel Lecture (1966).

[69] H. Unlu, A Thermodynamic Model for Determining Pressure and Temperature Effects on the Bandgap Energies and other Properties of some Semiconductors, *Solid State Electronics*, **35**, 1343 (1992).

[70] B. M. Askerov, *Electron transport phenomena in semiconductors*, World Scientific Publishing Co. Pte, Ltd., Singapore (1994).

[71] J. Singleton, *Band Theory and Electronic Properties of Solids*, Oxford University Press, New York (2001).

[72] K. Seeger, *Semiconductor Physics. An Introduction, 6th Edition*, Springer, Berlin (1997).

[73] B. G. Streetman, *Solid State Electronic Devices, 4th Edition*, Prentice Hall, New Jersey (1995).

[74] M. A. Pinault, J. Barjon, T. Kocinieski, F. Jomard, J. Chevallier, The n-type doping of diamond: present status and pending questions, *Physica B*, **51**, 401 (2007).

[75] D. C. Look, D. C. Reynolds, C. W. Litton, R. L. Jones, D. B. Eason, G. Cantwell, Characterization of homoepitaxial *p*-type ZnO grown by molecular beam epitaxy, *Appl. Phys. Lett.*, **81**, 1830 (2002).

[76] R. Dalvern, *Introduction to Applied Solid State Physics, 2nd Edition*, Plenum Press, New York (1990).

[77] N.W. Ashcroft and N.D. Mermin, Solid State Physics, Holt, Rinehart and Winston, New York (1976)

[78] D.A. Fraser, *The Physics of Semiconductor Devices*, Oxford University Press, Oxford (1977).

[79] R. Pierret, *Semiconductor Device Fundamentals*, Addison Wesley (1996).

Chapter 3

[1] N. F. Mott, J. Non-crystalline solids, **1**, 1 (1968): Conduction in non-crystalline materials, Clarendon Press, Oxford, 2nd ed (1993).

[2] N.F. Mott and E.A. Davis, *Electronic processes in non-crystalline materials*, Clarendon, Oxford (1979).

[3] I. Zvyagin, *Charge transport via delocalized states in disordered materials: Charge transport in disordered materials with applications in electronics*, S.D. Baranovski, (ed), John Wiley and sons, Ltd, Chichester (2006).

[4] N. Mott, Electrons in non-crystalline materials. The last twenty five years, *Cont. Phys.*, **26**, 203 (1985).

[5] M. A. Kastner, Artificial Atoms, *Phys. Today*, **46**, 24 (1993).

[6] D. Yu, C. wang, B. L. Wehrenberg, P. Guyot-Sionnest, Variable range hopping conduction in semiconductor nanocrystal solids, *Phys. Rev. Lett*, **92**, (21), 216802 (2003).

[7] A. Z-Khosousi, A-A. Dhirani, Charge Transport in Nanoparticle Assemblies, *Chem. Rev.*, **108**, 4072 (2008).

[8] M. Musakov, B. Tadic, Modeling collective charge transport in nanoparticle assemblies, *J. Phys.: Condens. Matter*, **22**, 163201 (2010).

[9] D. Yu, C. Wang, P. Guyot-Sionnest, *n*-Type conducting CdSe nanocrystal solids, *Sci.*, **300**, 1277 (2003).

[10] G. C. Psarras, Charge transport properties in carbon black/polymer composites, *J. Polymer Sci.* B: Polymer Physics, **45**, (18), 2535 (2007).

[11] M. Khissi, M. El Hasnaoui, J. Belattar, M. P. F. Graça, M. E. Achour, L. C. Costa, DC electrical conductivity studies on copolymer/carbon black composites, *J. Mater. Environ. Sci.*, **2**, (3), 281 (2011).

[12] M. P. J. van Staveren, H. B. Brom, L. J. de Jong, Metal-cluster compounds and universal features of the hopping conductivity of solids, *Phys. Rep.*, **208**, 1 (1991).

[13] B. Abeles, P. Sheng, M. D. Couts, Y. Arie, Structural and electrical properties of granular metal films, *Adv. Phys.*, **24**, 407 (1975).

[14] J. E. Morris, T. J. Coutts, Electrical conduction in discontinuous metal films, *Thin Solid Films*, **47**, 3 (1972).

[15] S. Komarneni, Nanocomposites, *J. Mater. Chem.*, **2**, (12), 1219 (1992).

[16] N. Salahiddin, A. Moet, A. Hiltner, E. Baer, Nanoscale highly filled epoxy nanocomposite, *Eurpean Polymer Journal*, **38**, 1477 (2002).

[17] C. Sanchez, F. Ribot, Design of Hybrid Organic-Inorganic Materials Synthesized Via Sol-Gel Chemistry, *New J. Chem.*, **18**, 1007 (1994).

[18] P. M. Ayajan, L. S. Shadler, P. V. Braun, *Nanocomposite Science and Technology*, Wiley ISBN 3527303596 (2003).

[19] F. Lux, Models proposed to explain the electrical conductivity of mixtures made of conductive and insulating materials, *J. Mater Sci*, **28**, 285 (1993).

[20] M. Carmona, C. Mouney, Temperature-dependent resistivity and conduction mechanism in carbon particle-filled polymers, *J. Mater Sci*, **27**, 1322 (1992).

[21] D.Vanmaekelbergh, P. Liljeroth, Electron-conducting quantum dot solids: novel materials based on colloidal semiconductor nanocrystals, *Chem. Soc. Re*v, 34, 299 (2005).

[22] E. H. Rhoderick, and R. H. Williams, *Metal-Semiconductor Contacts*, 2nd Ed., Clarendon, Oxford (1988).

[23] W. B. Nottingham, *Thermionic Emission*, Tech. Rep. 323, Research Lab of Electronics, Masschusetts Institute of Technology, Cambridge, Masschusetts (1956).

[24] H. A. Bethe, *"Theory of the Boundary Layer of Crystal Rectifiers,"* MTRadiat. Lab. Rep., 43-12 (1942).

[25] P. Sheng, Hopping Conductivity in Granular Metals, *Phys. Rev. Lett.*, **31**, 44 (1973).

[26] S. M. Sze, K. NG. Kong, *Physics of Semiconductor Devices, 3rd Edition,*, John Wiley & Sons, Inc., Hoboken, New Jersey (2007).

[27] J. G. Simons, Potential Barriers and Emission-Limited Current Flow Between Closely Spaced Parallel Metal Electrodes, *J. Appl. Phys.*, **35**, 2472 (1964).

[28] C. B. Duke, in Tunneling Phenomena in Solids; E. Burstein, S. Landqvist, Eds, Plenum, New York (1992).

[29] C. Y. Chang and S. M. Sze, Carrier transport across metal-semiconductor barriers, *Solid-State Electron.*, 13,727 (1970).

[30] F. A. Padovani and R. Stratton, Field and thermionic-field emission in Schottky barriers, *Solid-state Electron.*, 9, 695 (1966).

[31] P. Sheng, Fluctuation-induced tunnelling conduction in disordered materials, *Phys. Rev. B*, 21, (6) (1980).

[32] T.C. Choy, *Effective Medium Theory: Principles and applications,* Oxford University Press, Oxford (1999).

[33] B.I. Shklovskii, A.L. Efros, *Electronic properties of doped semiconductors,* Springer, Berlin, New York (1984).

[34] S. Kirkpartrick, Percolation and Conduction, *Rev. Mod. Phys*, **45,** (4), 574 (1993).

[35] P. Sheng, E. K. Sichel and J.L. Gittleman, Fluctuation-Induced Tunneling Conduction in Carbon-Polyvinylchloride Composites, *Phys. Rev. Lett,* **40**, 18 (1978)

[36] S. Shekar, V. Prasad, S.V. Subramanyam, Transport properties of conducting amorphous carbon-Poly (vinyl Chloride) composite, *J. Carbon.*, **44**, 334 (2006).

[37] P. Sheng: *Nanophase Materials*, eds. G. C. Hadjipanayis and R. W. Siegel (Kluwer Academic, Dordrecht), 381 (1994).

[38] Y.H. Lin, S.P. Chin and J.J. Lin, Thermal fluctuation-induced tunneling conduction through metal nanowire contacts, *Nanotechnology* **19**, 365201 (2008).

[39] H. Xie and P. Sheng, Fluctuation-induced tunneling conduction through nanoconstrictions, *Phys. Rev. B*, 79, 165419 (2009).

[40] I. Balberg, Tunnelling and non-universal conductivity in composite materials, *Phys. Rev. Lett.,* 59 (12) (1987).

[41] G.C. McGonigal, D. J. Thomson, J.G. Shaw, and H.C. Card, Electronic transport at grain boundaries in silicon, *Phys. Rev.* B, 28 (10) 5908 (1983).

[42] S.A, Kolosov, Yu. V. Klevkov, and A.F. Plotnikov, Amorphous, vitreous, and porous semiconductors, *Semiconductors,* **38** (4) 455 (2004).

[43] Y.S. Tsuo, J.B. Milstein, and T. Surek, Grain Boundary Structures and Properties in Polycrystalline Silicon, Elsevier Science Publishing Company, Inc. 155 (1982).

[44] C.R.M. Grovenor, Grain boundaries in semiconductors, *J. Phys. C: Solid State Phys.*, **18**, 4079 (1985).

[45] G. Baccarani, M. Impronta, B. Ricco, I-V characteristics of polycrystalline silicon resistors, *Revue De Physique, Appliquee,* **13**, 777 (1978).

[46] G. Baccaranni, B. Ricco, and G. Spadini, Transport properties of polycrystalline silicon films, *J Appl. Phys.*, 49, 5565 (1978).

[47] John Y. W. Seto, The electrical properties of polycrystalline silicon films, *J. Appl. Phys.* **46**, 5247 (1975).

[48] H. Ikeda, Evaluation of grain boundary trap states in polycrystalline–silicon thin-film transistors by mobility and capacitance measurements, *J. Appl. Phys.* **91** (7) (2002).

[49] C.R Crowell and S. M. Sze, Current transport in metal-semiconductor barriers, *Solid-State Electron Devices*, 9, 1035 (1966).

[50] C.H. Seager and G.E. Pike, Grain boundary states and varistor behaviour in silicon bicrystals, *App. Phys. Lett.* **35**, 709 (1979).

[51] O. Dorlanne, and M. Tao, *High Tech. Ceramics, ed. P. Vincezini, Elsevier, Amsterdam,* 1809 (1987).

[52] M. S. Castro and C.M. Aldao, Effects of thermal treatments on the conductance of tin oxide, *J. Europ. Ceramic Society*, **17**, 1533 (1997).

[53] J. Martinez, and J. Piqueras, On the mobility of polycrystalline semiconductors, *Solid State Electron*,. **23,** 297 (1980).

[54] C.Y. Lu, C.Y.Y. Lu, and C.S. Wang *Solid State Electron*, **23**, 297 (1980).

[55] M.L. Tarng, Carrier transport in oxygen-rich polycrystalline-silicon films, *J. Appl. Phys.*, **49**, 4069 (1978).

[56] K. Kim, Visible light emissions and single-electron tunnelling from silicon quantum dots embedded in Si-rich SiO_2 deposited in plasma phase, *Phys. Rev.* B **57**, 13072 (1998).

[57] W. Siegel, G. Kuhnel, and E. Zigler 1981, Electrical properties of grain boundaries in n-type and p-type GaP, *Phys. Stat. Sol. a* 64 249 (1981).

[58] S.R. Elliot, *The Physics of amorphous materials,* John Wiley& Sons, Inc.,New York (1990).

[59] B.I. Shkloviski and A.L. Efros, *Electronic properties of semiconductors,* Springer, Heidelberg (1984).

[60] A. Miller and E. Abrahams, Impurity Conduction at Low Concentrations, *Phys. Rev,* **120**,745 (1960).

[61] W. Fuhs, *Hydrogenated amorphous silicon material properties and device applications* in: *Charge transport in disordered solids with applications in electronics,* S.D. Baranoviski, (ed), John Wile & Sons, Ltd, Chichester (2006).

[62] S. Baranovski, O. Rubel,*Description of charge transport in amorphous semiconductors* in: *Charge transport in disordered solids with applications in electronics,* S.D. Baranovski, (ed), John Wile & Sons, Ltd, Chichester (2006).

[63] A.L. Efros and B.I. Shklovskii, . Coulomb Gap and Low-Temperature Conductivity of Disordered Systems, *J. Phys. C,***8**, L49 (1975).

[64] L. Nicolais, G. Carotenuto, *Metal-Polymer Nanocomposites,* John Wiley & Sons, Inc. (2005).

[65] S.D. Baranovski, A.L. Efros, B.L. Gelmont, and B.I. Shklovskii, Coulomb gap in disordered systems : computer simulation, *J. Phys. C,* **12**, 1023 (1979).

[66] S. Kirkpatrik, Percolation and Conduction, *Rev. Mod. Phys*., **45**, (5) 574 (1973).

[67] V. Ambegaokar, B. I. Halperin and J. S. Langer, Hopping Conductivity in disoredered Systems, *Phys. Rev.* B, **4**, (8) 2612 (1972).

[68] I. Stavaache, Charge photo-carrier transport from silicon nanocrystals embedded in SiO2-based multilayer structures, *Dig. J. Nanomat. Bio.* **6** (3) 1073 (2011).

[69] M. H. Ali, A. Abo-Hasheu, Percolation concept and the electrical conductivity of carbon black-polymer composites 2: Non-crystallisable chloroprene rubber mixed with HAF carbon black, *J. Mat. Proc. Tech.* **68** 168 (1997).

[70] N. Tessler, Y. Preezant, N. Rappaport and Y. Roichman, Charge Transport in Disordered Organic Materials and its Relevance to Thin Film Devices – a Tutorial Review, *Adv. Mater*. **21** 2741 (2009).

[71] M. Sahimi: *Applications of Percolation Theory*, Taylor & Francis, London (1994).

[72] A. Bunde and S.Havlin (eds.), *Fractals and Disordered Systems*, 2nd Edition, Springer Verlag, Heidelberg (1996).

[73] D. Stauffer and A. Aharony, *Introduction to Percolation Theory*, Taylor & Francis, London (1992).

[74] A. L. Efros and B. I. Shklovskii, Critical Behaviour of Conductivity, *Phys. Stat. Sol. B* **76** 475 (1976).

[75] H. E. Stanley, *Introduction to phase transitions and Critical Phenomena*, Oxford:OUP (1971).

[76] *Phase Transitions and Critical Phenomena*, Edited by C. Domb and M. S. Green, New York (1972).

[77] J. Feder, *Fractals*, New York: Plenum Press (1988).

[78] T. Vicsek, *Fractal Growth Phenomena*, Singapore: World Scientific (1989).

[79] B. Ballobas and O. Riordan, *Percolation*, Cambridge University Press (2006).

[80] G. Paul, S. V. Buldyrev, N. V. Dokholyan, S. Havlin, P. R. King, Y. Lee, H. E. Stanley, Dependence of conductance on percolation backbone mass, *Phys. Rev. E* **61** (4) (2000).

[81] R. Blumenfeld, A. Aharony, Nonlinear resistor fractal networks, topological distances, singly connected bonds and fluctuations, *J. Phys. A: Math. Gen*. **18** L443 (1985).

[82] T. Nakayama, K. Yakubo, Dynamical Properties of Fractal Networks: Scaling, Numerical Simulations, and Physical Realizations *Rev. Mod. Phys*. **66** (2) 381 (1994).

[83] O. Bleibaum, H. Böttger and V. V. Bryksin, Random-resistor network description for hopping transport in the presence of Hubbard interaction, *J. Phys.: Condens. Matter,* 15 1719 (2003).

[84] B. I. Shklovskii, Hopping conduction in semiconductor films, *Phys. Lett*. **51**A 289 (1975).

[85] M. Vissenberg, M. Maters, Theory of the field-effect mobility in amorphous organic transistors, *Phys. Rev. B* **57** 12964 (1998).

[86] M. Vissenberg, *Opto-Electronic Properties of Disordered Organic Semiconductors*, PhD Thesis, Universiteit Leiden, Leiden (1999).

[87] C. H. Lin, G. Y. Wu, Percolation calculation with non-nearest neighbor hopping of hopping resistances for granular metals, *Thin Solid Films* **397** 280 (2001).

[88] A. C. Beer, *Galvanomagnetic Effects in Semiconductors. Solid St. Phys. Suppl. 4* ed F. Seitz and D. Turnbull, New York: Academic (1963).

[89] E. H. Putley, *The Hall Effect and Related Phenomena*, London: Butterworth (1960).

[90] J. W. Orton and M. J. Powell, Hall effect in semiconductor powders, *Phil. Mag.* B, **38**, 491 (1978).

[91] L. J. van der Pauw, A method of measuring specific resistivity and Hall effect of discs of arbitrary shape, *Philips Res Reports,***13**,1 (1958).

[92] K. Seeger, *Semiconductor Physics, An Introduction*, 6th edition, Springer-Verlag, Berlin (1997).

[93] R. A. Smith, *Semiconductors*, 2nd Ed., Cambridge University Press, London (1979).

[94] J. W. Orton, and M. J. Powell, The Hall effect in polycrystalline and powdered semiconductors, *Rep. Prog. Phys.*, 43 (1990).

[95] R. Zallen and H. Scher, Percolation on a Continuum and the Localization-Delocalization Transition in Amorphous Semiconductors, *Phys. Rev.* B, **4**, 4471(1971).

[96] I**.** Webman**,** J. Jortner, and M. H. Cohen, Numerical simulation of continuous percolation conductivity, *Phys. Rev.* B, **14**, 4737 (1976).

[97] A . S. Skal and B. I. Shklovskii, Topology of the infinite cluster of the percolation theory and its relationship to the theory of hopping conduction, *Sov. Phys.-Semicond.*, **8**, 1029 (1975).

[98] M.E. Levinshtein, B.I. Shklovskii, M.S. Shur, A.L. Efros, The relation between the critical exponents of percolation theory, Zh. Eksp. Theor. Fiz. 69, 386 (1975) - Engl. transl.: Sov. Phys.-JETP **42**, 197 (1975).

[99] C. J. Adkins, Effective-medium theory of conductivity and Hall effect in two dimensions, *J. Phys. C: Solid St. Phys.*, **12**, 3389 (1979).

[100] M. Grünewald, P. Thomas and D. Würtz, The sign anomaly of the Hall effect in amorphous tetrahedrally bonded semiconductors: a chemical-bond orbital approach *J. Phys. C: Solid State Phys.*, **14**, 4083 (1981).

Chapter 4

[1] M.R. Scriba , D.T. Britton , C. Arendse, M.J. van Staden, M. Härting, Composition and Crystallinity of Silicon Nanoparticles Synthesized by Hot Wire Thermal Catalytic Pyrolysis at Different Pressures, *Thin Solid Films* 517, 3484–3487 (2009).

[2] D. T. Britton, in *Plastic Electronics Asia* (2008).

[3] R. H. Leach, and R. J. Pierce, *The printing ink manual*, Springer, Netherlands (2007).

[4] N. R. Mathe, *The Rheology of Silicon Nanoparticle Inks*, MSc Thesis, University of Cape Town (2010).

[5] R. G. Loasby and P. J. Holmes: *"Development of Thick Film Technology", in Handbook of Thick Film Technology*, K. E. G. Pitt, Electrochemical Publications Ltd, Brittish Isles (2005).

[6] A. Hobby, *"Printing thick film hybrids", in Handbook of thick film technology*, K. E. G. Pitt, Electrochemical Publications Ltd, British Isles (2005).

[7] LakeShore user manual: *Lake Shore 7500/9500 Series Hall Series Hall System User's manual*. www.lakeshore.com.

[8] A. Visioli, *Practical PID control*, Springer-Verlag (2006).

[9] LakeShore user manual: *User's manual, model 340 temperature controller*, www.lakeshore.com.

[10] D. C. Look, C. E. Stutz, J. R. Sizelove, and K. R. Evans, On Hall scattering factors for holes in GaAs, *J. Appl. Phys.*, **80**, 1913 (1996).

[11] R. Chwang, B.J. Smith, and C.R. Crowell, Contact size effects on the van der Pauw method for resistivity and Hall coefficient measurement, *Solid-State Electron.*, **17**, 1217 (1974).

Chapter 5

[1] D. T. Britton, E. A. Odo, G. Goro Gonfa, E. O. Jonah and M. Härting, Size distribution and surface characteristics of silicon nanoparticles, *J. Appl. Cryst.* **42** (2009).

[2] D. T. Britton, M. Härting, Printed nanoparticulate composites for silicon thick-film electronics, *Pure Appl. Chem.*, **78**, (9), 17231739 (2006).

[3] M.R. Scriba, D.T. Britton , C. Arendse, M.J. van Staden, M. Härting, Composition and Crystallinity of Silicon Nanoparticles Synthesized by Hot Wire Thermal Catalytic Pyrolysis at Different Pressures *Thin Solid Films* 517, 3484–3487 (2009).

[4] G. G. Gonfa, *Hall Effect in Printed Nanoparticulate Silicon Networks*, PhD Thesis, University of Cape Town (2009).

[5] M. Shibata, S. Asahina, T. Negishi, *Proc. 8 APEM, Kanazawa* (2004).

[6] W. Hauffe, Electron microscopy, **2**, *EUREM 92, Granada*, Spain (1992).

[7] G. D. J. Smit, S. Rogge, and T. M. Klapwijk , Conductance distribution in nanometer-sized semiconductor devices due to dopant statistics, *Appl. Phys. Lett.*, **81**, 3852 (2002).

[8] W. Monch, On the physics of metal-semiconductor interfaces, *Rep. Prog. Phys.*, **53**, 221 (1990).

[9] A. Rose, Space-Charge-Limited Currents in Solids, *Phys. Rev.*, **97**, 1538 (1955).

[10] J. Lindemuth, B. Dodrill, J. Meyer, and I. Vurgaftman, *Extended abstract, CS-MAX conference, San Jose*, CA, IOP publishing Ltd (2002).

[11] J. R. Meyer, C. A. Hoffman, F. J. Bartoli, D. J. Arnold, S. Sivananthan, and J. P. Faurie, Methods for magnetotransport characterization of IR detector materials, *Semicon. Sci. Technol.* **8**, 805 (1993).

[12] S. M. Sze, K. NG. Kong, *Physics of Semiconductor Devices, 3rd Edition,*, John Wiley & Sons, Inc., Hoboken, New Jersey (2007).

Chapter 6

[1] D. T. Britton, E. A. Odo, G. Goro Gonfa, E. O. Jonah and M. Härting, Size distribution and surface characteristics of silicon nanoparticles *J. Appl. Cryst.* **42** (2009).

[2] D.K. Rai, G. Beaucage, E.O. Jonah, D.T. Britton, S. Sukumaran, S. Chopra, G. Goro Gonfa, and M. Härting, Quantitative investigations of aggregate systems, *J. Chem. Phys.*, **137**, 044311 (2012).

[3] E. O. Jonah , D. T. Britton, P. Beaucage, D. K. Rai , G. Beaucage, B. Magunje, J. Ilavsky, M. R. Scriba, M. Harting, Topological investigation of electronic silicon nanoparticulate aggregates using ultra-small-angle X-ray scattering, *J Nanopart Res.* 14:1249 (2012).

[4] D. Stauffer, A. Aharony, *Introduction to percolation theory 2nd edition*, Taylor & Francis, London, UK (1994).

[5] F. Duan, J. Guojun, *Introduction to condensed matter physics Vol 1*, World Scientific Publishing Co. Pte Ltd., London (2005).

[6] R. T. Tung, Electron transport at metal-semiconductor interfaces: General theory, *Phys. Rev. B*, 45, 13509 (1992).

[7] S. M. Sze, K. NG. Kong, *Physics of Semiconductor Devices, 3rd Edition,*, John Wiley & Sons, Inc., Hoboken, New Jersey, 2007.

[8] L.A. Ragnarsson and P. Lundgren, Electrical characterization of P-b centers in (100)Si-SiO2 structures: The influence of surface potential on passivation during post metallization anneal, *J. Appl. Phys.*, **88**, (2), 938-942, 2000.

[9] M.R. Scriba , D.T. Britton , C. Arendse, M.J. van Staden, M. Härting, Composition and Crystallinity of Silicon Nanoparticles Synthesized by Hot Wire Thermal Catalytic Pyrolysis at Different Pressures, *Thin Solid Films* 517, 3484–3487 (2009).

[10] K. F. Brennan, *Introduction to the Physics of semiconductors with applications to optoelectronic devices*, The Press Syndicate of the University of Cambridge, Cambridge, UK (1999).

[11] H. Alloul, *Introduction to the Physics of electrons in solids*, Springer, Berlin (2011).

[12] D. C. Cronemeyer, Hall and drift mobility in high-resistivity single crystal silicon, *Phys. Rev.*, **105**, (2) (1957).